

AD-A130 923

SCANNING LASER DOPPLER ANEMOMETER AND ITS APPLICATION
IN TURBULENT SEPARA... (U) SOUTHERN METHODIST UNIV DALLAS
TX DEPT OF CIVIL AND MECHANICAL 8 CHEHROUDI ET AL.

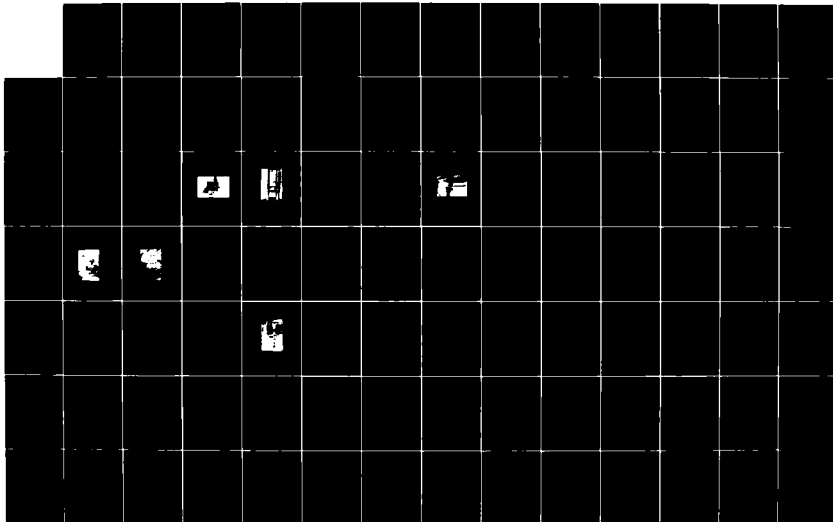
1/2

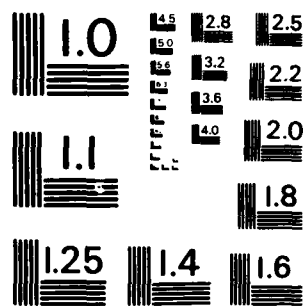
UNCLASSIFIED

JUL 83 SMU-WT-7 N00014-79-C-0277

F/G 14/2

NL





MICROCOPY RESOLUTION TEST CHART
NATIONAL BUREAU OF STANDARDS-1963-A

AD A130923

SCANNING LASER DOPPLER ANEMOMETER AND
ITS APPLICATION IN TURBULENT SEPARATED FLOW

B. Chehroudi and R.L. Simpson

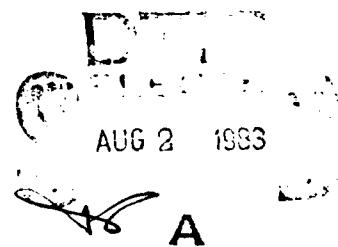
July 1983

Office of Naval Research

Contracts N00014-79-C-0277
and N00014-82-K-0554

Southern Methodist University
Department of Civil and Mechanical Engineering

Report WT-7



Approved for Public Release
Distribution Unlimited

83 07 26 063

DTIC FILE COPY

Unclassified

SECURITY CLASSIFICATION OF THIS PAGE (When Data Entered)

REPORT DOCUMENTATION PAGE		READ INSTRUCTIONS BEFORE COMPLETING FORM
1. REPORT NUMBER SMU-WT-7	2. GOVT ACCESSION NO. AD-A130923	3. RECIPIENT'S CATALOG NUMBER
4. TITLE (and Subtitle) Scanning Laser Doppler Anemometer and its Application in Turbulent Separated Flow		5. TYPE OF REPORT & PERIOD COVERED Technical March 1980 - June 1983
		6. PERFORMING ORG. REPORT NUMBER SMU-WT-7
7. AUTHOR(s) Behrouz Chehroudi Roger L. Simpson		8. CONTRACT OR GRANT NUMBER(s) N00014-79-C-0277 N00014-82-K-0554
9. PERFORMING ORGANIZATION NAME AND ADDRESS Southern Methodist University Dallas, Texas 75275		10. PROGRAM ELEMENT, PROJECT, TASK AREA & WORK UNIT NUMBERS
11. CONTROLLING OFFICE NAME AND ADDRESS Office of Naval Research 800 N. Quincy Street Arlington, VA 22217		12. REPORT DATE July 1983
		13. NUMBER OF PAGES 131
14. MONITORING AGENCY NAME & ADDRESS (if different from Controlling Office)		15. SECURITY CLASS. (of this report) Unclassified
		15a. DECLASSIFICATION/DOWNGRADING SCHEDULE
16. DISTRIBUTION STATEMENT (of this Report) Approved for public release; distribution unlimited.		
17. DISTRIBUTION STATEMENT (of the abstract entered in Block 20, if different from Report)		
18. SUPPLEMENTARY NOTES The view, opinions, and/or findings contained in this report are those of the author(s) and should not be construed as an official Office of Naval Research position, policy, or decision, unless so designated by other documentation.		
19. KEY WORDS (Continue on reverse side if necessary and identify by block number) Separation Scanning Laser Anemometer Turbulence Fluid Dynamics Laser Anemometer		
20. ABSTRACT (Continue on reverse side if necessary and identify by block number) A rapidly scanning directionally-sensitive fringe-type Laser Doppler Anemometer (SLDA) which scans the measurement volume perpen- dicular to the optical axis of the transmitting optics is described. Scan frequencies up to 60 Hz over scan distances of 40 cm. have been used, although scan frequencies up to 150 Hz are possible. The maximum		

Unclassified

SECURITY CLASSIFICATION OF THIS PAGE (When Data Entered)

Unclassified

SECURITY CLASSIFICATION OF THIS PAGE(When Data Entered)

scanning velocity of the measurement volume that can be used is directly proportional to the shift frequency of the Bragg cell since each signal producing particle must cross a minimum number of fringes to produce a valid signal. Signal averaging bias is lower with a scanning LDA than with pointwise measurements. Results obtained for a separating turbulent boundary layer show that very good mean and rms velocity profiles of the fraction of time that the flow moves downstream can be obtained in less than one minute of data acquisition. Space-time correlations show that the degree of coherence between outer region and near wall region increases as flow goes into separated zone.

SECURITY CLASSIFICATION OF THIS PAGE(When Data Entered)

ACKNOWLEDGEMENTS

I would like to express my gratitude to Dr. R. L. Simpson for his encouragement, suggestions, support and constructive criticism throughout the course of this work.

My parents Ali and Monir, have also been very supportive by sending messages of patience and endurance, without which this work could not have been done.

I would like to thank Dr. K. W. Heizer, Dale Drager, and A. Linz for their valuable comments and assistance on electrical aspect of this work.

My thanks also go to Dr. Clara Shiloh for her contributions to this work.

Special thanks are also due to Mr. Francis Isley for providing the laboratory support and to Trellas Gotcher for typing this work.

This work was supported by the U. S. Office of Naval Research.

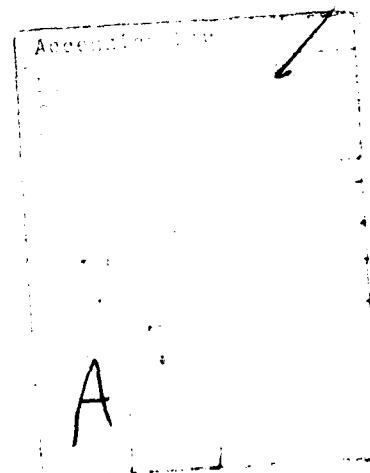


TABLE OF CONTENTS

	Page
ABSTRACT	iv
ACKNOWLEDGEMENT	v
LIST OF FIGURES	ix
LIST OF TABLES	xiv
NOMENCLATURE	xv

Chapter

I. INTRODUCTION	1
1.1 Previous work	1
1.2 Objective of the thesis	4
1.3 Outline of thesis	5
II. EXPERIMENTAL APPARATUS	6
2.1 Basic wind tunnel	6
2.2 Solid particle seeder	9
2.2.1 Seeding techniques examined	10
2.2.2 Details of the seeder design	11
2.3 Conical manifold for particle distribution	13

III. INSTRUMENTATION	19
3.1 Theory of operation	19
3.2 Transmitting optics	22
3.2.1 Lens and mirrors	22
3.2.2 Bragg cell	30
3.2.3 Scanner	35
3.3 Receiving optics	39
3.3.1 Schematic diagram and description .	39
3.3.2 Other alternatives examined for receiving optics	45
3.4 Fringe analysis for scanning system . .	46
3.5 Velocity bias consideration	50
IV. DATA ACQUISITION AND PROCESSING	52
4.1 General description of the problems. . .	52
4.2 Counter type processor	53
4.3 Position calibration of the measurement volume	57
4.4 Data acquisition	60
4.4.1 Pulse marker	60
4.4.2 Data acquisition logic and procedure	64
4.5 Data processing	71
4.6 Static and dynamic check of the entire system.	75
4.7 Position and velocity uncertainty	77

V.	EXPERIMENTAL RESULTS AND DISCUSSION	84
5.1	Mean and RMS values using scanning LDA	84
5.2	Some characteristics of the flow field in this work	95
5.3	Quadrant analysis and space-time correlations	99
5.4	Suggestions for future improvements and extensions	124
5.5	Conclusions	127
	LIST OF REFERENCES	129

LIST OF FIGURES

	Page
2.1 Sideview schematic of the test section . . .	7
2.2 Freestream velocity distribution along the tunnel center line	8
2.3 Schematic of the solid particle seeder . . .	12
2.4 Upper section of the solid particle seeder showing the housing and cylinder	14
2.5 Lower section of the solid particle seeder . .	15
2.6 Qualitative response of the seeder	16
2.7 Conical manifold for introducing seeded air into test section	18

3.1 A simple schematic of a laser anemometer signal generated by a particle passing through a fringe pattern formed in measurement volume	20
3.2 Schematic of the transmitting optics	23
3.3 Photograph of the transmitting optical components	26
3.4 Photograph of the transmitting optics	27
3.5 Alignment of two intersecting beams as observed on a paper target located at the measurement volume position	29
3.6 Optical arrangement for the mirror flatness test	29
3.7 Results from the flatness test on mirrors	31
3.8 Characteristics (flatness) of the mirrors used on the transmitting optics	32
3.9 The Debye-Sears effect	33
3.10 Arrangement for testing the linearity of the scanner	37
3.11 Output of the PM-tube & scanner position output as seen in a dual channel scope	37
3.12 Sampled scanner position voltage versus position of the needle (measurement volume)	38
3.13 Cylindrical lens configuration schematic diagram	40
3.14 Ray paths for the receiving optics	42
3.15 The receiving optics assembly inside of the black box	43
3.16 Number of fringes crossed by a particle as a function of U_f/V_s and U/V_s ; from equ. 3.13.	47

4.1	Characteristics of electrical signal . . .	55
4.2 (a) & (b)	single trace of the band-pass filtered signal on the storage scope with baby powder seeding . . .	56
4.3	Beam position calibration for scanning LDA . .	58
4.4	Effect of the scan range shift . . .	59
4.5	Pulse marker circuit diagram . . .	61
4.6	Timing diagram for the pulse maker . . .	62
4.7	Data acquisition block diagram . . .	66
4.8	Shift of the sawtooth waveform . . .	67
4.9 (a)	Short time representation of the output of the pulse marker in Fig. 4.7 . . .	69
4.9 (b)	Nomenclature used on the sawtooth waveform . . .	69
4.10	Data acquisition, processing logic and signals .	72
4.11	Schematic diagram showing the creation of new record containing the useful data (only valid counter measurements on the upsweep) . . .	73
4.12	Block diagram for static test of the system . .	78
4.13	Static calibration of the entire system . . .	79
4.14	Block diagram for dynamic test of the system . .	80
4.15	Dynamic test of the entire system . . .	81

5.1	Mean velocity vs. position for various frequencies at $x = 436.9$ cm. (170 in) . . .	85
5.2	RMS of the streamwise velocity fluctuations for various frequencies at $x = 436.9$ cm. (170 in) .	86
5.3	Mean streamwise velocity vs. position at four different x-locations	90
5.4	RMS of the velocity fluctuations at four different streamwise locations	91
5.5	Intermittency factor, γ_{pu} , vs. position at four different streamwise locations	92
5.6	(total number of valid measurements) / (total time spent by measurement volume in a bin) versus position	93
5.7	Comparison of the data at $x = 317.5$ cm (125 in) with the Perry and Schofield (1973) mean velocity correlation	97
5.8	Spectra of $\overline{u^2}$ at four streamwise positions . .	98
5.9	Mean velocity vs. position from scanning LDV showing the spatial intervals used for quadrant analysis Figs. 5.10 to 5.16	101
5.10 to 5.16	Quadrant analysis	102

5.17 Terminology used for space-time correlation	
coefficients determined by scanning LDA	109
5.18 Auto-correlation coefficient found using scanning	
set up but for fixed measurement volume at	
$y = 10.2$ cm and $x = 396.2$ cm as compared with	
the scanning results for various number of	
forward cycle delay for an interval centered	
around the same Y-position	111
5.19 Space-time correlation coefficient for zero cycle	
delay vs. position at three different locations	113
5.20 Space-time correlations coefficient between a	
fixed interval near the wall and various inter-	
vals, versus y/δ for three streamwise locations	114
5.21 - 5.23 Space-time correlation coefficient	
vs. y/δ	116
5.24 - 5.28 Instantaneous velocity profiles for four	
consecutive scans starting from lower	
profile	119
5.29 A suggested extension of the existing scanning	
LDA to two-dimensional scanning system	126

LIST OF TABLES

3.1	Characteristic dimensions of the transmitting and receiving optics	24
4.1	Distance travelled by measurement volume during sampling period of T_{ext} (μsec) for various scan frequencies (f_s) with scan range of 30.5 cm. ($=R$)	70
4.2	Maximum sampling pulse period allowable in order to have 3 ($=S$) computer samples in each position bin using 30 ($=N_b$) number of position bins in scan range	76
5.1	Legend for Figs. 5.1 to 5.6	89
5.2	Boundary layer integral parameter for four streamwise positions	96

NOMENCLATURE

d'	Image of the streamwise dimension of the probe volume on the slit
d	Probe volume diameter or streamwise dimension of the probe volume
E	Voltage
$F(n)$	Spectrum function of $\overline{u^2}$
f	frequency
f_m	Bragg cell transducer frequency
f_s	Scan frequency
f_1	focal length of CL1
f_2	focal length of CL2
H	shape factor; δ_1/δ_2
I_f	Image of the scan range (O_1) on the slit (PM-tube)
n	Frequency in spectra measurements
N_b	Number of position bins in scan range
N_s	Number of fringes crossed by a particle crossing the probe volume
n_{max}	Maximum of spectrum function, $F(n)$
O_1	Scan range of the probe volume
R_{uu}	Space-time correlation coefficient defined by equation 5.4
T_R	Retrace time of the sawtooth waveform (Fig. 4.9)

T_s	Period of the sawtooth waveform for the scanner (Fig. 4.9)
T_{tb}	Total time spent by probe volume in each bin for the entire data record
T_{ext}	Sampling period
U	Instantaneous streamwise flow velocity
u	Streamwise velocity fluctuations
u^2	Mean square of u
\bar{U}	Mean streamwise flow velocity
U_∞	Free-stream or external velocity
U_f	Fringe velocity
U_{px}	Streamwise velocity of a particle entering the probe volume
U_r	Velocity of the particle with respect to measurement volume
U_s	Scale velocity for Perry-Schofield model
V_s	Upward scan velocity of the probe volume
x	Horizontal axis measured from the leading edge of the bottom test wall (Fig. 2.1)
x_1	Distance between measurement volume and the first cylindrical lens (CL1)
x_1'	Distance from the first cylindrical lens to the PM-tube
x_2'	Distance from second cylindrical lens (CL2) to the PM-tube
Y	Vertical axis measured from the bottom test wall of the wind tunnel

Greek Symbols

ΔY_R	The distance travelled by the probe volume during sampling period T_{ext}
Δx	Fringe spacing.
$\delta_{.99}$	Boundary layer thickness where $\bar{U}/U_\infty = .99$
δ_1	Displacement thickness $\int_0^\infty (1 - \bar{U}/U_\infty) dy$
δ_2	Momentum thickness $\int_0^\infty (\bar{U}/U_\infty) (1 - \bar{U}/U_\infty) dy$
θ	Angle between two intersecting beams for LDA; angle between relative velocity of a particle entering the probe volume and main flow.
ϕ	Position angle for a particle entering the probe volume
λ	Laser light wavelength

CHAPTER I

INTRODUCTION

The laser Doppler Anemometer (LDA) has become a valuable tool for experimental investigations in fluid mechanics since it can measure the direction and magnitude of the velocity accurately and nonintrusively. Today there are commercial pointwise LDA systems available with specially-designed slow-moving traversing mechanisms to obtain complete flow pattern in large wind tunnels. That means for each spatial location the experiment has to be repeated. Scanning LDA systems are needed for two reasons. First, having almost "instantaneous" velocity profiles, one can investigate the flow structure. Secondly, scanning LDA speeds up the acquisition of velocity information in at least one direction.

This thesis is concerned with the development of the Scanning Laser Doppler Anemometer (SLDA) and demonstration of its usefulness in a turbulent separated flow region.

1.1 Previous Work:

There have been a few scanning LDA systems designed and used in the past. The ones known to the author will be discussed here.

In 1971 a scanning LDA system was described by Bendick (1971) in which he used a translationally oscillating mirror as the heart of his design. This system was used for instantaneous velocity measurements in steady and pulsating water flow in a glass tube of 6mm I. D. with scan

speed of approximately 0.4 m/sec. The proper operation of this design at high scan speeds and large scan ranges is doubtful because of inertial considerations.

In 1973, a two-color dual-beam backscatter scanning LDA system was reported by Grant and Orloff (1973). The scan was accomplished by translating a lens in the direction of the optical axis which caused the measurement volume to move in that same direction. Scan ranges from 60cm to 200cm with variable scan rates from less than 1 cm/sec to maximum of 1.5 m/sec reported to have been achieved. In later reports, this system was employed to investigate periodic flow around a helicopter blade as it passed some fixed azimuthal angle using a mineral oil smoke generator for seeding purposes. Because of low data rates, measurements of instantaneous velocity profiles were not possible, and many scans were needed to represent a plot of mean velocity with a counter type processor. There were no attempts to represent turbulent velocity fluctuations, and fast scan rates were presumably difficult in this translational system. For more information concerning the application of this design, see Orloff and Biggers (1974) and Orloff et al. (1975).

In 1976 a design description of a backscattered scanning system was reported by Rhodes (1976) in which the scan range of 30cm and a scan frequency of 30 Hz were reported. Measurements of flow velocities at 16 discrete positions along the optical axis were made using a large rotating wheel containing 16 ports, 15 of which held glass plates of different thickness. The resident time at each position is 2 msec. This scanning system was used to investigate the flow behind the airfoil using kerosine smoke particles as seeding material with a measurement

volume dimension of 0.2 mm diameter and 1.3 cm length. A counter type processor was used to find the mean velocity for each scan. For more information, see Gartrell and Jordan (1977), and Meyers (1979).

A new optical system was reported in 1978 by Nakatani et al. (1978) which is capable of making true instantaneous velocity profiles. In contrast to all previous designs, there is no moving or scanning device. Spherical lenses are used to increase the beam diameter of the two horizontal incident laser beams. After passing through a converging cylindrical lens, these intersecting beams form a vertical measurement volume along a straight line. The scattered light from this vertical measurement volume is received by a series of optical fibers connected to individual photo-detectors, each collecting data simultaneously from different positions of the measurement volume. Measurements of unsteady flow in a branch tube of rectangular cross-section (2 mm x 10 mm) has been reported in their paper. The results clearly demonstrate the proper operation of this design for small tubes, but instantaneous velocity profiles in a large tunnel, using this design, is expensive and not practical.

Durst et al. (1981) in their scanning system used a rotationally oscillating mirror to scan the measurement volume perpendicular to the optical axis of the transmitting optics. The image of the measurement volume for all the positions fall on one physical point on the photomultiplier (PM-tube). The position transducer as well as PM-tube signals were simultaneously digitized by a two-channel transient recorder, which was triggered only when a Doppler burst was present. The mean and rms velocity profiles via this scanning system were compared with the pointwise measurements and the conclusion was due

to resonance difficulties of the scanner mirror scan frequencies were limited to about 15 Hz. As the system is designed, the measurement volume scans an arc instead of a straight line, and for a given scanner mirror, fringe spacing cannot be varied.

1.2 Objective of the Thesis

Although the scanning laser doppler anemometer has various useful applications, the entire work here was motivated by the fact that in a separated flow region instantaneous velocity gradients are substantially different from the mean velocity gradients. Mixing length and eddy viscosity models fail in this region (Simpson et al., 1981).

Mean velocity and turbulence profiles have already been measured, but no satisfactory model for the backflow has emerged. (Simpson, 1983). If an almost instantaneous velocity profile could be obtained, then more detailed features of the nature of the backflow would be revealed.

With current technology, it is not easy to determine purely instantaneous profiles unless a large number of LDA systems are used simultaneously. Therefore, the objectives of the present work are as follows:

1. Development of a rapid scanning LDA system capable of scanning at least 40 cm or longer at high frequencies.
 2. Demonstration of the proper operation of the above design and its usefulness in the separated flow occurring in the SMU wind tunnel.
-

1.3 Outline of Thesis

Chapter 2 describes the geometry and dimensions of the wind tunnel as well as the details of the solid particle feeder employed for flow seeding in the tunnel. The conical manifold used for uniform flow seeding is also described in this chapter.

Chapter 3 deals with the design of the new scanning LDA. The components of the transmitting and receiving optics are explained in conjunction with a discussion of a non-dimensional parameter representing the number of fringes crossed by a particle in this scanning system. Analysis of the velocity biasing is also mentioned.

Chapter 4 is devoted to the detailed description of the data acquisition and processing procedures and logics. Position and velocity uncertainty analysis as well as the methods used for testing the entire system are also explained here.

Chapter 5 gives the experimental results taken in a separating turbulent boundary layer occurring in the SMU wind tunnel. The first set of results is for demonstrating the proper operation of this new design, and the system is used to map out the flow in the tunnel to further reinforce its capabilities. Later in this chapter, space-time correlation coefficients taken for the first time in a separated flow are shown and discussed with the hope of acquiring some more insight to the flow structure. The suggestions for further improvements and conclusions are mentioned at the last part of this chapter.

CHAPTER II

EXPERIMENTAL APPARATUS

2.1 Basic Wind Tunnel

The mainstream flow of the blown open-circuit wind tunnel is introduced into the test section after first passing through a filter, blower, a fixed-setting damper, a plenum, a section of honeycomb to remove the mean swirl of the flow, seven screens to remove much of the turbulence intensity and finally through a two-dimensional 4:1 contraction ratio nozzle further to reduce the longitudinal turbulence intensity while accelerating the flow to test speed.

The upper wall is adjustable so that the free-stream velocity or pressure gradient can be adjusted. The side walls are made of float glass. The test wall is constructed from 1.9 cm thick fin-form plywood, reinforced every 28 cm with 7.6 x 3.8 x .6 cm cross-section steel channel. Figure 2.1 is a side-view schematic diagram of the 7.62 m long, .91 m wide test section of the wind tunnel.

The active boundary-layer control system, which is described by Simpson, Chew, and Shivaprasad (1980), is used to eliminate preferential separation of the curved-top-wall boundary layer. Highly two-dimensional wall jets of high-velocity air are introduced at the beginning of each of the .20 m long sections. At the latter two streamwise locations the oncoming boundary layer is partially removed by a highly two-dimensional suction system.

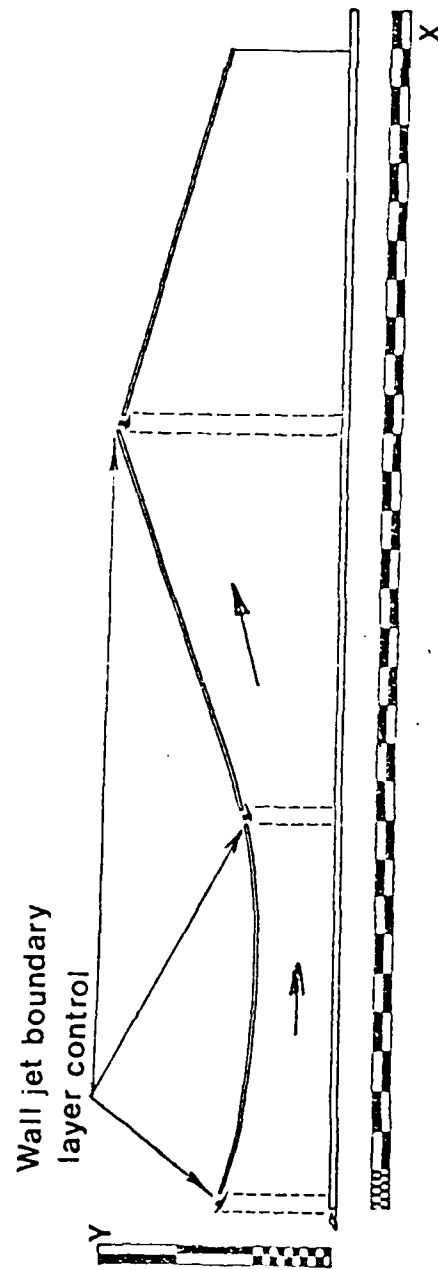


Fig. 2.1 Sideview Schematic of the Test Section.
 Major division on scales: 10 in (25.4 cm).
 Note baffle plate upstream of leading edge on bottom test wall, and side and upper wall jet boundary layer controls. Coordinates (X and Y) are as shown here.

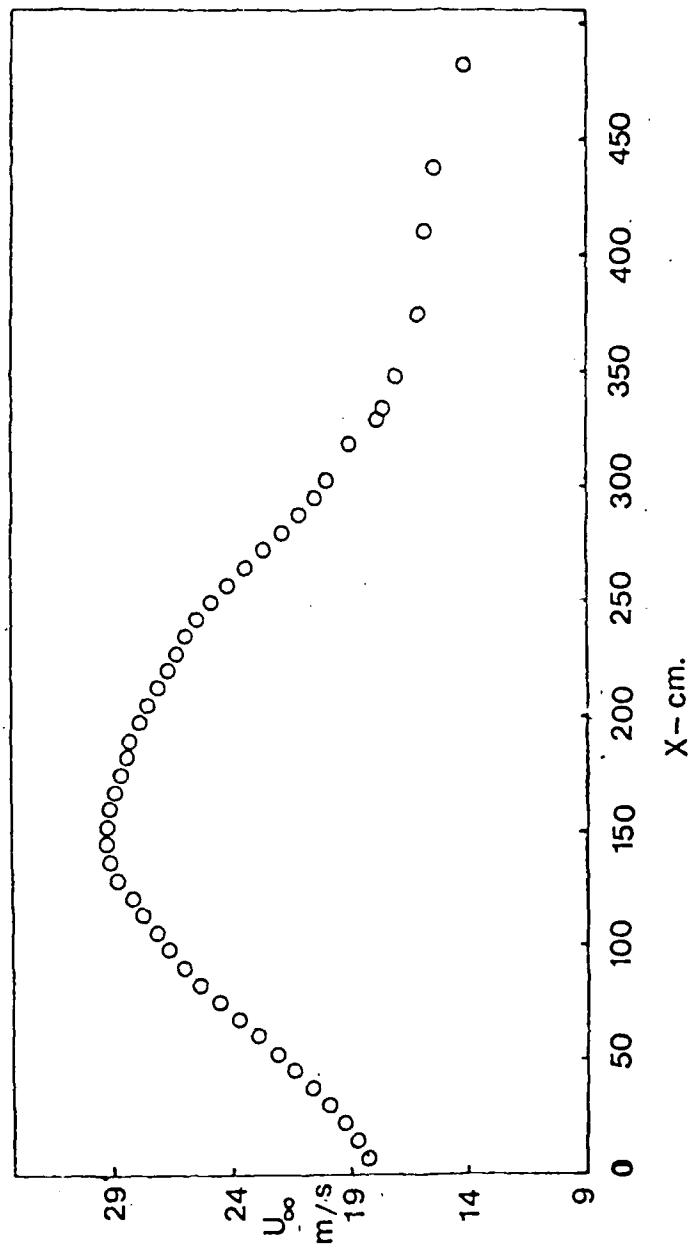


Fig. 2.2 Freestream Velocity Distribution along the Tunnel Centerline.

The inviscid core flow is uniform within 0.05% in the spanwise direction and within 1% in the vertical direction with a turbulence intensity of 0.1% at 20.9 m/sec. Figure 2.2 shows the free-stream velocity distribution obtained along the tunnel center-line using the single-wire probe.

2.2 Solid particle Seeder

The choice of the particle seeder explained in this section is based on a series of exhaustive experiments conducted on the entire system including SMU wind tunnel and counter type processor for data acquisition. (See Chapter IV)

Adrian et al. (1975) showed that a signal with at least 45dB signal-to-noise ratio (SNR) was required for results not prejudiced by the counter processor settings. Since determination of SNR practically, if not impossible, is not easy for all seeding agents, a more realistic approach was used to find the "proper" seeding material in this work. Here, "proper" means that the particles are faithfully following the flow and the 45 dB SNR criterion for counter processor is fulfilled.

To find the appropriate seeding material for this work, the results (mean and RMS of velocity) for the pointwise velocity measurements taken with the scanning set up (explained in Chapter 3), at a given-fixed streamwise position, were compared with the known established results (reference velocity profiles) measured with different arrangement at that same location (Simpson, 1978).

2.2.1 Seeding Techniques Examined

The aerosol generator at SMU was based on the design proposed by Echols and Young (1963) using dioctyl phthalate (DOP) as seeding material. A series of experiments using this aerosol generator with scanning LDA arrangement, operated in pointwise mode, did not give satisfactory results. It was suspected that too many sub-micron DOP particles were present and were producing much signal noise with a fringe spacing of $3.3 \mu\text{m}$.

A series of detailed tests on this DOP aerosol particle generator were performed at the University of Arkansas by the group headed by Professor M. K. Mazumder using the SPART aerosol analyser (Mazumder et al. 1979). These tests confirmed the suspected factor since only 30% of the particles were ever greater than $1 \mu\text{m}$. In a chain of experiments a technique proposed by Seegmiller (1982) which uses Paasche HS #5 air-brush with a mixture of 2 liters of denatured methanol, 100cc of warm water, and 10cc polylatex spheres was examined.

Air brushes were used in various streamwise locations, just upstream of the leading edge of the test wall of the tunnel and upstream of the contraction, and at different injecting angles with respect to the floor of the tunnel. No "satisfactory" results were obtained with the scanning LDA, operated in pointwise mode having $3.3 \mu\text{m}$ fringe spacing, in comparison with the reference velocity profiles.

Various powders were used with the existing particle seeder, explained in the next section; and, finally, it was found that the baby powder produced relatively 'satisfactory' results. The estimated density of the baby powder is about 0.8 g/cm^3 which is almost 650 times

that of air. The particle diameter is also estimated to be in the order of few microns ($<10\text{ }\mu\text{m}$). Hjelmfet and Mockros (1966) showed that, for the case where the ratio of the seed density to fluid is about 1000; particles with $7\text{ }\mu\text{m}$ diameter will give frequency response up to 812 Hz. This limiting frequency increases with decrease in particle diameter and when density ratio approaches one.

2.2.2 Details of the Seeder Design

The solid particle seeder built at SMU is similar in design to the Opto-Elektronische Instrumente (Karlsruhe, Germany) (OEI) Model 101 solid particle seeder which uses baby powder having particles greater than $1\text{ }\mu\text{m}$.

Air passes through a Sears air line filter-regulator Model No. 282-160232, and into the seeder housing. It is important that the air be dried to prevent additional agglomeration of baby powder particles.

The schematic of the seeder is shown in Fig. 2.3. The outlet of the housing is made to contract gradually. The inside corners are filled with sealing foam to streamline the interior surface and thus prevent baby powder from piling up in the housing. One side of the housing is made of plexiglas which enables one to inspect the inside during operation. The inside of the box is accessible via a sealed top lid. The box pressure can be increased up to 1 psig without significant leakage.

A $1/4\text{ HP}$, 1725 RPM, single phase AC motor is used to rotate the shaft inside the housing via a 1 to 1 pulley mechanism. Four 15.2 cm diameter, fine Sears wire wheels (Model No. 9HT64824) are mounted on the shaft inside the box which is being supported by two self aligned

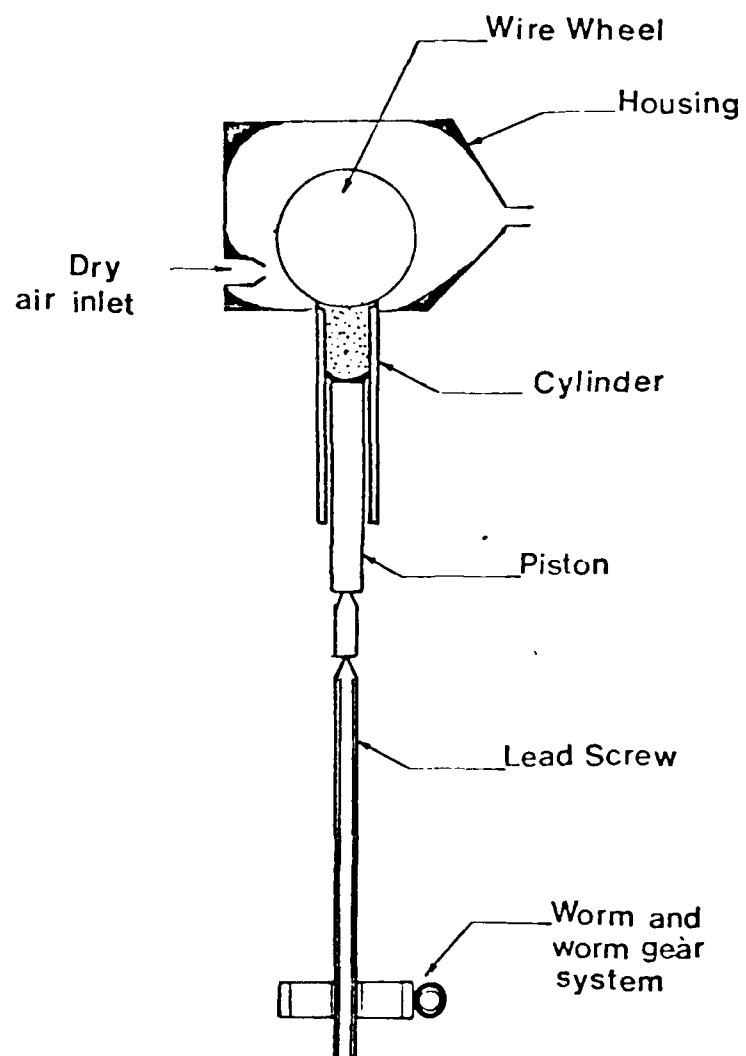


Fig. 2.3 Schematic of the Solid Particle Seeder.

bearings outside the housing and are fixed to the particle seeder frame. The two side holes of the box, from which the shaft passes through, are sealed by two rubber flat plates having a hole size equal to that of the shaft O.D. on each of them and are mounted with two collars on each side to reinforce the sealing due to higher inside pressure of the housing.

The baby powder is pushed up inside the housing by an aluminum piston of 4.78 cm diameter, 30.73 cm length, and is scraped by wire wheels inside. A variable DC motor, to control the seeding rate, with calibrated tachometer and 2 to 1, 90° speed reducer rotates a 10:1 worm gear system which in turn translates a lead screw vertically upward. This lead screw pushes the piston inside the cylinder to feed the housing with the powder (Figs. 2.4 and 2.5).

Air flow rate through particle seeder is measured via a Dwyer Rotometer up to 4 m³/hr and is directed towards the wire wheels. The tip velocity of wire brushes is approximately 4 m/sec, which is much higher than the maximum jet speed of 0.3 m/sec.

The outlet of the housing is directed to the conical manifold which is described in the next section. The qualitative response of the seeder, using counter processor, is shown in Fig. 2.6. The estimated average concentration of the baby powder is 33 mg/m³ and it takes about 10 - 15 minutes to reach its almost steady state condition.

2.3 Conical Manifold for Particle Distribution

It is important to seed the flow in the wind tunnel (for measurement purposes) as uniformly as possible so as to minimize its effects on two-dimensional character of the boundary layer. The powder

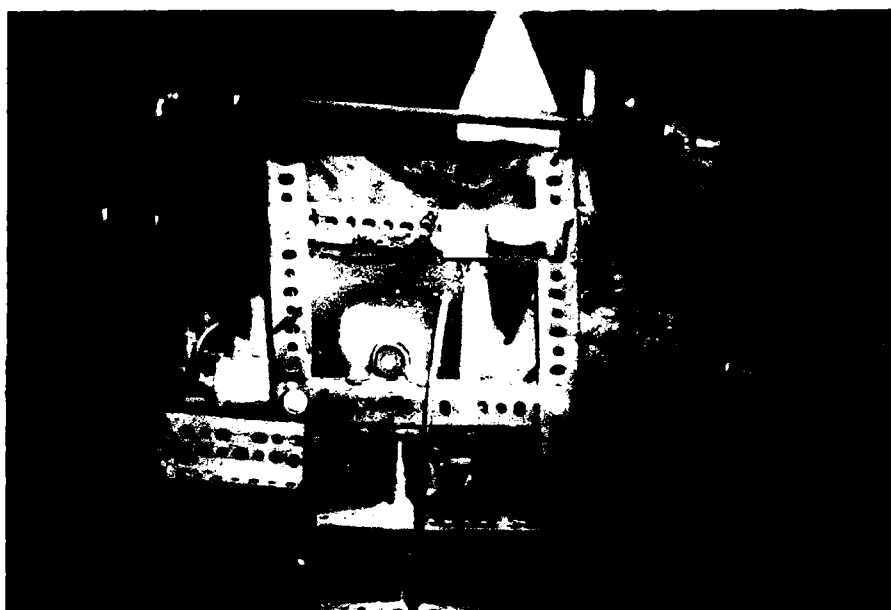


Fig. 2.4 Upper Section of the Solid Particle Seeder.

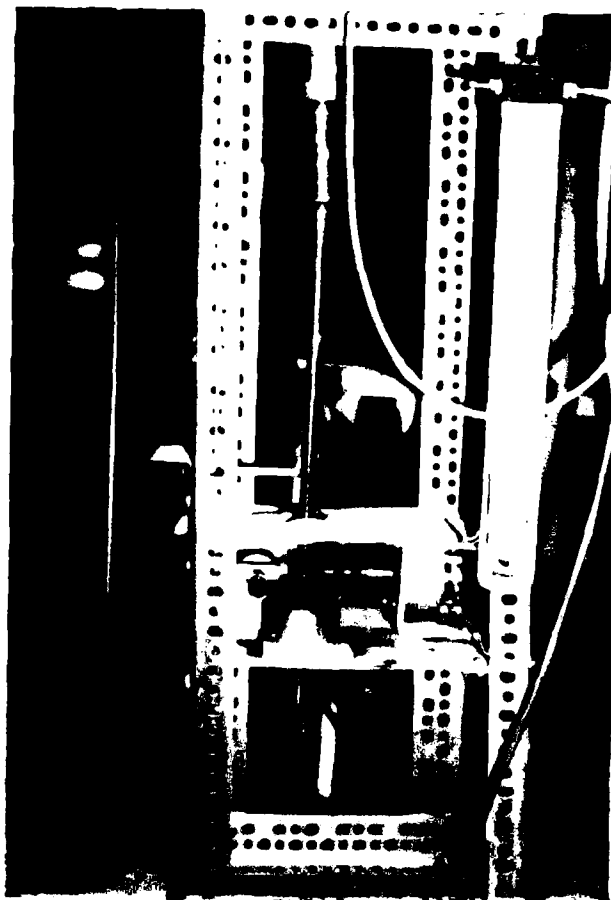


Fig. 2.5 Lower Section of the Solid Particle Seeder.
Worm and worm gear arrangement, lead screw,
and piston are shown.

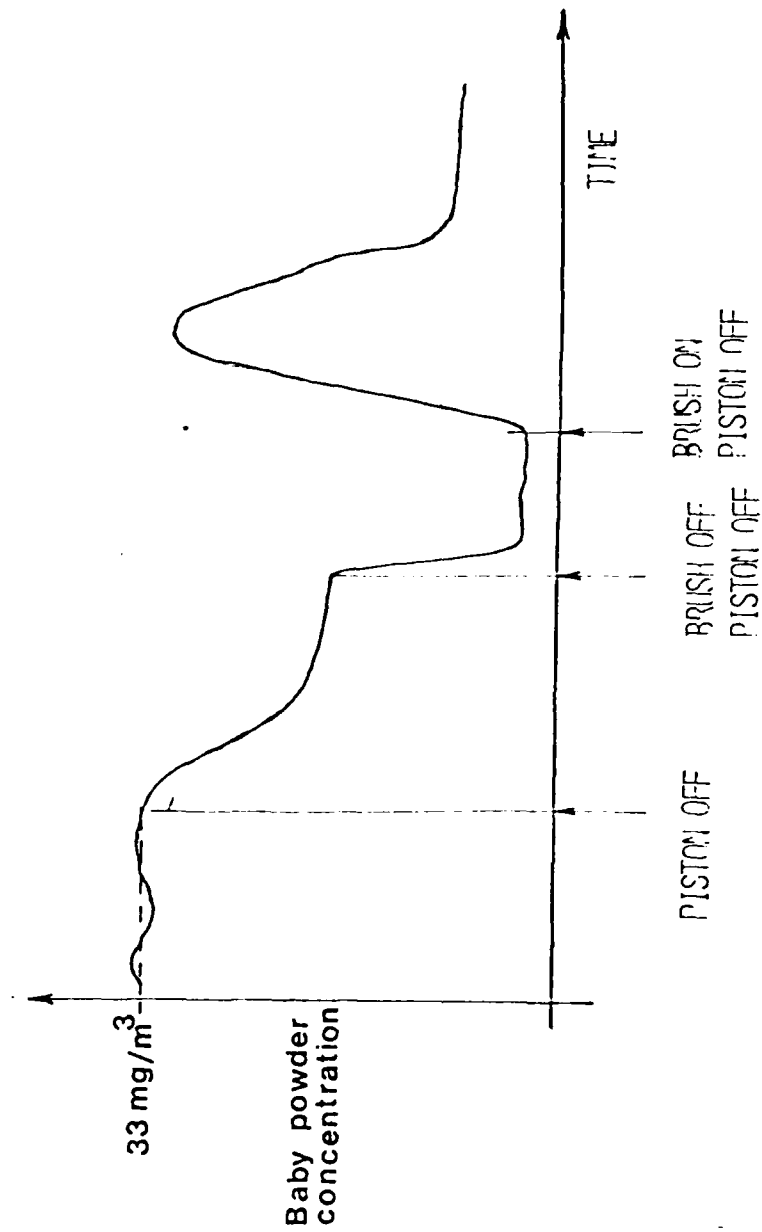


Fig. 2.6 Qualitative Response of the Seeder.

is distributed evenly and injected upward inside the wind tunnel by 32 equally spaced holes of about 4mm in diameter just upstream of the leading edge of the test wall boundary layer. The basic ideas behind the conical manifold are to construct the flow paths for all of the 32 injection holes equal in length, and to eliminate stagnation points. This provides equal tube resistances and consequently equal flow rates through each of the injection parts.

The manifold is conical in shape and consists of thirty-two, 1/4-inch copper tubes inside (Fig. 2.7). The spacings between the tubes are filled with sealing foam to let the powder flow only through the tubes. The end of the copper tubes are connected to the injection ports via plastic tubes.



Fig. 2.7 Conical Manifold (arrow) for Introducing Seeded Air into Test Section.

CHAPTER III

INSTRUMENTATION

3.1 THEORY OF OPERATION:

The basic principle of laser doppler velocimetry is shown in Fig. 3.1. The laser beam is split into the two equal intensity beams that are made to intersect each other at the measurement position. The intersecting beams form "stationary" interference fringes inside an ellipsoidal measurement volume at the focal plane of the lens. To have parallel fringes, the intersection point should occur at the waist of each beam since this is the location where plane wave fronts exit (Durst et al., 1976).

The fringe pattern consists of dark and bright regions of equal spacing. The spacing, Δx , is given by:

$$\Delta x = \frac{\lambda}{2 \sin (\theta/2)} \quad (3.1)$$

Where $\theta/2$ is the half angle between the intersecting beams and λ is the wavelength of the laser light.

If a particle (1 to 4 micron diameter) passes through the measurement volume, as it is shown in Fig. 3.1, it will scatter light which can be detected with a photo detector. The Doppler frequency (Durst et al., 1976) of the scattered light is proportional to the

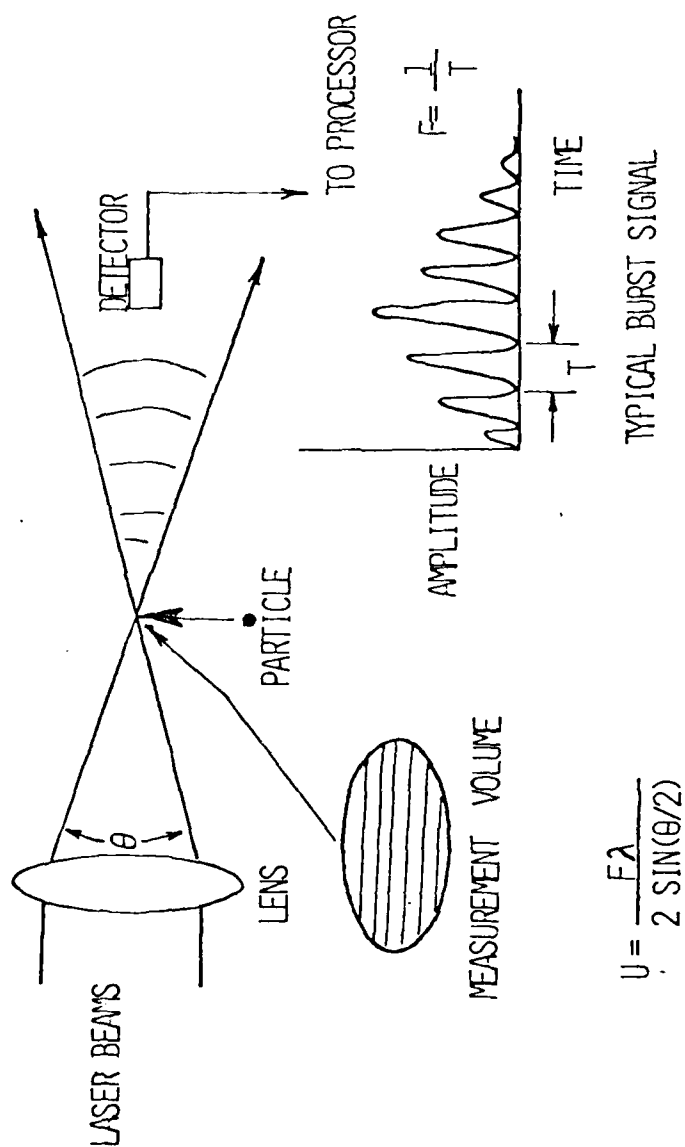


Fig. 3.1 A Simple Schematic of a Laser Anemometer Signals Generated by a Particle Passing through a Fringe Pattern Formed in Measurement Volume.

particle velocity which is given by:

$$f = \frac{2|U|}{\lambda} \sin \theta/2 \quad (3.2)$$

In which $|U|$ is the absolute value of the instantaneous velocity component of the particle in the direction perpendicular to the optical axis (Fig. 3.1).

There are various time and frequency domain instruments used for measurement of Doppler frequency from which the velocity of the suspended particles in one particular direction can be calculated.

Seeding the flow with the so-called "right" material is one of the important factors in laser Doppler anemometry. From a fluid mechanic point of view, one must insure that the particles are faithfully following the flow. This in turn means that the density of the particles should be as close as possible to that of the flowing fluid. The shape, size, and concentration of the particles are also determining factors for their motion.

The system described above is not directionally sensitive; in other words, particles moving perpendicular to the optical axis having the same speed will have the same Doppler frequency. To obtain velocity directionality, an acousto-optic modulator called the Bragg cell, (described in section 3.2.2) is used to modulate the incoming laser beam.

The signal-to-noise (SNR) ratio of the signal output of the photo detector is closely related to the ratio of the particle size to fringe spacing. It is worth mentioning that the particle size normally refers to the mean particle size for a poly-dispersed distribution. The recommended ratio should be chosen in the order of one half. Other factors influencing SNR are: Laser power, relative intensities of the

two light beams, alignment of the transmitting optics, light collecting system, and clean optics.

Another factor worth mentioning is particle concentration. If there is more than one particle at a time inside the measurement volume, constructive or destructive superposition of the scattered lights and consequently of electrical detected signals can occur (Durst et al. 1976).

3.2 Transmitting Optics

Figure 3.2 shows a schematic diagram of the transmitting optics looking from above. An Argon Ion, 5-watt, Spectra Physics, Model 104 Laser with 514.5 nm wavelength is used as a source of the coherent, vertically polarized light for velocity measurements. The Laser beam is passed through the lens combination (L1 and L2) to decrease its beam diameter at the measurement volume, and is split and frequency shifted by a Bragg cell to make the system directionally sensitive. The outgoing beams from the Bragg cell are directed towards a rotationally oscillating scanner mirror (SM) by a small mirror M1. The beams are then reflected to the last-stage mirrors (M5-M7) by a long and fixed mirror M3. Measurement volume moves perpendicular to the plane of Fig. 3.2 as scanner mirror, SM, oscillates.

Requirements for the components in the transmitting optics are discussed below.

3.2.1 Lens and Mirrors

A finer spatial resolution and better fringe visibility are usually achieved by making the measurement volume as small as possible. In this work, there is a minimum limit for the beam diameter at the measurement point. This limit is practically determined by the flatness

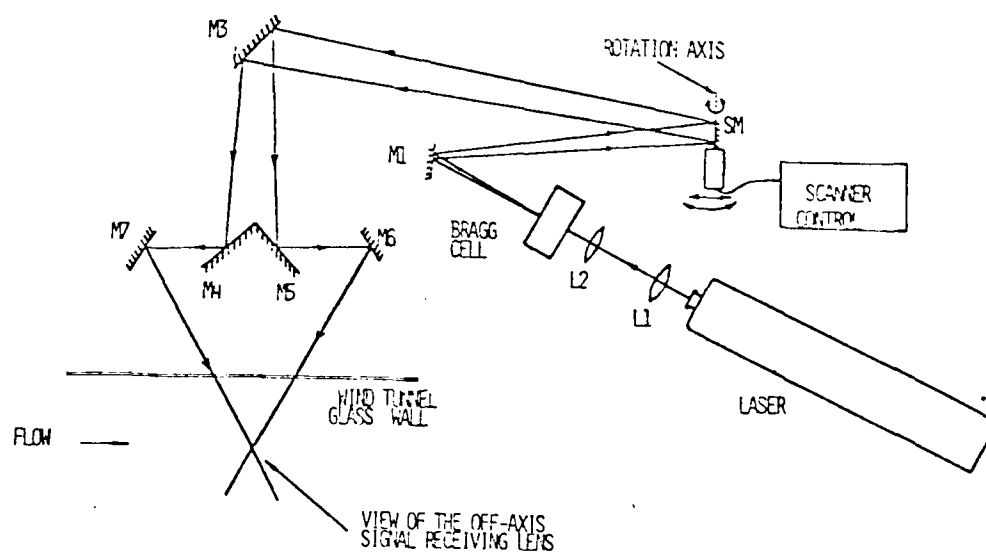


Fig. 3.2 Schematic of Transmitting Optics.
See Table 3.1 for more details.

Table 3.1 Characteristic Dimensions of the
Transmitting and Receiving Optics

Components	Parameter	Value
Mirrors M3-M6	length	254 mm
Lens L1	focal length	55 mm
Lens L2	focal length	100 mm
	distance between L1 and L2	160 mm
Bragg Cell BC	transducer diameter	25 mm
	transducer frequency	15.2 MHz
Scanner Mirror SM	size	26 mm x 39 mm
	vertical dimension of measurement volume	~2 mm
	fringe spacing	*3.1 μ m
	angle between intersecting beams	9.5°
	distance from Laser to the measurement volume	3708 mm
Cylindrical Lens CL1	focal length	300 mm
	size	60 mm x 200 mm
	distance from measurement volume to CL1	663 mm
Cylindrical Lens CL2	focal length	86 mm
	size	57 mm x 60 mm
	distance between C1 & C1	546 mm
	distance between CL2 & PM tube	102 mm
Mirror M8	size	51 mm x 381 mm
Slit	width	1.5 mm
	length	25.4 mm

of the mirrors used.

Two circular positive lenses are used after the laser to decrease the beams' diameters at the measurement position down to 2mm. The estimate of the beam diameter is determined by intercepting the beam with a white paper at the measurement point, and then measuring the diameter of the circular boundary of the bright spot on the paper as observed by a special laser goggle.

The quality of the mirrors is one important factor in this scanning system. For instance, scratches on the mirror could increase the noise level and therefore reduce the SNR. A long and flat front surface mirror, which is aluminized on the surface nearest the object to be viewed, is used so that light reflects from this near surface with no refraction. Mirrors M3 - M7 are also made of this quality (Fig. 3.2) and are mounted on aluminum angles. The process of attaching the mirrors to the angles and the technical difficulties observed will be discussed later in this section.

The last-stage mirrors consist of one mount with two mirrors (named square mirror), M4 and M5, and two independent mirrors, M6 and M7. They are all mounted on a separate optical table which is fixed to the traversing table (Fig. 3.4). For ease of alignment, mirrors M6 and M7 are each mounted on a two-point mirror holder that can rotate the mirror around vertical and horizontal axes. The square mirror has three translational and one rotational degrees of freedom which make the alignment process easy to accomplish.

The purpose of these last-stage mirrors is to enable one to vary the fringe spacing, see equation 2.1, so as to obtain the best SNR for the seeding used here. The mirrors M3 to M7 should be long enough to

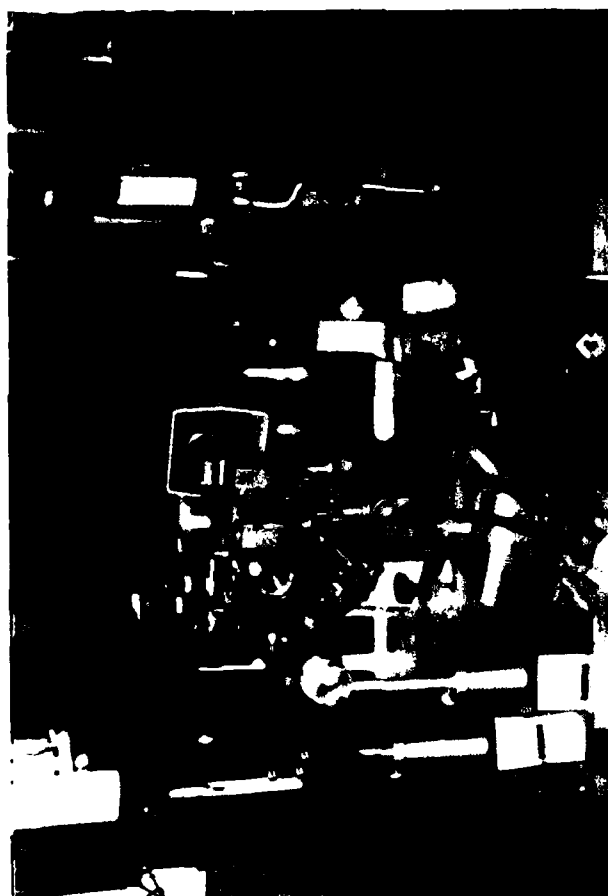


Fig. 3.3 Photograph of the Transmitting Optics Components.



Fig. 3.4 Photograph of the Transmitting Optics.

Laser, lenses, Bragg cell, and scanner are shown.

cover the desired range of movements of the measurement volume.

It is not difficult to see that when the scanning ranges of the two beams are equal in length on the paper target, located exactly at the position of the measurement volume, then the paths travelled by the two beams are equal for any position of scanning (path length equalization for LDA system). In fact, this is one of the advantages of this design since for 90% of the cases the beams can be aligned to scan the same length by only adjusting the mirrors M6 and M7.

The main difficulty with this system was observed when the two beams (reflecting from mirrors M6 and M7) were aligned to cross at the measurement point. One should insure that these two laser beams intersect with each other and are perfectly aligned at any arbitrary position within the scan range (after the path length equalization described above has been accomplished). For a simple alignment check, the system was set on manual scanning mode, and it was observed that the two "spots" on a paper target (located at the measurement point) were not aligned properly as shown in Fig. 3.5(b). This caused significant SNR reduction. In search of the cause of this problem, flatness of the mirrors was suspected. Therefore, some reliable flatness test was needed. For a simple flatness test, a horizontal laser beam was reflected from various points on each mirror to a graph paper target a long distance away as the mirror mount was precisely traversed in a vertical direction and the beam displacement was observed at position (B) as it is shown in Fig. 3.6.

Since silicone glue was originally used to attach the mirrors to the angles, this technique was thought to disturb the beams' alignment. Figure 3.7 shows results of flatness tests conducted on two mirrors before and after gluing. As can be seen, the unit vector normal to the

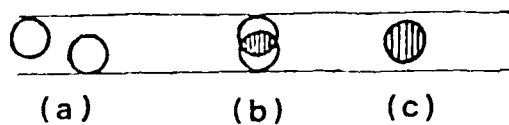


Fig. 3.5 Alignment of two Intersecting Beams as Observed on a Paper Target Located at the Measurement Volume Position.

- (a) Beams are separated.
- (b) Beams overlap.
- (c) Perfect alignment.

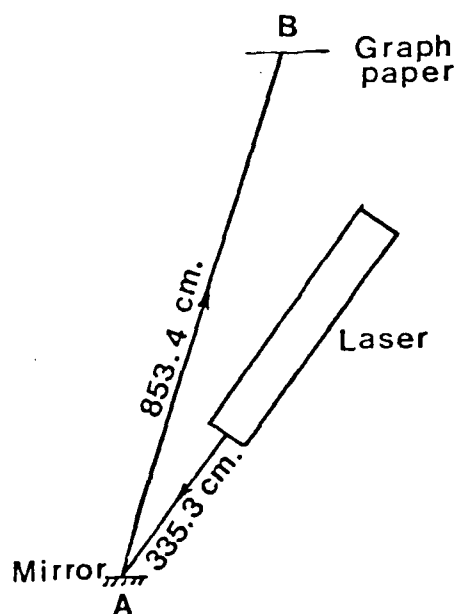


Fig. 3.6 Optical Arrangement for Mirror Flatness (Surface Curvature) Test.

surface of the mirror M6 changes drastically as one scans using this mirror. This important problem was solved by suspending the mirrors from the top to the aluminum angles, using a simple adhesive tape, which also eliminates any changes in flatness due to temperature variation. The results of flatness test conducted on the existing mirrors are shown in Fig. 3.8.

As this system is designed, the measurement volume scans a line rather than a curve; and the variation of the fringe spacing is at most .8% of the fringe spacing measured when the two intersecting beams are in the horizontal plane, which was found to be immaterial for all practical purposes.

3.2.2 Bragg Cell

The Bragg cell works on phenomena known as Debye-Sears effect and Bragg reflection. Basically, if light enters a material with an index of refraction of n , there will be a phase shift occurring on the outcoming light from the material which depends on the propagation constant and the length of material. If this n can be changed sinusoidally with some frequency, f_m , then the outcoming light would be phase modulated at f_m (Debye-Sears effect).

Debye-Sears effect in Bragg cell is observed by using a transducer vibrating at high frequency in a cavity containing distilled water (this creates a variable index of refraction, Fig. 3.9). The incoming laser light is frequently shifted as it leaves the Bragg cell. The power to each of the side band frequencies can be changed by rotating the Bragg cell around the axis normal to the paper in Fig. 3.9 (Bragg reflection).

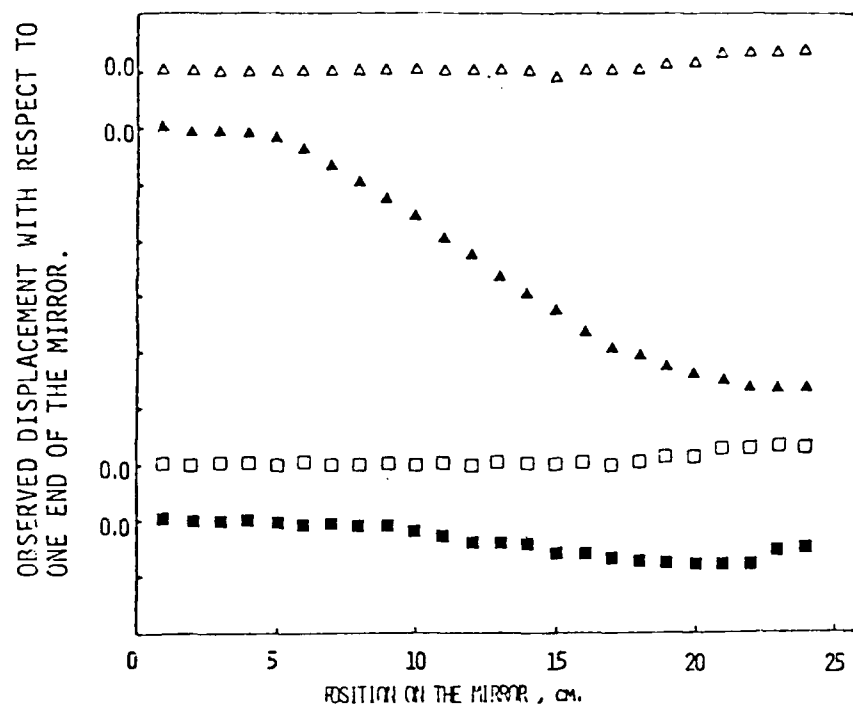


Fig. 3.7 Results from the Flatness Test on Mirrors.
Each division on vertical axis is one centimeter.

Mirror

$\Delta M6$ Before glueing.

▲ M6 After glueing.

☐ M7 Before glueing.

☐ M7 Before glueing.
☒ M7 After glueing.

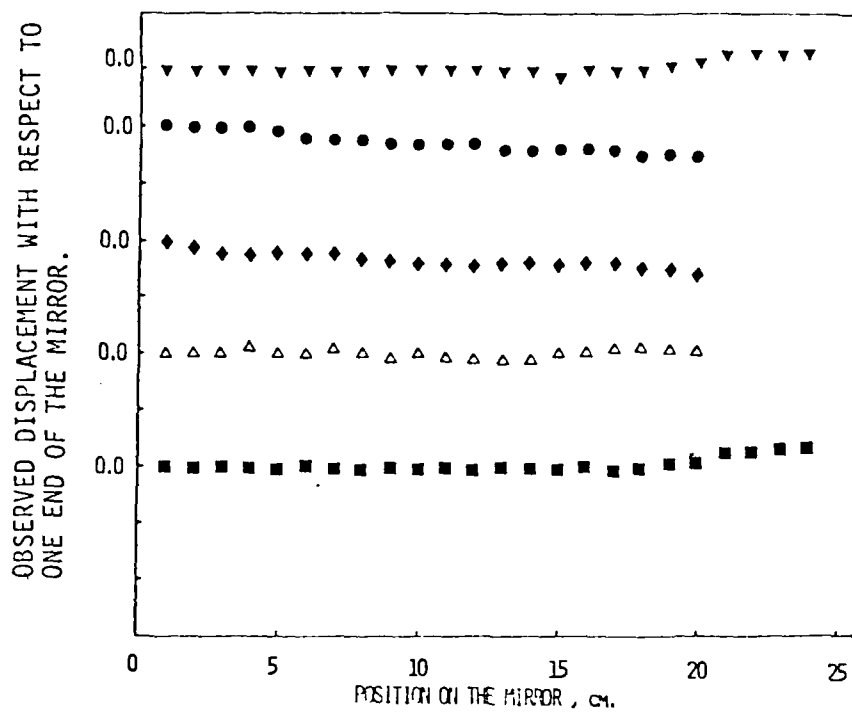


Fig. 3.8 Characteristics of the Mirrors Used on the Transmitting Optics.
Each division on the vertical axis is one centimeter.
▼ M6; ● M4; ◆ M5; △ M3; ■ M7.

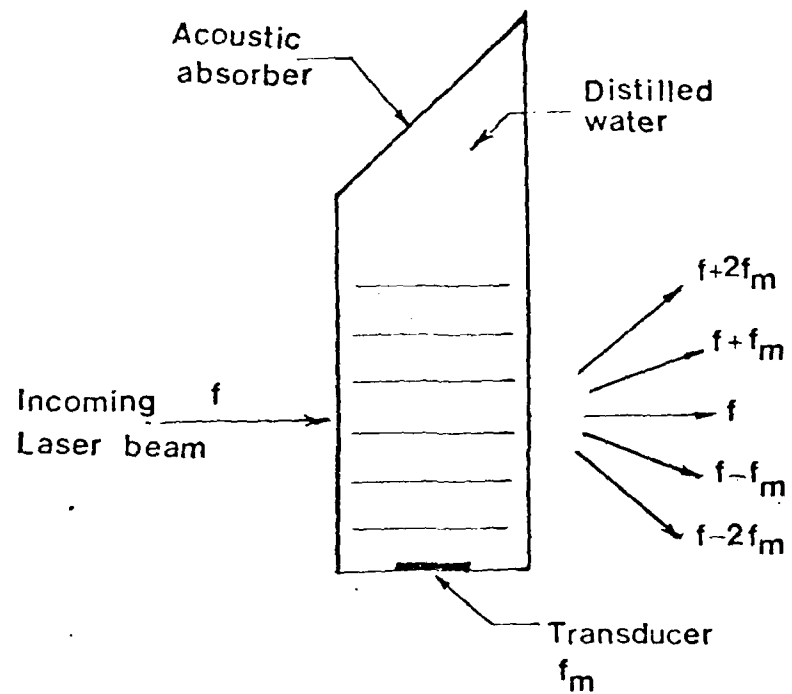


Fig. 3.9 The Debye-Sears Effect.

The Bragg cell transducer used in the present system has a nominal frequency of 5.042 MHz and is polished for the third overtone. It is important to drive it at the natural frequency so that maximum input power can be absorbed and the gold-plated surface of the transducer will not peel off. The natural frequency of the transducer was measured to be 5.067 MHz.

The driver unit of the Bragg cell transducer consists of Heathkit C. B. radio transmitter, Model DX-60, having a crystal oscillator of 7.600 MHz. It amplifies the second harmonic to give 15.200 MHz output. The output of the transmitter was matched to the input impedance of the transducer via an L-C circuit to prevent power reflection back to the transmitter.

Using Bragg cell, one can achieve directional sensitivity for a LDA system. In the present system the first order frequency shifted and unshifted beams are used as intersecting beams. These two beams create a fringe pattern that looks as though it were moving with velocity equal to $\Delta x \cdot f_m$. Here, f_m is the transducer frequency, and Δx is fringe spacing.

In the existing system fringes are moving downstream so that the modified equation for the Doppler frequency is:

$$f = f_m - (2U/\lambda) \sin \theta/2 \quad (3.3)$$

Where f_m is Bragg frequency, U is the instantaneous velocity normal to the optical axis of the system ($U > 0$ for forward flow and $U < 0$ for backflow). The Bragg cell is covered by an aluminum housing to prevent rf - radiation leakage to the signal processing electronics.

3.2.3 Scanner:

The heart of the scanning LDA is a G300PDT scanner from General Scanning Inc. which causes the measurement volume to scan through the boundary layer in the test section. The G300PDT optical scanner is a moving iron galvanometer with a position transducer designed specifically for closed-loop operation. The excursion range is up to 25 degrees of mirror rotation (corresponding to 50 degrees of optical scanning). The position transducer operates by detection of capacitance variation between the rotating armature and a set of stationary electrodes.

Shaft wobble is typically below five arc-seconds. The transducer linearity exceeds $\pm 0.15\%$ of the working excursion; the SNR affords a resolution of one second of arc; and the signal response time is 10 nsec.

The CCX102 controller is a servo control driver amplifiers and includes a stepless DC heater control to regulate the temperature of G300PDT scanner (equipped with a thermister and an adhesive-bonded electrical heater).

Commercial grade scanner mirror, part # M1-3226-39, with thickness of 3.2mm and dimension of 26mm x 39mm, has ALSiO coating (aluminum front surface over coated with silicon monoxide) and is flat to one wavelength per centimeter.

Since the signal processing described in Chapter IV depends on the linearity of the ramp section of the scanner internal sawtooth generator (which drives the scanner mirror), a test is conducted to examine its behavior. The scanner control has an output voltage which

should be linearly proportional to the angular position of its mirror and consequently to measurement volume position. A sewing needle is used to reflect the light when the measurement volume passes the location of this needle, and a photomultiplier with a pinhole detects this light. The output of the PM-tube is a pulse which occurs at the time when the measurement volume crosses the needle. The pulse width depends on the speed of the scanning as well as the needle diameter, Fig. 3.10.

The position-voltage output of the scanner control unit and the output of the PM-tube are fed into a sample-and-hold circuit to sample and hold the position voltage when the measurement volume crosses the needle (see Fig. 3.10). The position of the needle with respect to some reference level is accurately determined by a cathetometer.

Figure 3.12 shows the scanner position voltage output signal versus position of the measurement volume (needle) for two different frequencies. The correlation coefficient for the least square fit was found to be about .999956, which shows the degree of linearity of the waveform. A convenient calibration technique using an HP 9825B computer was used in practice which is described in Chapter IV.

The scanner drift was determined by an experiment to be approximately 0.0002 volts/min, and its effects on the calibration curve are practically negligible.

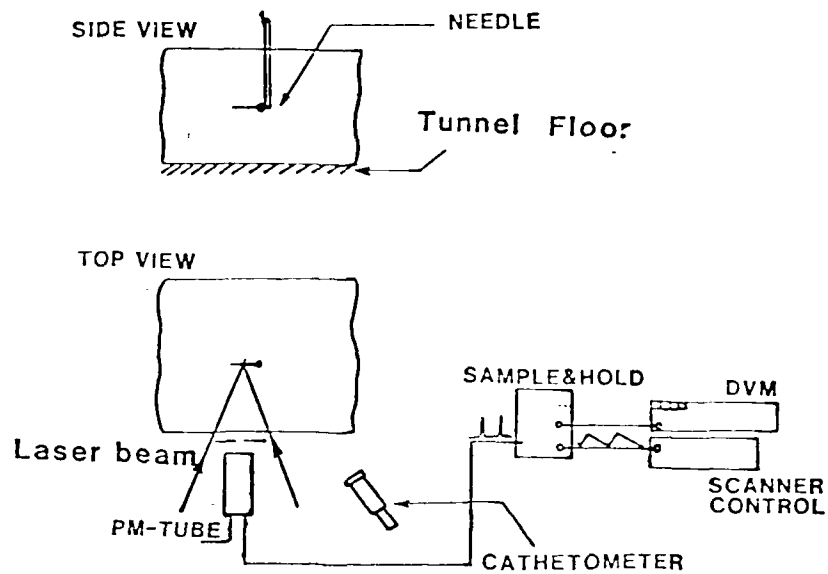


Fig. 3.10 Arrangement for Testing the Linearity of the Scanner.

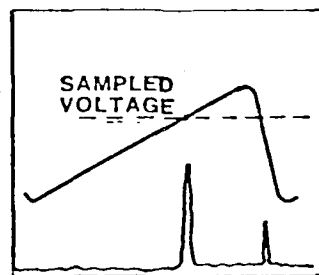


Fig. 3.11 Output of the PM-Tube and Scanner Position Voltage Signal as Observed on a Dual Channel Scope. Note the voltage sampled by Sample&Hold in Fig. 3.10.

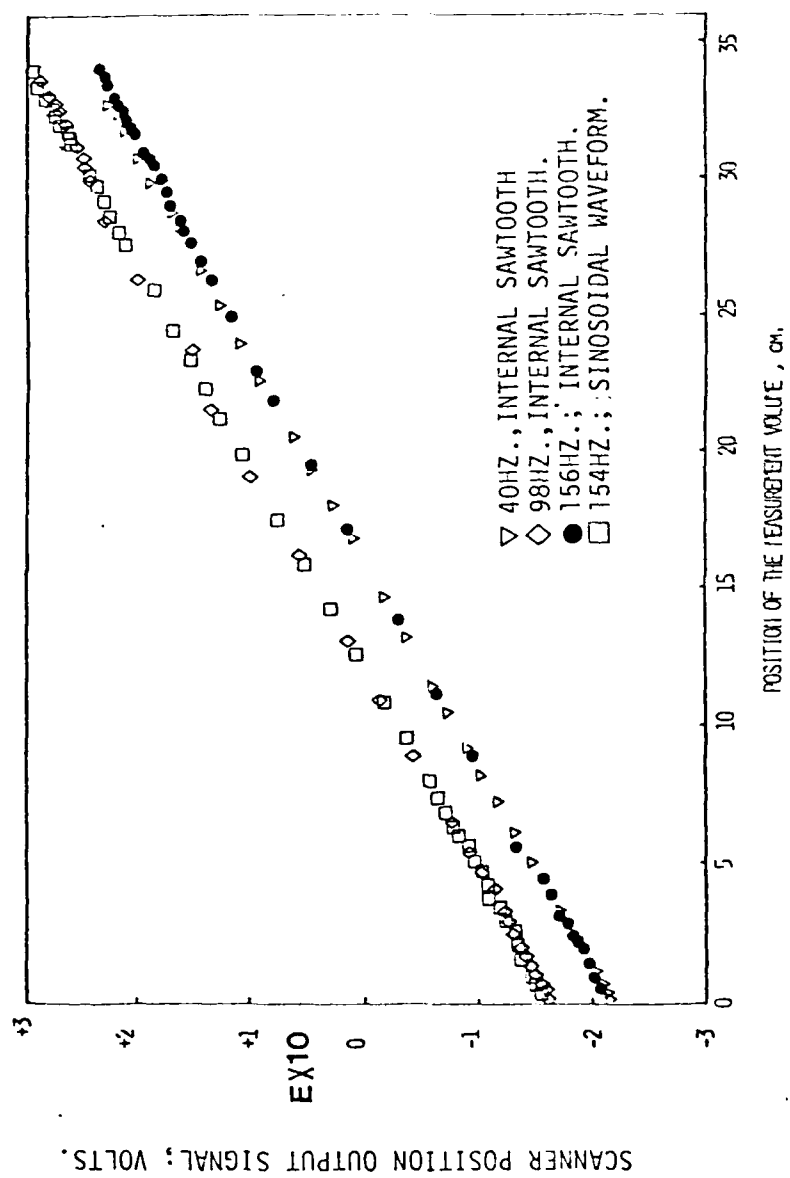


Fig. 3.12 Sampled Scanner Position Voltage vs. Position of the Needle (Measurement Volume).

3.3 Receiving optics

The main idea in the design of the receiving optics is to enable one to detect the scattered signal from the seed particles for any position of the measurement volume throughout the scan range.

Since there is access to a forward-scattering signal on the opposite side of the wind tunnel, and the design is such that no simultaneous movement of incident and receiving optics is required, there is no advantage in working with back scattered signal. Figure 3.13 shows the receiving optics arrangement. The assembly is isolated optically inside a black box having a side door for any adjustment.

3.3.1 Schematic diagram and description

Scattered light enters into the box through four cylindrical lens (CL1), 50 mm x 60 mm, having a focal length of 300 mm. The choice of this focal length was based on the facts that the distance between the center line of the tunnel to the side wall, where the scattered light is gathered, is approximately 457 mm, and the enlargement of the image of the measurement volume in the streamwise direction on the PM-tube was desired.

To make the length of the receiving optics as compact as possible, a long and wide front surface mirror, M8, of the same quality as mentioned for transmitting optics was used to direct the scattered light downward.

The purpose of the second cylindrical lense (CL2), 57 mm x 60 mm and focal length of 86 mm, is to construct the image of the measurement volume on the PM-tube for any positions of scanning. A 5 cm long adjustable slit is made of two pieces of 0.005 inch thick shim stock to gather signal from a portion of the measurement volume.

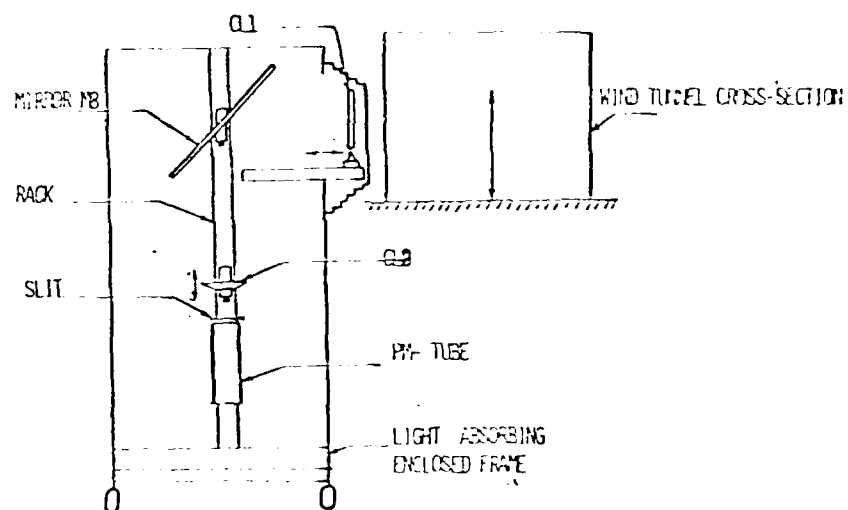


Fig. 3.13 Cylindrical Lens Configuration Schematic Diagram.
See Table 3.1.

Mirror M8, second cylindrical lens (CL2), and PM-tube are all mounted on a rack such that they can be moved in the directions shown in Fig. 3.13. There are two long slots on the rack so that the holders can be fixed at any vertical position desired. To have additional flexibility of alignment, the rack itself can be moved horizontally. The first cylindrical lens, CL1, is mounted on a small channel and its position is also adjustable. The receiving optics arrangement in all of the experiments reported here was off-axis, downstream by approximately 25 degrees.

Figure 3.14 shows the ray tracing for the receiving cylindrical lenses. Since the second cylindrical lens only works in a vertical plane one can use a simple lens equation.

$$\frac{1}{Z+X_1} + \frac{1}{X'_2} = \frac{1}{f_2} \quad (3.4)$$

Where Z is the distance between two cylindrical lenses, X_1 and X'_2 are the distances from the measurement volume to the first cylindrical lens and from second lens to the PM-tube respectively, and f_2 is the focal lens of the second lens (CL2).

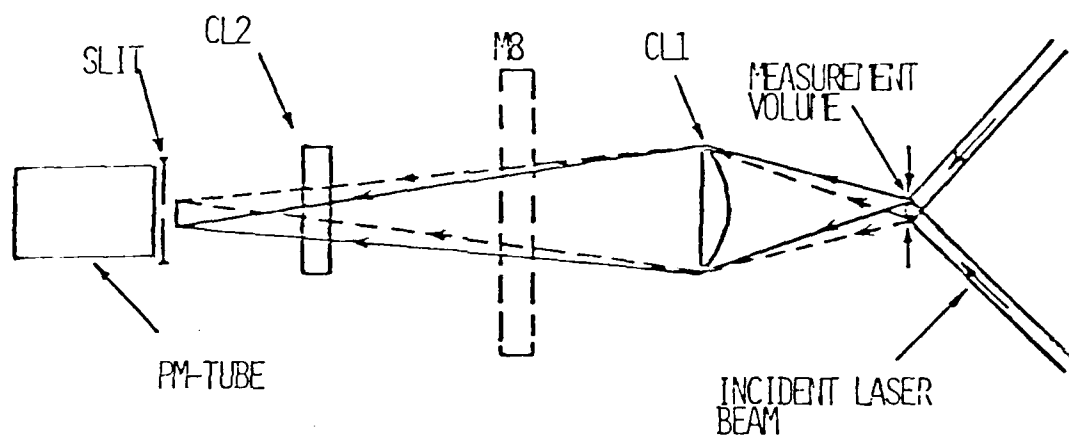
The ratio of the vertical scan range to the image length on the slit is:

$$O_1/I_f = (Z + X_1)/X'_2 \quad (3.5)$$

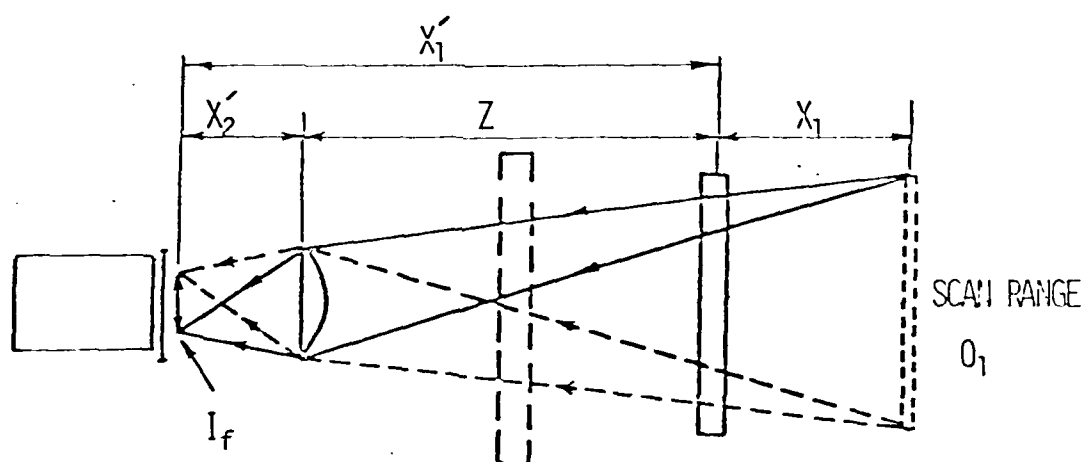
From (3.4) and (3.5), one has:

$$X_1 + Z = 1 + (O_1/I_f)f_2 \quad (3.6)$$

$$X_1 = 1 + (I_f/O_1)f_2 \quad (3.7)$$



(a) TOP VIEW



(b) SIDE VIEW

Fig. 3.14 Ray Paths for the Receiving Optics.

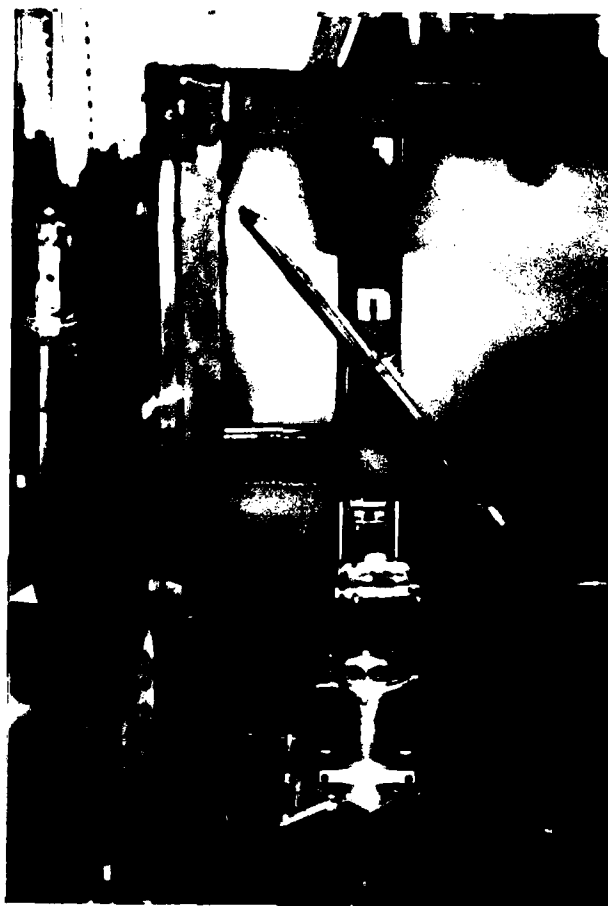


Fig. 3.15 The Receiving Optics Assembly inside of the Black Box.

Using the same lens equation for the first cylindrical lens which works in horizontal plane:

$$\frac{1}{X_1} + \frac{1}{X'_1} = \frac{1}{f_1} \quad (3.8)$$

In which X'_1 is the distance from CL1 to the PM-tube and f_1 is its focal length. From (3.8) finding X'_1 which is equal to $Z + X'_2$:

$$Z + X'_2 = \frac{X_1 \cdot f_1}{X_1 - f_1} \quad (3.9)$$

From (3.6), (3.7) and (3.9) one can easily derive an algebraic equation which determines X_1 for any choices of O_1/I_f ratio and f_2 :

$$f(X_1) = X_1 + (f_1 X_1)/(X_1 - f_1) - [2 + (O_1/I_f + I_f/O_1)] f_2 = 0 \quad (3.10)$$

Using equation 3.10, one can select the lenses considering the following restrictions:

1. Since the photo sensitive front surface of the PM tube is almost 50 mm in diameter and the image of the scan range, I_f , is preferred to fall on the central region of this surface; thus, the image length was decided to be approximately 30 mm.
2. Since the maximum boundary layer thickness in the test section is roughly 330 mm, the maximum scan length, (O_1) , was chosen to be 381 mm.
3. The distance from the measurement volume to the first

cylindrical length, X_1 , should be approximately greater than 457mm and less than 558mm, since the half spanwise width of the tunnel is about 457 mm.

Using the design equation (3.10) with $f_1 = 300$ mm, $O_1 = 381$ mm and $I_f = 30$ mm, one could determine the focal length of the second cylindrical lens of approximately $f_2 = 86$ mm for $X_1 = 485$ mm.

Furthermore, the ratio of the thickness of the image, d' , to the streamwise dimension of the measurement volume would be about 1.62, allowing easy adjustment of the slit width for the best signals. The width of the first cylindrical lens determines the solid angle from which light is collected and should be matched with the width of the second lens.

The second cylindrical lens should be wide enough to gather all the scattered light that is passed throughout the entire length of the first one. The existing width of the second cylindrical lens is 57 mm, which was found to be adequate (see Fig. 3.14).

3.3.2 Other Alternatives examined for Receiving Optics.

The decision on the design explained in section 3.2 was made based on examining other various designs of which two are worth mentioning:

In one design a circular lens was employed to construct the image of the probe volume, for all the positions of scanning, on a long vertical slit behind which the central region of a fresnel lens was used to project the final image on the PM-tube. It was found that this final image was circular in shape for all scan positions. It is worth mentioning that the central strip of the fresnel lens works basically as a very wide cylindrical lens.

The advantage of this design is that it allows one to use a large circular lens to collect more scattered light; disadvantages are the poor quality of the fresnel lens, large bulky set up, and poor signal-to-noise ratio at the ends of scanning.

In another design a circular lens was used to construct the image of the measurement volume, for all the positions of scanning, on a short slit fixed in front of the PM-tube surface. The problem of poor SNR on the scan extremes has been solved by this design, but the image on the PM-tube was very narrow and consequently very sensitive to the slit width. The only advantages of this design are the compactness of the system and the use of a circular lens.

The decision on the final design used in this work was made on the SNR observed by spectrum analyzer (using DOP), and the fact that the counter type processor needs high SNR to give any faithful readings (Adrian et al. 1975).

3.4 Fringe Analysis for Scanning LDA

A simple equation can be derived to represent the number of fringes crossed by a particle as it enters the measurement volume. The analysis is based on the assumption that the probe volume is two-dimensional and circular in shape, and the particle motion is dominated by its streamwise velocity U_{px} . In a directionally sensitive LDA system the fringe pattern is moving with velocity of:

$$U_f = \Delta x \cdot f_m \quad (3.11)$$

In which f_m is the Bragg cell transducer frequency and Δx is fringe spacing. In the system employed for this work, fringes move in the streamwise direction as shown in Fig. 3.16. Here, the relative velocity

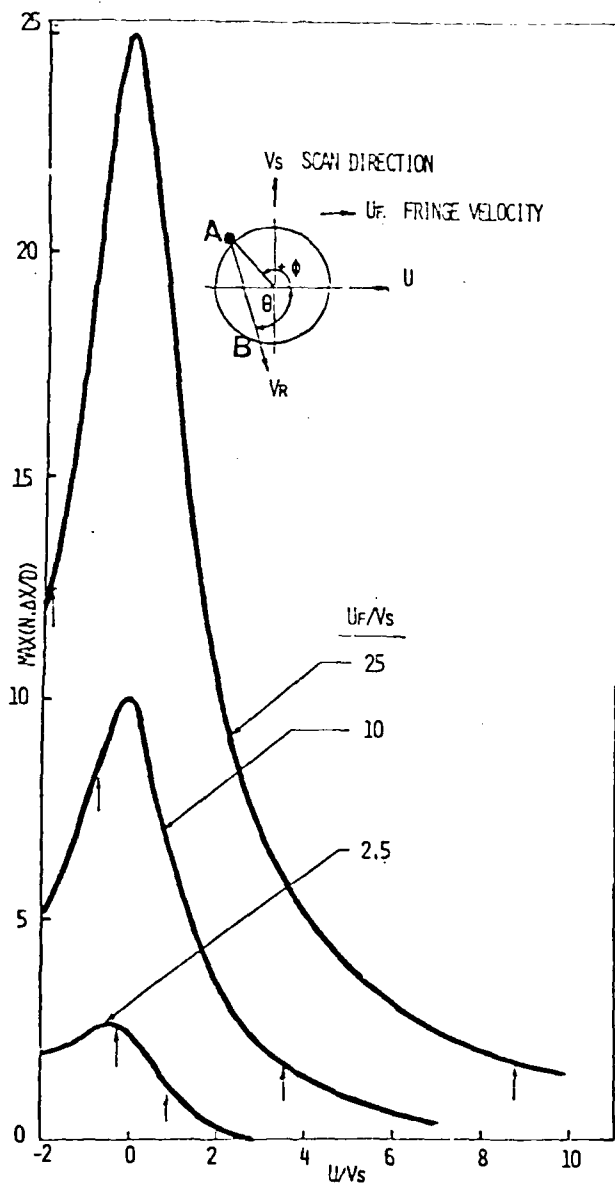


Fig. 3.16 Number of Fringes Crossed by a Particle as a Function of U_f/V_s and U/V_s from Equ. 3.13.

Arrows on each curve show the extremes of the U/V_s ratio at the streamwise location of 436.9 cm.

of a particle with respect to the measurement volume, U_r , is referred to when the probe volume scans away from the bottom wall of the wind tunnel only. Hence, the time needed for a particle to travel one fringe spacing entering from the position angle of ϕ with the streamwise velocity of U_{px} is:

$$t = \frac{\Delta X}{|U_{px} - U_f|} \quad (3.12)$$

In which the negative value for U_{px} represents the backflow situation. The resident time for the particle in the probe volume is (Fig. 3.16):

$$T_r = \frac{\overline{AB}}{U_r} = \frac{d \cos(\theta + \phi - \pi)}{(U_{px}^2 + V_s^2)^{\frac{1}{2}}} \quad (3.13)$$

Where V_s is the upward scan velocity and θ is the angle between the positive direction of U and that of U_r vector (Fig. 3.16). Therefore, the number of fringes crossed by a particle is

$$N_s = \frac{T_r}{t} = \frac{|U_{px} - U_f|}{(U_{px}^2 + V_s^2)^{\frac{1}{2}}} (d/\Delta x) \cos(\theta + \phi - \pi) \quad (3.14)$$

which can be represented in non-dimensional form as:

$$\frac{N_s \Delta X}{d} = - \frac{|1 - (U_f/V_s)(V_s/U_{px})|}{[1 + (V_s/U_{px})^2]^{\frac{1}{2}}} \cos(\theta + \phi) \quad (3.15)$$

For each fixed upswing scan velocity, the ratio U_f/V_s is a constant number and the right hand side of the previous equation is function of V_s/U_{px} and ϕ . Note that the Eq. 3.13 reduces in the limit to the stationary measurement volume as V_s/U_{px} goes to zero.

From a practical point of view, the maximum number of fringes crossed by a particle is of interest and can be derived by setting the cosine term in Eq. 3.15 equal to -1, which physically means that the particle passes through the center of the measurement volume. Figure 3.16 shows the maximum value of $N_s \Delta X/d$ versus U_{px}/V_s for three values of U_f/V_s ratio. The arrows on each curve show the extremes of the U_{px}/V_s parameter at the streamwise location of 436.9 cm in the wind tunnel. The maximum number of fringes crossed by a particle decreases as the scan speed is increased (low values of U_f/V_s).

The maximum number of cycles per signal burst used by the counter type processor in this work is 32. This simplified model was used to insure that there was a sufficient number of fringes crossed by a particle for various scan speeds and flow velocities in the boundary layer. For example, with a maximum streamwise velocity of 17 m/sec, a fringe spacing of 3.1 μm , a fringe velocity of 47 m/sec, and a small effective streamwise measurement volume dimension of 3/4 mm viewed by the slit; a particle will cross no more than 32 fringes with an upper limit scan speed of approximately 200 m/sec, which is much greater than used here. To use a higher scan velocity and still obtain a sufficient number of fringe crossings, a higher Bragg cell frequency could be used.

3.5 Velocity Bias Consideration

According to velocity biasing analysis of McLaughlin and Tiederman (1973), the data rate in a "pointwise" LDA system is proportional to the magnitude of the instantaneous velocity vector U . Therefore, the velocity amplitude probability distribution is biased towards higher velocities. Likewise, the data rate in "scanning" LDA system, in which measurement volume itself moves, is proportional to the magnitude of the instantaneous "relative" velocity of the fluid with respect to the measurement volume U_r .

Based on the refined biasing analysis of Buchhave et al. (1979), the percentage biasing error decreases as the parameter Q and/or σ/\bar{U} decreases. The Q parameter is the ratio of the minimum number of zero crossings required for a valid measurement to the maximum number of fringe crossings available, and σ/\bar{U} is the ratio of the RMS of the velocity fluctuations to the mean value.

One can use the results of the percentage biasing error mentioned in Buchhave et al. (1979) to have an estimate of the biasing error in the present scanning system, but one should note that the mean "relative" velocity of the fluid with respect to the measurement volume, U_r , should be used instead of the mean flow velocity, \bar{U} , in the σ/\bar{U} parameter. For a given σ , using Fig. 3-5 of Buchhave et al. (1979), one can see that the biasing error decreases using scanning LDA, in comparison with the pointwise LDA, considering the fact that the mean relative velocity of the fluid with respect to measurement volume (scanning) is always greater than the mean velocity of the fluid (pointwise), \bar{U} . It is interesting to note that the biasing error decreases as the scan velocity is increased.

Finally, since the required number of zero crossings for a frequency measurement is 32, and the effective total number of fringes available is about 300, the Q factor mentioned above is almost 0.1, and, therefore, the directional dependence is very weak in this work.

CHAPTER IV

DATA ACQUISITION AND PROCESSING

Ideally, in a scanning laser anemometer system one needs to know the exact position of the measurement volume at the time when a "validated" velocity measurement is detected. The data acquisition and processing described in this chapter was a choice based on available facilities in SMU. It might not be the best approach for a scanning LDV system, but it was found to be quite adequate (Durst et al. 1981).

4.1 General description

As mentioned, the "ideal" technique is to sample both position voltage output of the scanner driver (a sawtooth waveform) and the valid frequency (or velocity, see Eq. 3.3) measurements from the analog output of the counter processor simultaneously. The whole process could be triggered via "data ready" output of the counter which sends a pulse every time a new measurement has been validated.

Since the HP-9825B computer used in this work cannot be programmed in assembly language and HPL language is not fast enough to switch and sample position as well as counter output from two A/D convertors, a different technique for data acquisition than the "ideal" one was used.

It is worth mentioning that the switching process from one A/D converter to the other using a HPL command takes on the order of 5 msec. With 15 Hz scanning, using scanner internal sawtooth generator, the scan velocity for the ramp part of the signal is about 5 m/sec. Hence,

during this switching time the measurement volume will translate by about 25 mm. This causes two problems: firstly, it practically eliminates the validated signals during the switching time; secondly, position ambiguity occurs.

The retrace part of the sawtooth position waveform was not used for processing due to its poor linearity. The symmetrical waveform is probably preferred for the external control of the scanner driver, since one can acquire validated signals from the counter processor, both when measurement volume scans upward and downward.

Considering the aforementioned problems, the counter processor analog output has been added to a "marker" signal (stretched SYNC pulse in Figs. 4.7 and 4.10), which marks the end of each upswing scan and was fed into a fast analog-to-digital (A/D) converter. The computer can acquire this signal (output of A/D) as fast as 10,000 samples a second.

It should be emphasized that the computer does not sample each time a validated counter measurement is available, and for this reason, some memory locations will be wasted. Data processing relies heavily on the linearity and repeatability of the upsweep section of the internal sawtooth generator used by the scanner drive control unit (Brosens, 1976). This will be discussed in more detail later in this chapter.

4.2 Counter Type Processor

As mentioned in section 3.1, the scattered light from particles passing through the measurement volume is detected by a photomultiplier which will look like Fig. 4.1. The low frequency variation corresponds to the passage of each particle through one or other or both intersecting beams, and the high frequency represents the passage of a particle through the fringes.

The TSI Inc. Counter, Model No. 1980, is used for finding the high frequency component of the signal (Doppler frequency) which is proportional to the velocity of the particle (Eq. 3.1). The signal conditioning section of the TSI counter consists of a signal amplitude limit control which eliminates the large amplitude signals generated by large particles which are not following the flow, low and high pass filter to remove the low frequency variation and noise respectively, Fig. 4.1, and finally an amplifier with adjustable gain.

Zero crossing technique is the basic principle of operation used for finding the Doppler frequency. The zero cross voltage level is fixed to +50 mv and the signal amplitude can be varied by the gain control of the amplifier. The analog output of the counter is a voltage proportional to the Doppler frequency which in turn is related to flow velocity through Eq. 3.3. This analog output is used for all data acquisitions in this work. The counter holds the output voltage of the validated measurement until the next one occurs, and it measures the time for N cycles and compares them with that of N/2 cycles. A division is actually performed so that it is a true percentage comparison which can be set via a dial on the counter.

Figures 4.2 (a) and 4.2 (b) represent the typical signals observed on the oscilloscope using baby powder as seeding agent while scanning.

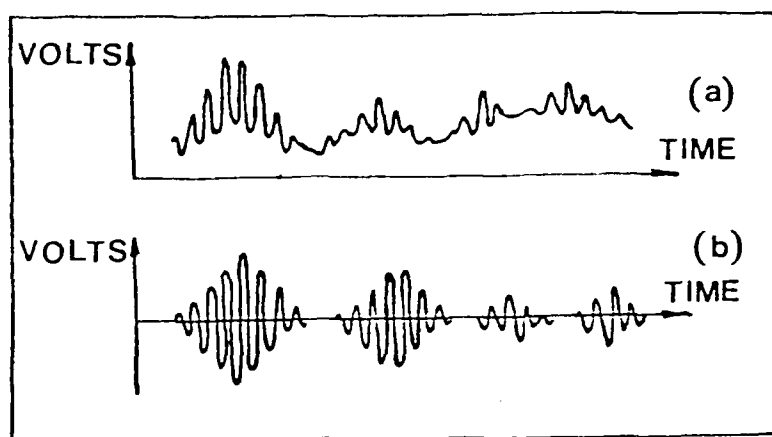
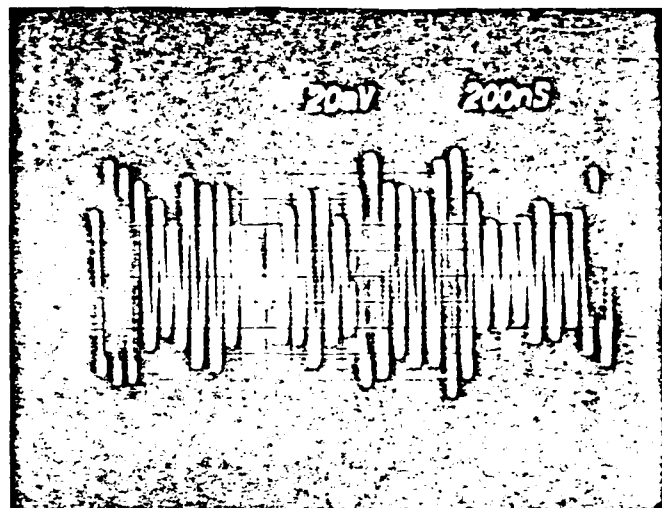
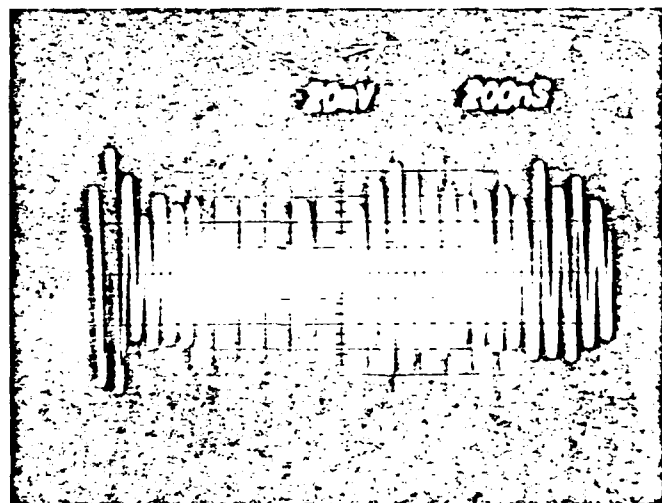


Fig. 4.1 Characteristics of Electrical Signal.
(a) Signal from photomultiplier tube.
(b) After high-pass filtering to eliminate dc pedestal.



(a)



(b)

Fig. 4.2 (a) and (b) Single Trace of the Band-Pass Filtered Signal on a Storage Scope with Baby Powder Seeding.

4.3 Position Calibration of the Measurement Volume

One needs to know the position at which a validated measurement occurs. For this purpose, the scanner driver has a position voltage output (sawtooth) which is proportional to the position of the measurement volume and can be used for calibration.

A special black paper target having 15 holes of 1mm diameter and 25.4 mm apart vertically is attached to a stable frame such that the first hole is 25.4 mm from the tunnel floor. A white piece of paper is attached behind each of the holes to scatter light as laser beams pass over.

The calibration procedure starts by locating the paper target in the position where the velocity profile is needed such that the measurement volume scans through the holes on the target. The same receiving optic arrangement is used for calibration, and as the measurement volume passes over each of the holes a pulse is generated by the PM-tube. Since the pulses on the retrace are not desirable, a low pass filter is used to attenuate and finally eliminate them via a comparator (Fig. 4.3). Hence, only pulses corresponding to the ramp section of the position voltage output of the scanner remain after the comparator. The combination of an inverter, a comparator, and one-shot, (see section 4.4.1) make the pulses look like Fig. 4.3 (G). This signal is used to trigger an A/D converter externally in order to sample the position voltage of the scanner. The HP 9825 computer acquires the sampled position voltages.

The software written for the calibration acquires 50 cycles of consecutive scans of the measurement volume and computes the linear

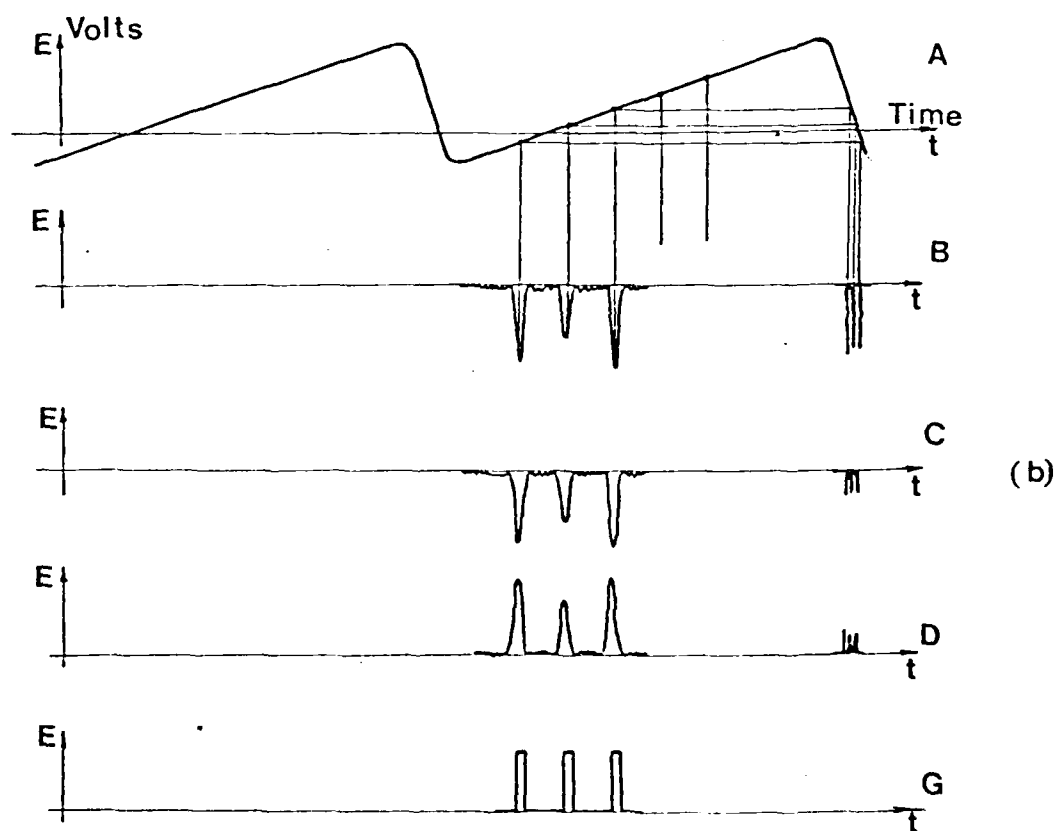
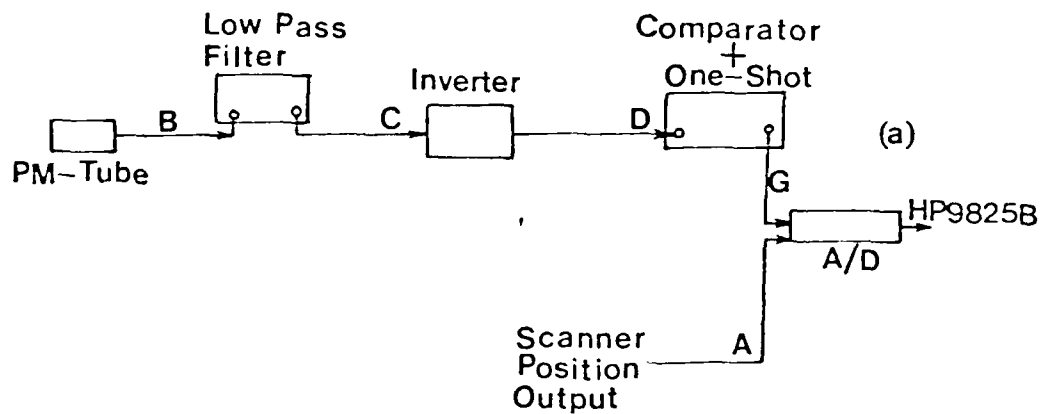


Fig. 4.3 Beam Position Calibration for Scanning LDA.
 (a) Electronic equipment arrangement.
 (b) Typical signals. Labels correspond to points on (a).

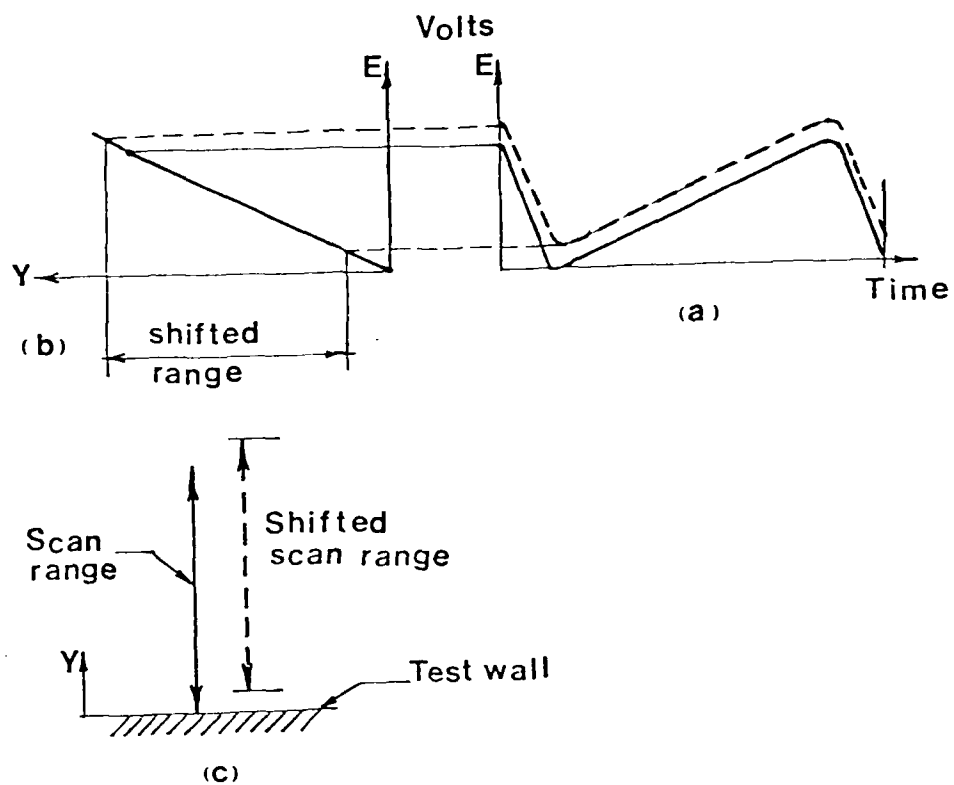


Fig. 4.4 Effect of the Scan Range Shift(c) on the Waveform(a) and on the Calibration Line(b).

least square fit through the sampled position voltages. Therefore, one has a linear relation between the position voltage output of the scanner and the position of the measurement volume.

It was found that the scan range, once set by the scanner driver, remained constant; but the whole scan range shifted either up or down, Fig. 4.4 (c). As far as calibration is concerned, this scanner "shift" does not have significant effects either on slope or on intercept of the calibration line and has been confirmed experimentally. It will, however, cause problems in determining the position corresponding to each computer-sampled point which is discussed in section 4.4.2.

4.4 Data Acquisition

This section is divided into two parts. The first part is devoted to the description of the special circuitry made for the acquisition, called "pulse marker", and the second part deals with the data acquisition logic and procedure.

For more clarity in the logic and procedure of the acquisition and processing, the reader is encouraged to refer to the key Figs. 4.7 and 4.10 frequently.

4.4.1 Pulse Marker

The circuit diagram of the pulse marker is shown in Fig. 4.5. A dual amplifier is used as voltage follower to have high input impedance and to prevent loading of the equipment from which signals are taken.

As can be seen, the diagram has basically two branches which are

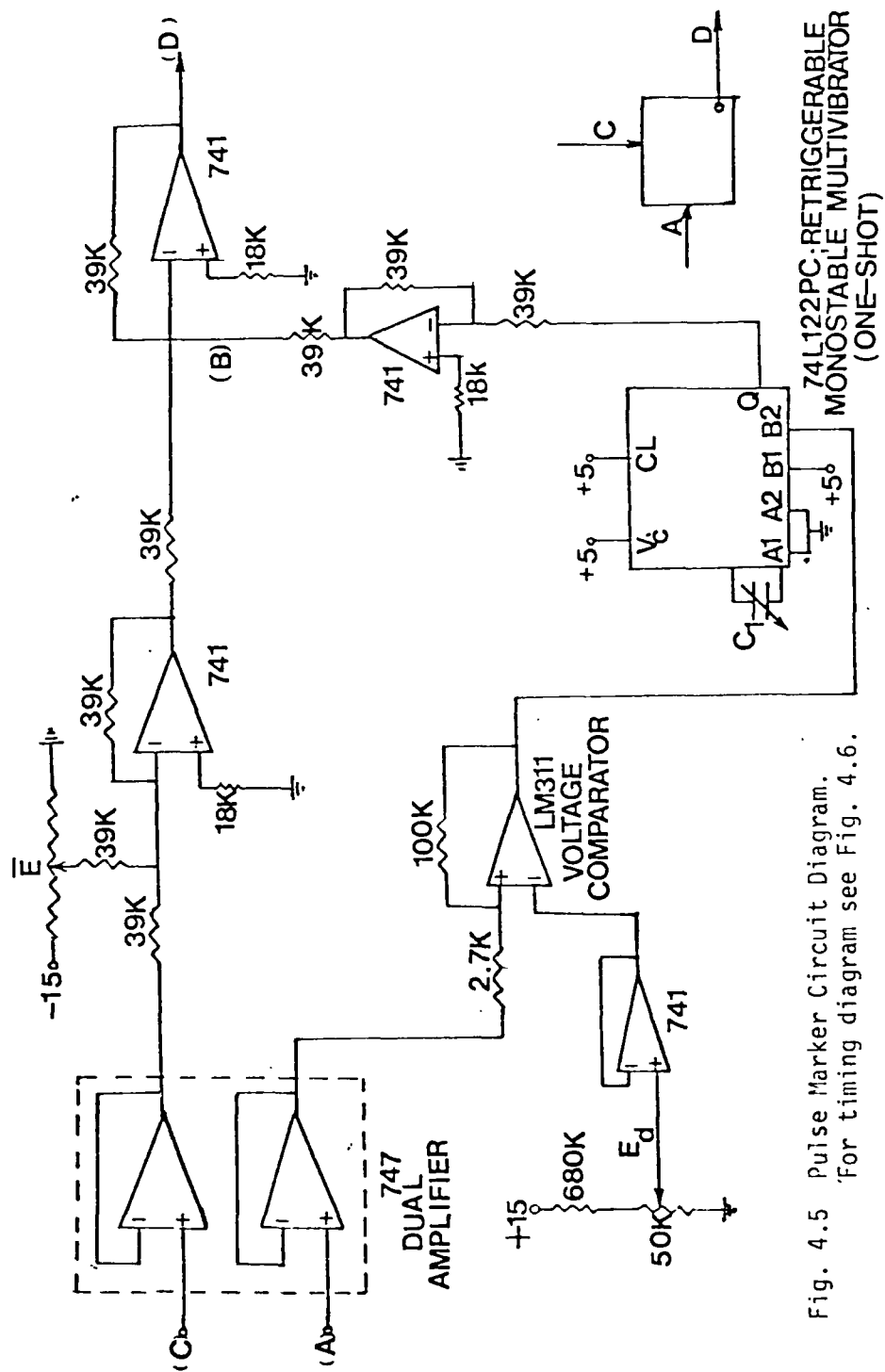


Fig. 4.5 Pulse Marker Circuit Diagram.
For timing diagram see Fig. 4.6.

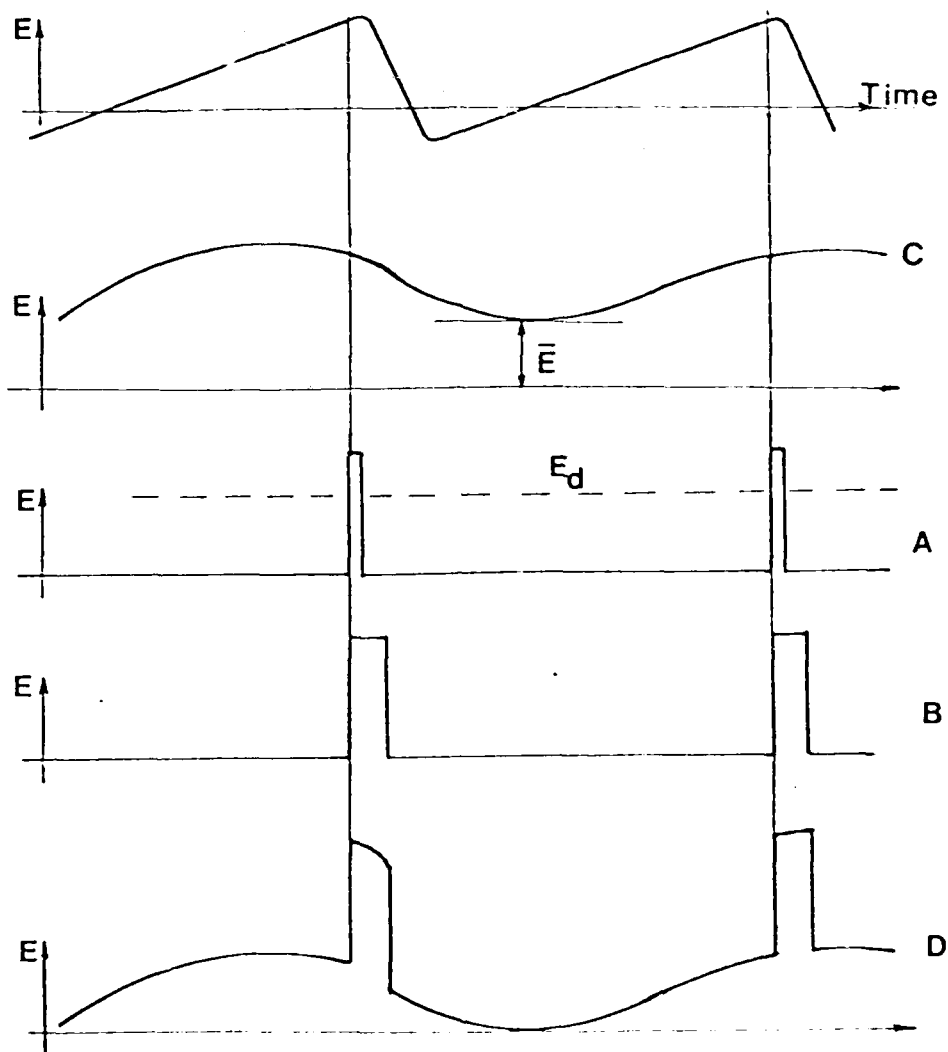


Fig. 4.6 Timing Diagram of the Pulse Marker.
Letters on the signals correspond to
points shown in Fig. 4.5.

added together to construct the output. Typical operation of the pulse marker which is closely related to its actual one in data acquisition is explained in Fig. 4.6.

Signal "A" in Fig. 4.6 is available by the scanner drive control called SYNC pulse and always occurs at the same location shown in that figure. The purpose of the lower branch in the pulse marker circuit diagram is to generate a variable pulse width controlled via a capacitor box (Fig. 4.6 b).

In data acquisition, the input signal (c) in Fig. 4.6 is the analog output of the counter processor. The voltage variation of the counter analog output for the settings used in the data acquisition was within 3.5 ± 1 volts. Since better voltage resolution (.0005 volts) was available working on ± 1 volt operation range of the fast A/D converter, the upper branch of the pulse marker circuit was added to shift the input signal (c) by an appropriate value, E, in order to bound this input signal within ± 1 volt range.

If the voltage level at "A" in Fig. 4.5 exceeds the adjustable discrimination voltage, E_d , then the output of the comparator goes high and remains there and finally drops to zero (low) when the voltage level at "A" goes lower than E_d . Theoretically, as far as data acquisition is concerned, one may not need a comparator; but, it was added since this same circuit was used for calibration, and this additional feature was found to be practicable.

4.4.2 Data Acquisition Logic and Procedure

The whole idea is that if one knows the position calibration line and the sawtooth position waveform, one can find the position corresponding to each valid velocity measurement in this scanning system. Figures 4.7 and 4.10 explain the idea. Step by step details of the procedure will follow.

As mentioned before, data acquisition relies heavily upon the linearity and repeatability of the sawtooth position waveform of the scanner. The knowledge of this waveform is needed for finding the position corresponding to each piece of computer-stored points (output of A/D1 in Fig. 4.7). In fact, only the validated velocity measurements that occur during upward scan of the measurement volume are of interest. Therefore, software was written to sample the sawtooth waveform and to compute the slope, intercept, minimum, and maximum voltage for the upsweep section of this waveform (statistical analysis). The results of this analysis showed that the maximum rms of the voltage variations at a given phase on the upsweep part did not exceed 0.2% of the mean voltage value in that same phase which represents the repeatability of the waveform.

Although the shape and the frequency of the sawtooth waveform are adequately stable, but the whole waveform might shift up or down either manually or by itself (Fig. 4.8), what it basically means is that the intercept for the upsweep section of the sawtooth waveform changes in time. The knowledge of the intercept at the time when each record of the frequency data is taken would be essentially important for finding the position corresponding to each frequency data point, see Figs. 4.8 and 4.10.

The SYNC pulse of the scanner driver can be used to keep track of the amount of the voltage shift. The voltage corresponding to the time when SYNC pulse occurs is called "Reference Voltage", Fig. 4.8. From the statistical analysis of the sawtooth waveform, one has slope, intercept, and the reference voltage at the time this waveform was sampled by the computer. The difference between the reference voltages for each record of the frequency data acquisition (shown as solid line in Fig. 4.8) and that of the previously known value when the sawtooth waveform was sampled for statistical analysis (broken line, Fig. 4.8) determines the correction to the intercept for the upsweep part of the waveform.

To summarize, the first step in the data acquisition is position versus voltage calibration; the second step is the statistical analysis on the scanner sawtooth waveform; and, finally, the third step is the acquisition of the frequency voltage from the counter. Figure 4.7 shows the block diagram for the final step of the data acquisition.

In Fig. 4.7 the voltage output of the LDA processor (TSI counter), which is proportional to the Doppler frequency or velocity of the particles (fluid), is shifted by the pulse marker (to be within ± 1 volt) and is added to the marker-pulse (Figs. 4.6 and 4.10). It is important that the pulse width of the marker-pulse be greater than the period of the pulses used for sampling in A/D 1 (section 4.5).

The final phase of data acquisition starts by acquiring 100 samples from the reference voltage, just before the frequency data is acquired, using A/D2 with SYNC as its sampling pulse (Fig. 4.7), then switching to the A/D1 to acquire a single record of 17500 points, with a controllable sampling period (pulse generator) of T_{ext} , and, finally,

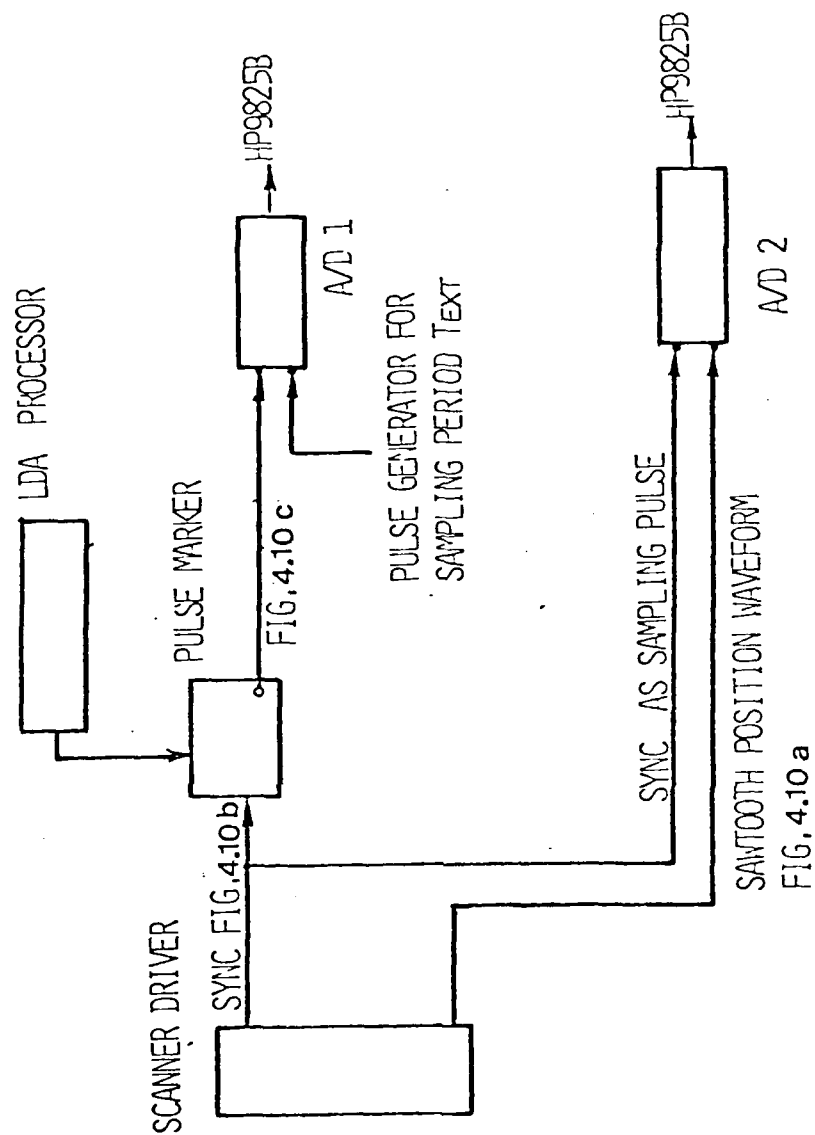


Fig. 4.7 Data Acquisition Block Diagram.
Pulse marker circuit stretches scanner SYNC pulse and adds analog output from counter.

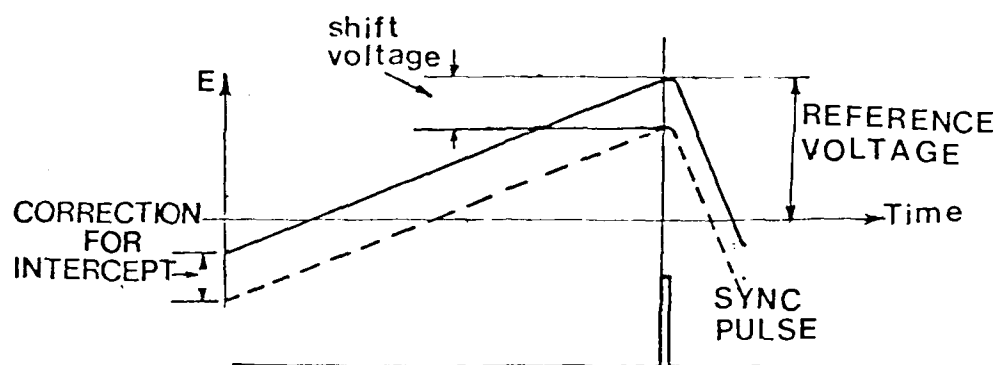


Fig. 4.8 Shift of the Sawtooth Waveform.

switching back to A/D2 and to acquire another sample of the reference voltage, see Fig. 4.7.

The average of the reference voltages sampled in the beginning and at the end of each record was used for data processing and monitoring purposes. The difference between this average reference voltage (when this record of frequency data is taken) and that known when statistical analysis on sawtooth position waveform is done (in second step of acquisition), determines the intercept correction in Figs. 4.8 and 4.10. Every pulse of the pulse generator, Fig. 4.7, triggers a new conversion cycle for the fast A/D converter which lasts 50 μsec . Hence, the period of the pulses, T_{ext} , cannot be less than 50 μsec . The choice of sampling period is essential both in the acquisition and processing of the data. Here, this choice of sampling period is discussed briefly in regard to the position uncertainty in this work.

Figure 4.9 (a) shows a short portion of the output of the pulse marker (see Fig. 4.10 c) which has been digitized by the A/D1. Processing logic in this work accepts the sample number 2 as the time when particle passes the measurement volume, while in reality the particle passed the volume sometime earlier. The maximum error in time when the particle crosses the intersection point of the two laser beams is equal to T_{ext} .

If the measurement volume scans a length equal to R mm with frequency of f_s using sawtooth internal generator of the scanner, then the distance travelled by the measurement volume, ΔY_R , in the time interval of T_{ext} is (Fig. 4.9 b):

$$\Delta Y_R = [R/(1-T_R/T_S)] f_s T_{\text{ext}} \quad (\text{mm}) \quad (4.1)$$

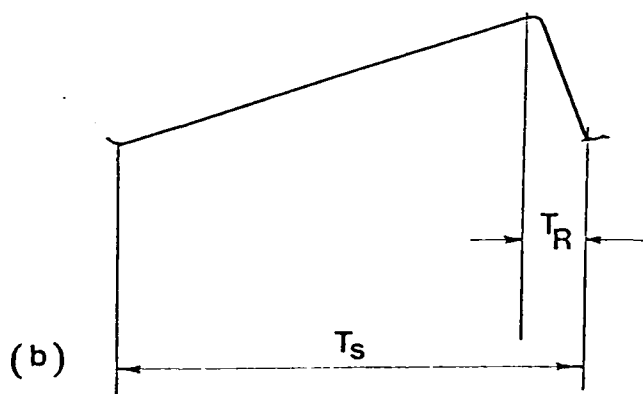
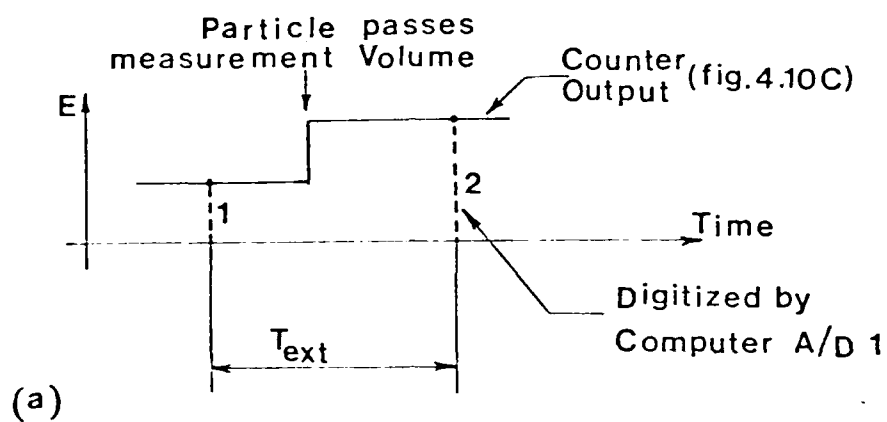


Fig. 4.9 (a) Short Time Representation of the Output of the Pulse Marker Output in Fig. 4.8.
 (b) Nomenclature Used on the Waveform.

Table 4.1 Distance travelled by measurement volume (ΔY_R) during sampling period of T_{ext} , for various scan frequencies (f_s) with scan range of 30.5 cm(=R).

f_s -Hz	T_{ext} μ sec							
	100	200	300	400	500	600	700	800
	ΔY_R - mm							
6	0.2	0.4	0.6	0.8	1.0	1.2	1.4	1.6
10	0.3	0.7	1.0	1.3	1.7	2.0	2.3	
15	0.5	1.0	1.5	2.0	2.5	3.0		
20	0.7	1.3	2.0	2.6	3.3			
30	1.0	2.0	3.0	4.0				
50	1.6	3.3	5.0					
60	2.0	4.0						
70	2.3							

For any arbitrary scan range, L-cm, one can use the above table with the correction equation $\Delta Y_L = \Delta Y_R(L/R)$.

The value of $1 - T_R/T_S$ is .921 for 15 Hz frequency of scanning and remains fairly constant for the wide range of frequencies (Fig. 4.9 b).

Table 4.1 shows the distance travelled by the measurement volume during sampling period for various scan frequencies and sampling periods, T_{ext} (R is taken as 30.5 cm.). Since the beam diameter is approximately 2 mm, the T_{ext} for each scan frequency is chosen so that the position uncertainty, due to measurement volume movement, becomes less than the beam diameter. Hence, before the beginning of the final stage of data acquisition, one should make an appropriate decision of a value for the sampling period. There is another important determining factor for the value of T_{ext} which will be discussed in section 4.5.

4.5 Data Processing

Figure 4.10 shows the details of the processing. The reference voltage for each data record, section 4.4.2, is used to find the correction on the intercept for the ramp section of the sawtooth waveform for each particular record (Fig. 4.10). Note that the reference of time for calculating the slope and intercept for the upswing part of the waveform is taken at the lowest voltage of the scan on the ramp.

The height of the marker-pulse (stretched SYNC pulse, Fig. 4.10) is such that it always exceeds the saturation voltage level (+1 volts) of the A/D1. This pulse marks the end of each upswing scan cycle which is digitized and stored by the computer. For this reason, the width of the marker-pulse must be slightly greater than T_{ext} to insure that the A/D1 samples at least once on the marker-pulse.

Data processing program starts by scanning backward in time through the stored record searching for the sampled marker-pulses and

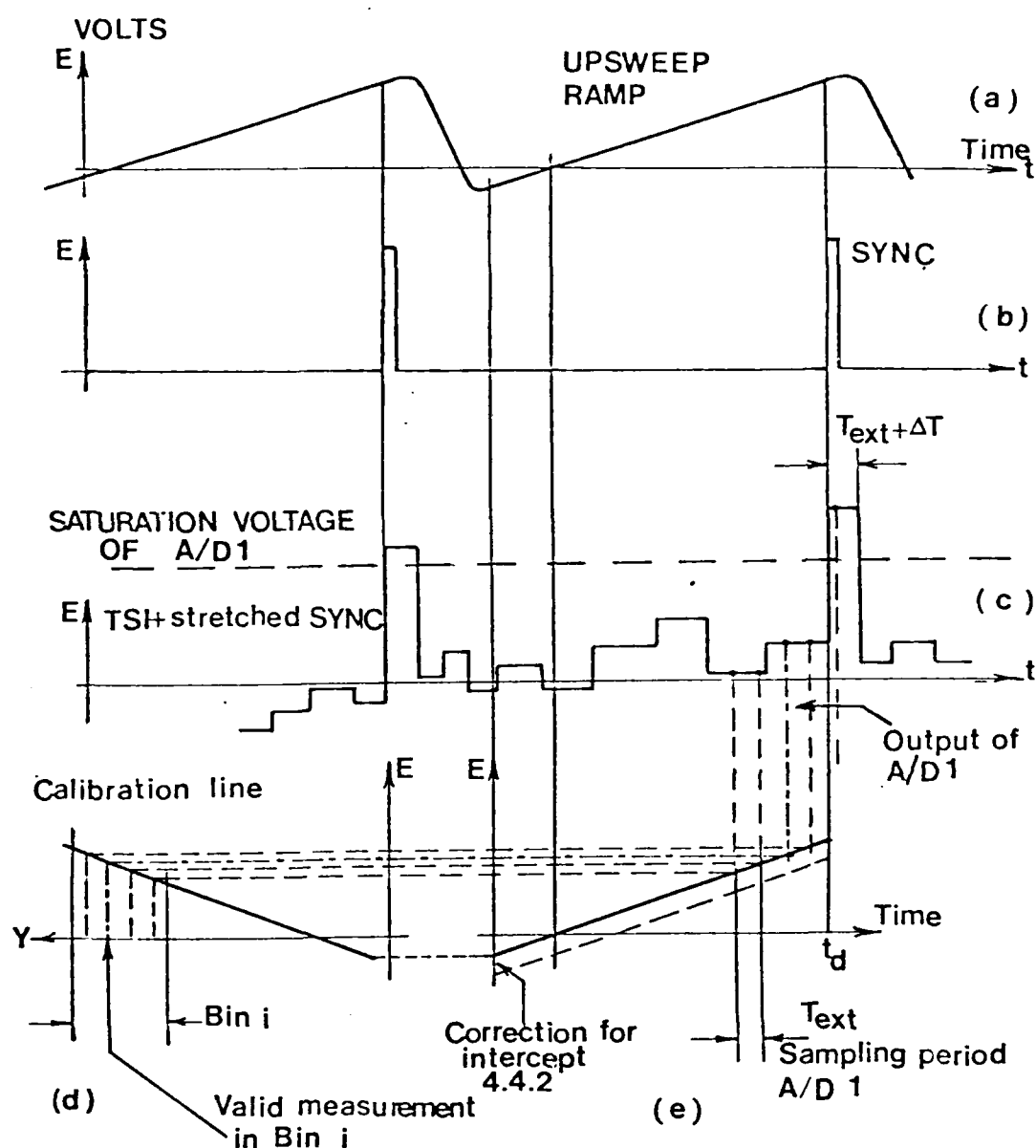


Fig. 4.10 Data Acquisition and Processing Logic and Signals.

- (a) Internal sawtooth waveform of scanner.
- (b) SYNC pulse from scanner.
- (c) Sum of the analog output from counter processor and the stretched SYNC pulse (Marker-Pulse).
- (d) Scanner voltage vs. position (Calibration Line).
- (e) Sampled data points from (c) with corresponding position voltage on the linear least-square fit waveform.

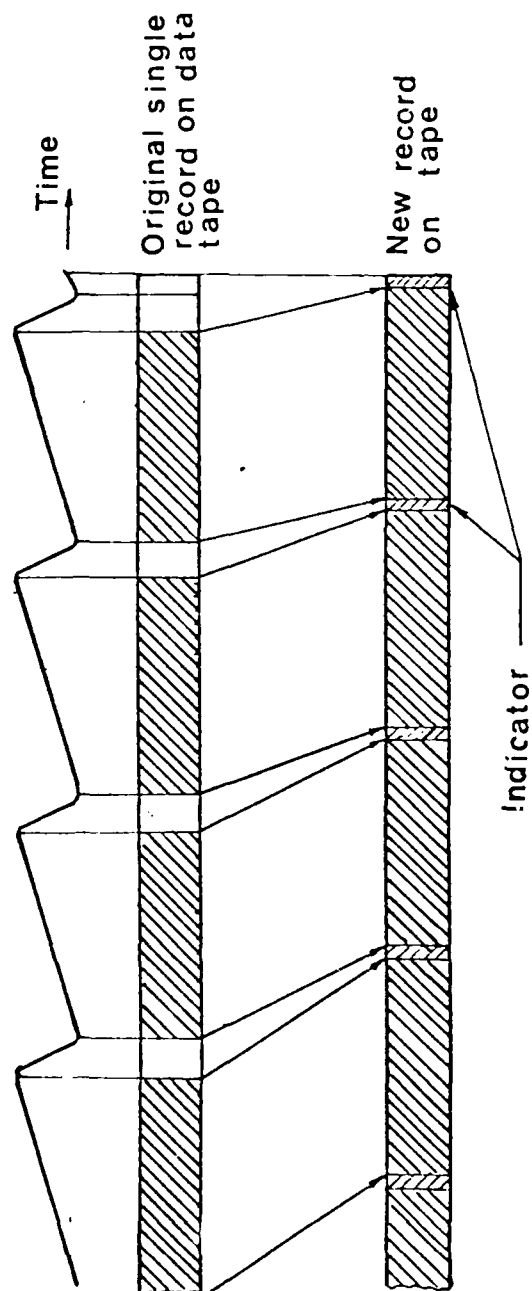


Fig. 4.11 Schematic Diagram Showing Creation of New Record Containing the Useful Data (only on Upsweep).

creating a new record by eliminating the sample points on the retrace of each and every cycle in the record. In this new record, there is an indicator for the beginning of each upswing scan which at the same time represents the end point of the previous scan cycle, see Fig. 4.11.

One knows the corrected intercept, slope, the time corresponding to the maximum location of scanning (t_d in Fig. 4.10), and the sampling period, (T_{ext}) from data acquisition process. Therefore, one can determine the position corresponding to each computer-stored point (output of A/D 1) by using calibration line as shown in Fig. 4.10.

The total scan length is divided to a certain number of position "bins". The processing program searches through the computer-stored points for validated velocity measurements in each bin by finding the voltage difference of the two consecutive samples, ΔE . If the absolute value of this difference is greater than a certain number, then the sample which occurred later in time is taken as the valid velocity measurement in that particular bin. Note that since velocity and Doppler frequency for a particle are related, thus the terms velocity measurement or frequency measurement are equivalent in this context.

Since the voltage resolution of the A/D1 is .0005 volt, the absolute value of the voltage difference ($|\Delta E|$) mentioned above should be greater than this number. In fact, it was found experimentally that the $|\Delta E|$ must be greater than or equal to 0.005 volt and less than 0.01, in order to pick the true validated velocity measurements. Note that the 0.005 voltage difference corresponds to approximately ± 0.061 m/s, using a $3.1 \mu\text{m}$ fringe spacing.

At the final stage of the data processing program, all of the validated velocity measurements for each "position bin" are used in

computing mean and RMS values for that particular bin. Furthermore, program prints out the number of valid measurements for each bin which is used for computing the data rate distribution (chapter V).

From the data processing logic, it is obvious that at least two computer-stored points are needed to determine a single validated measurement in each position bin (see Figs. 4.9 a and 4.10 d). If one wants to have greater than or equal to "S" number of computer data samples in each "position bin," then the sampling pulse period, T_{ext} , must be

$$T_{ext} < (.921/S)(T_s/N_b) \quad (4.2)$$

where T_s is the period of sawtooth scanning waveform, and N_b is the total number of position bins in the scan range (section 4.4.2). So the T_{ext} should be chosen such that to minimize the position uncertainty as well as satisfy equation 4.2.

Table 4.2 represents the maximum T_{ext} allowable in order to have at least three numbers of computer data samples in each position bin.

4.6 Static and Dynamic Check of the Entire System

Due to the lack of availability of the appropriate equipment, the data processing as explained in previous sections is somewhat complicated. Therefore, a test procedure was needed to check the proper operation of the whole system including the softwares.

There are two tests called static and dynamic checks. The

Table 4.2 Maximum sampling pulse period allowable in order to have
3 (=S) computer samples in each position bin using 30
(=N_b) number of position bins in scan range.

f_s -Hz	T_{ext} - μsec
6	1700
10	1000
15	682
20	512
25	409
30	292
40	256
50	205
60	171
70	146
100	102

static test has a two-fold purpose of voltage calibration as well as testing the system. The terminology of "static" and "dynamic" will be explained by the procedure of each test.

The static test procedure is to follow all the steps of data acquisition and processing but using a constant voltage from a DC power supply, instead of the TSI counter, as shown in Fig. 4.12. The input voltage is measured by a digital voltmeter (DVM).

The end result of the processing is the mean voltage for each position bin of the scanning which must remain the same for all position bins. The entire procedure could be repeated for various fixed input voltages and a voltage calibration line be derived. Figure 4.13 shows such a calibration line which later is incorporated in the data processing program.

The second test on the entire system uses the position waveform of the scanner, as the simulated TSI counter output, as shown in Fig. 4.14; and for that reason the test is called a dynamic test.

As the data processing logic works, see Fig. 4.10, if the software is to follow the logic, then one should not only obtain a line, if a plot of the mean value for each position bin versus position is constructed, but this line should represent the ramp section of the sawtooth waveform.

Figure 4.15 shows the results of such a test. The solid line represents the result taken from the statistical analysis on the waveform, see section 4.4.2.

4.7 Position and Velocity Uncertainty

In sections 4.4.2 and 4.5 concerning data acquisition logic and processing, it was referred that the major position uncertainty was due

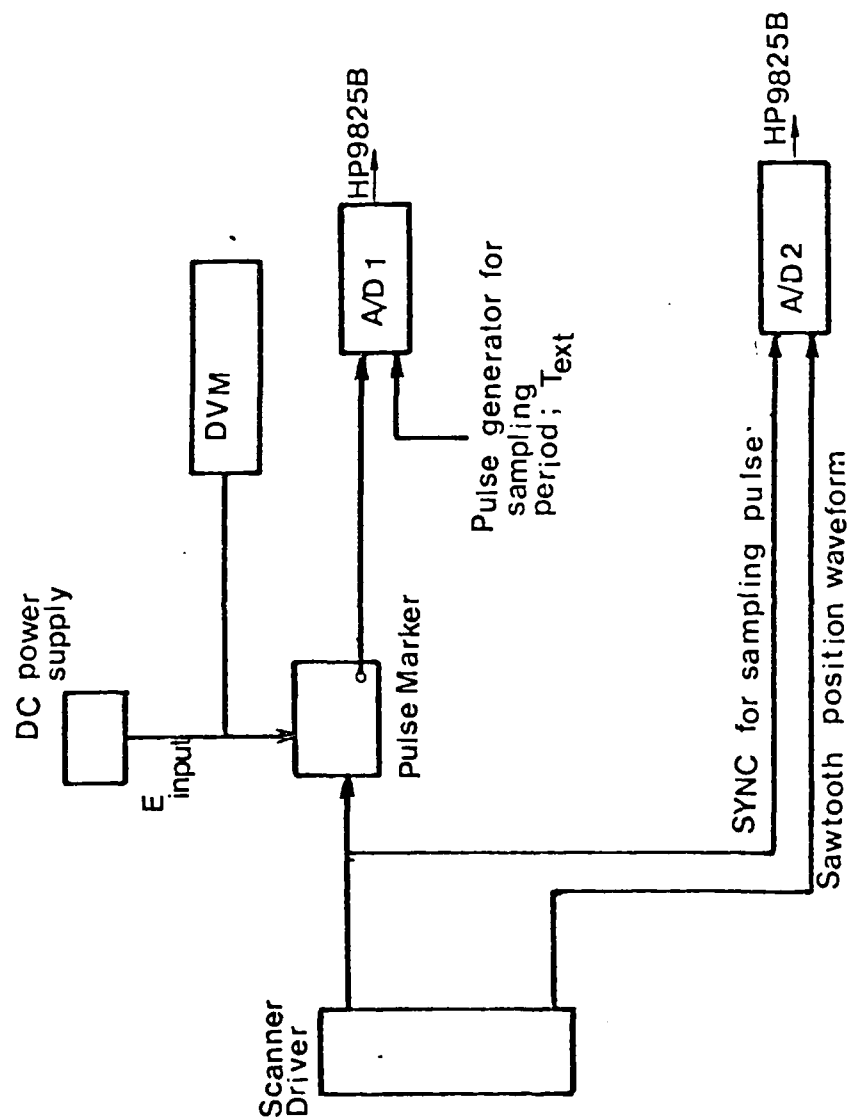


Fig. 4.12 Block Diagram for Static Test of the System.

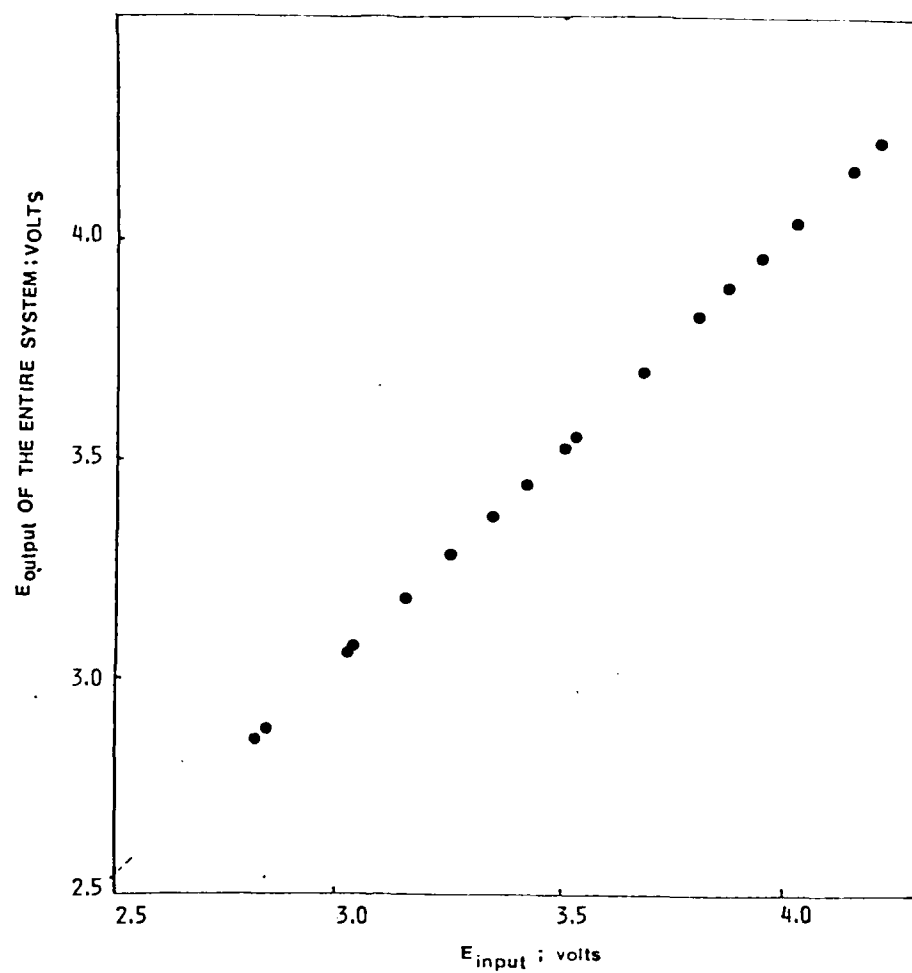


Fig. 4.13 Static Calibration of the Entire System.

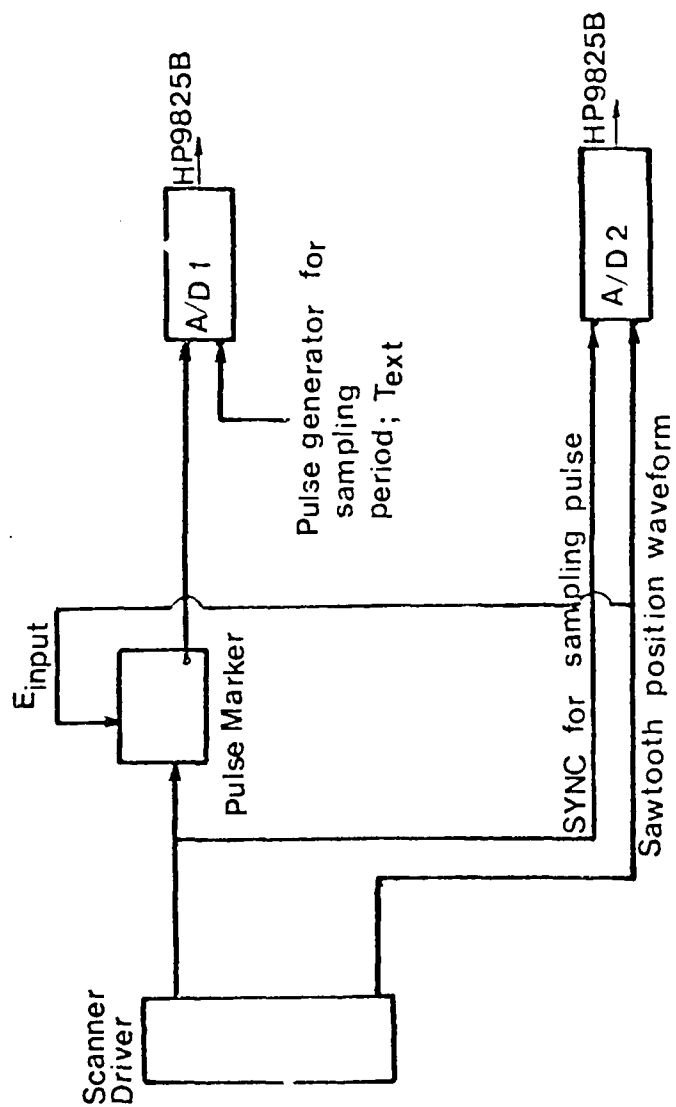
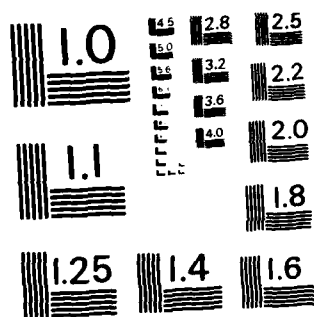


Fig. 4.14 Block Diagram for Dynamic Test of the System

AD-A130 923 SCANNING LASER DOPPLER ANEMOMETER AND ITS APPLICATION 2/2
IN TURBULENT SEPARA..(U) SOUTHERN METHODIST UNIV DALLAS
TX DEPT OF CIVIL AND MECHANICA.. B CHEHROUDI ET AL
UNCLASSIFIED JUL 83 SMU-WT-7 N00014-79-C-0277 F/G 14/2 NL

END
DATE
FILMED
6 83
DTIC



MICROCOPY RESOLUTION TEST CHART
NATIONAL BUREAU OF STANDARDS - 1963-A

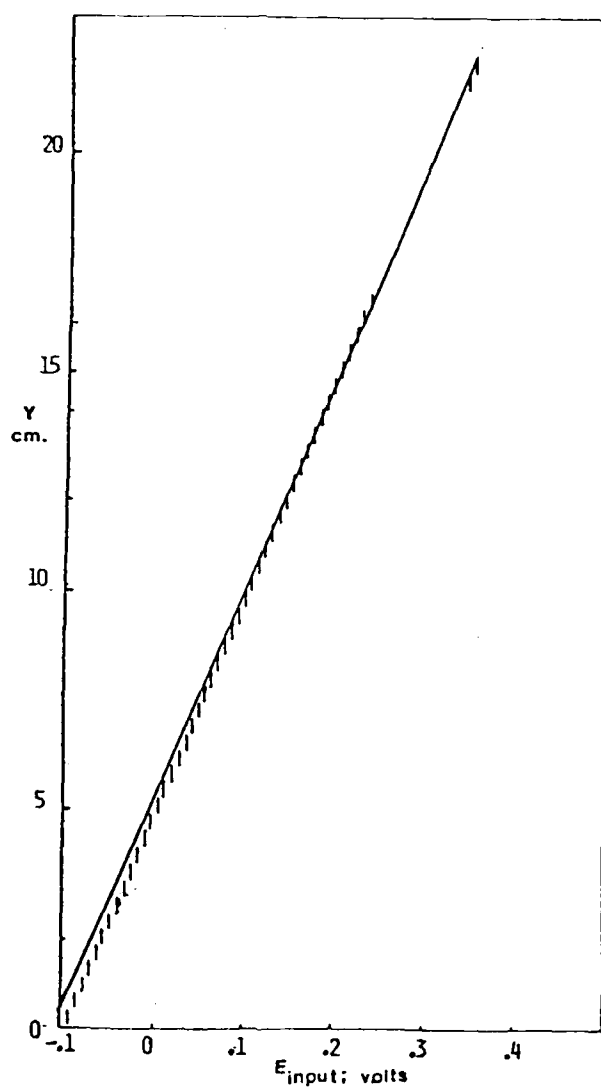


Fig. 4.15 Dynamic Test of the Entire System.
Solid line is the calibration line from
Fig. 4.10 .

to the technique used for determining the position corresponding to each counter validated velocity measurement (Fig. 4.10).

Table 4.1 shows the maximum position uncertainty associated with aforementioned processing technique in millimeter. Since the processing program accepts the point No. 2 in Fig. 4.9 (a) as the time when particle passes the measurement volume, therefore, one has the true position where the particle crossed the fringes as:

$$Y_{\text{true}} = Y_2 \pm d/2 - \begin{cases} \Delta Y_R \\ 0 \end{cases} \quad (4.3)$$

Where Y_2 is the position corresponding to the point No. 2 in Fig. 4.9(a), d is the beam diameter, and ΔY_R is given in Table 4.1. According to the uncertainty analysis of Kline and McClintock (1953), in all of the experiments in this work the T_{ext} in Table 4.1 is chosen such that the maximum position uncertainty due to measurement volume movement is less than the beam diameter. Hence, the dominant uncertainty would be due to the large beam diameter itself.

Another source of position uncertainty is due to the fact that a linear least square fit to the ramp upswing of the sawtooth waveform is used which even for high scan frequencies (60Hz) does not exceed 1 mm, and therefore is negligible.

The uncertainty due to velocity is mainly associated with the counter processor. The counter measures the time for 32 cycles and compares this time to that of 16 cycles. The comparison is done on the frequencies calculated based on 32 and 16 cycles by actually dividing

the two numbers. The comparison limit can be set on the counter from 1% to 20% discrepancy between the two values. The equation that determines the velocity can be derived using equations (2.1) and (3.1)

$$(15.2 \times 10^6 - f \cdot 10^6) \cdot (\Delta x \cdot 10^{-6}) = U \quad (4.4)$$

in which f is the Doppler frequency measured by counter in MHz, Δx is the fringe spacing in micron, and U is the instantaneous streamwise velocity in m/sec.

In equation 4.4, an error in the measurement of the Doppler frequency of $\pm df$ is equivalent to the velocity uncertainty of $\pm 10.2 df$ using fringe spacing of $3.1 \mu\text{m}$. For 1% comparison limit the $\pm df$ is about .150 MHz, meaning that the associated velocity uncertainty is at most $\pm .45$ m/sec.

The TSI counter uses a 250 MHz clock to measure the frequency. Therefore, uncertainty due to ± 1 count ambiguity, Durst et al. (1976), is almost $\pm .05$ m/sec for maximum forward flow, which is negligible compared with the comparison uncertainty of $\pm .45$ m/sec.

CHAPTER V

EXPERIMENTAL RESULTS AND DISCUSSION

5.1 Mean and RMS Values Using Scanning LDV

There were several questions raised concerning the operation of this new design: 1. Is this system reliable for any velocity measurement? 2. What is the maximum scan frequency achievable in this design? 3. What are the limitations? Therefore a series of experiments were made in an attempt to answer the above fundamental questions.

For comparison purposes, in all of the experiments the results of the pointwise measurements using the same scanning LDA setup are compared with that of scanning data for various frequencies in a turbulent separated flow generated in the SMU wind tunnel.

Figures 5.1 and 5.2 show mean and rms velocity profiles for each position bin and for various scan frequencies. In each case the total record consists of several number of smaller data records taken during experiment; the total record time in previous figures for each frequency was at most one minute. The boundary layer thickness for Figs. 5.1 and 5.2 is about 35 cm. Consequently due to variation of the vertical distance of the turbulent-nonturbulent interface and the fact that much of the baby powder remains inside the turbulent boundary layer, the mean values are biased near $Y \approx 25$ cm, besides, the particle concentration

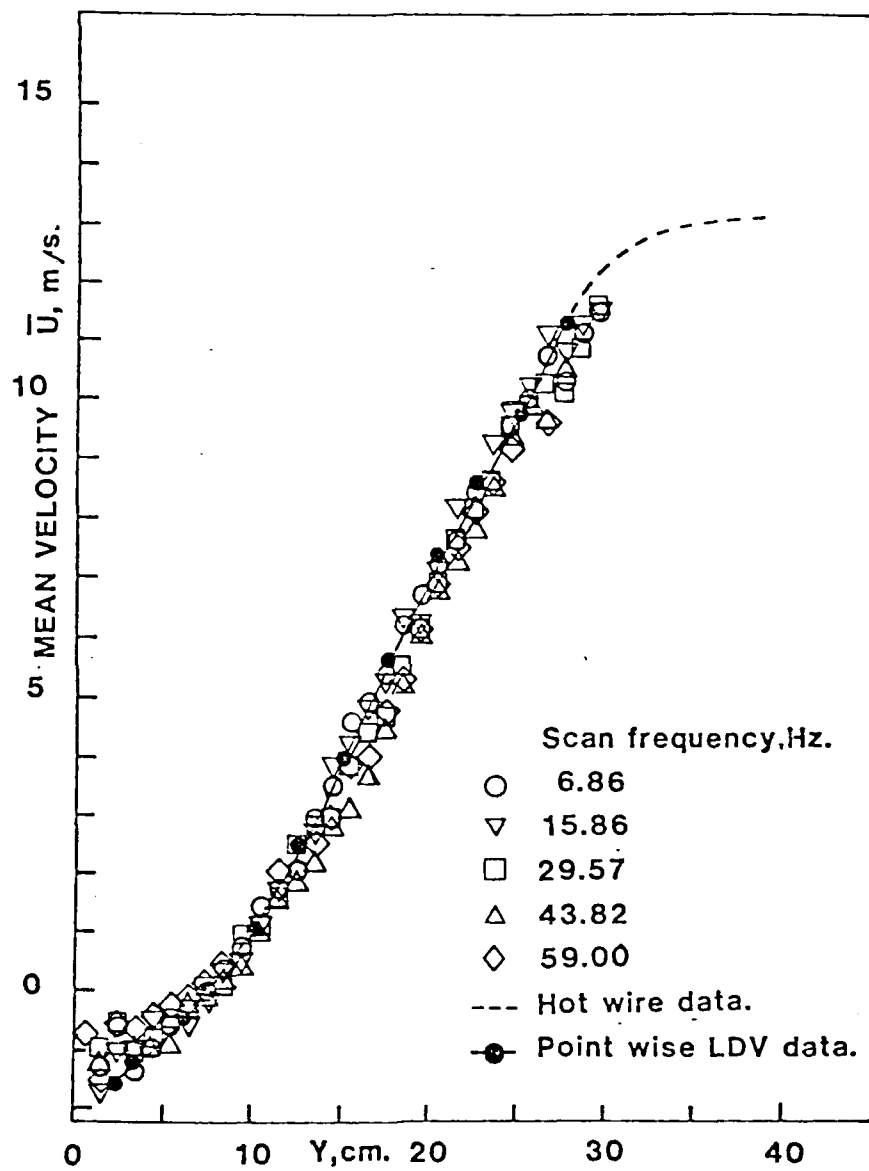


Fig. 5.1 Mean Velocity vs. Position for Various Frequencies at $X=436.9$ cm (172 in) .

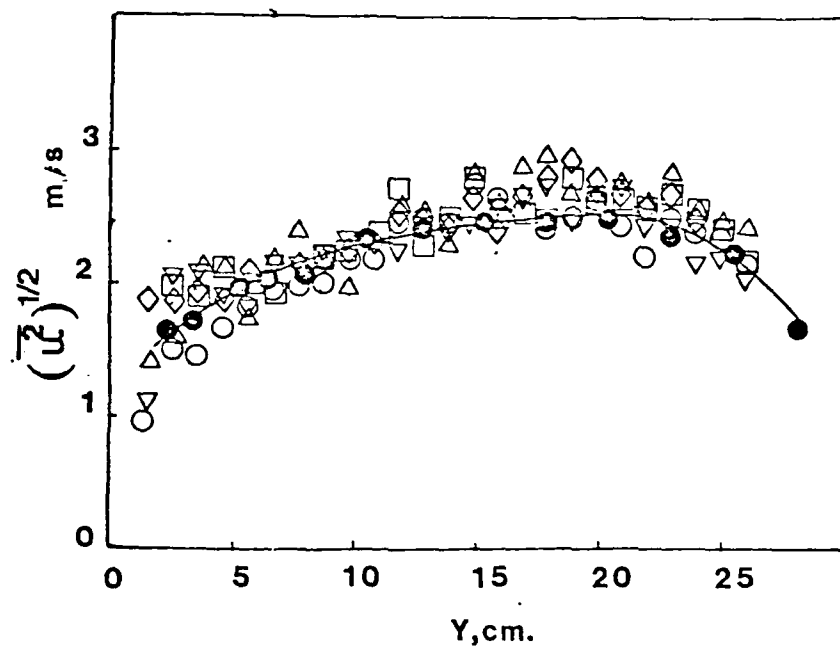


Fig. 5.2 RMS of the Velocity Fluctuation for Various Frequencies.

For legend see Fig. 5.1 .
X-location= 436.9 cm(172 in).

According to Yanta and Smith (1973) taking a flow with 5% level of turbulence, a sample size of 166 is necessary to obtain a .99% confidence level that the experimental mean differs from the true population mean by less than 1%. But for population's standard deviation, 3150 sample size is required for a confidence level of 95% and an error of 2.5%. The fact that one needs larger sample size for standard deviation than the mean, can also be seen in a work by Bates and Hughes (1976), in which they concluded that for sample size of 3500 and above, the turbulence intensity shows no variation with sample size. One can see, in their work, that, with sample size of 500, the errors for mean and turbulence intensity are in the order of 4% and 22% respectively.

The maximum number of validated counter measurement for each position bin in Figs. 5.1 and 5.2 does not exceed 350. Near the wall and edge of the boundary layer, data rates are low; therefore, one has smaller sample size for corresponding position bins, which, in turn, means higher percentage error. Despite that, good agreement exists between the mean values, Fig. 5.1, up to a scan frequency of 59 Hz (scan speed of 19 m/sec.)

One should consider that as the measurement volume scans with this rapid velocity through the highly turbulent separated flow the counter processor receives variable signal-to-noise (SNR) ratio signals due to measurement volume movement and from variations in seeding density and/or particle size. Orloff et al. (1974) also reported these effects.

The rms of velocity fluctuations shows more scatter, but is within measurement uncertainty (section 4.7); and as mentioned before, one reason is due to insufficient number of validated counter measurements in each bin (small sample size). This is especially seen for the

position bins corresponding to the extremes of the scanning range. Better results were taken by proper focusing of the image of the measurement volume on PM-tube and increasing the sample size (Figs. 5.3 and 5.4).

Once the proper operation of this design was established, the system was used to survey the flow in the SMU wind tunnel. Figures 5.3 and 5.4 show the mean and rms of the velocity fluctuations at four different streamwise locations in the wind tunnel, using scanning LDA, as compared with those of pointwise velocity measurements (using the same scanning arrangement). The sample size for each position bin does not exceed 600, and for this reason, all of the pointwise measurements are with sample size of 500 to compare with those of scanning data.

Figure 5.5 shows the intermittency factor, γ_{pu} , the fraction of time when flow is in the main stream direction, for three streamwise stations in the wind tunnel (using the same set of data as Figs. 5.3 and 5.4). Reasonably good agreements are seen except very near the wall. For $x = 317.5$ cm, intermittency factor is 1 throughout the boundary layer.

If one divides the total number of valid velocity measurements in each position bin to the total time that the measurement volume spends in that bin for the entire record, T_{tb} , one will have an idea of the data rate and/or concentration throughout the boundary layer. Figure 5.6 shows the result of such a parameter for four stations in the wind tunnel. It is clearly shown in Fig. 5.6 that the data rates (or sample size) for position bins in the extremes of the scan range are very low. One can increase the data rates by increasing the baby powder

Table 5.1 Legend for figures 5.1 to 5.6

x-Location cm.(in.)	Scan frequency f_s - Hz.	Counter amplifier gain- dB		$+T_{tb}$ sec.
317.5 (125)	55.7	2.3	●	2.26
355.6 (140)	56.6	3.3	◆	2.76
396.2 (156)	58.6	3.5	▲	1.07
436.9 (172)	58.2	3.9	■	1.40

Corresponding pointwise measurements using the same scanning set-up with sample size of 500 each.

○

$+T_{tb}$ is the total time spent by the measurement volume in a bin.

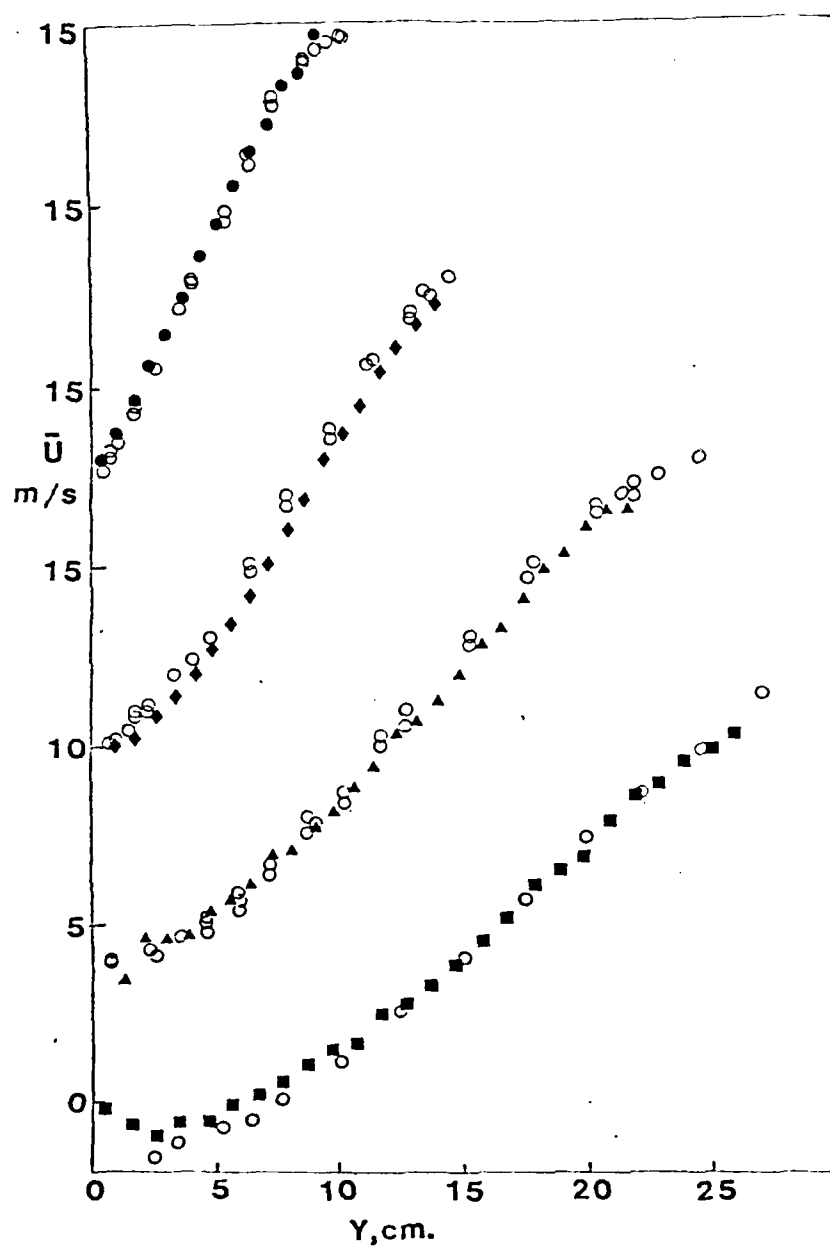


Fig. 5.3 Mean Velocity vs. Position at Four Different Streamwise locations.

For legend see Table 5.1 .

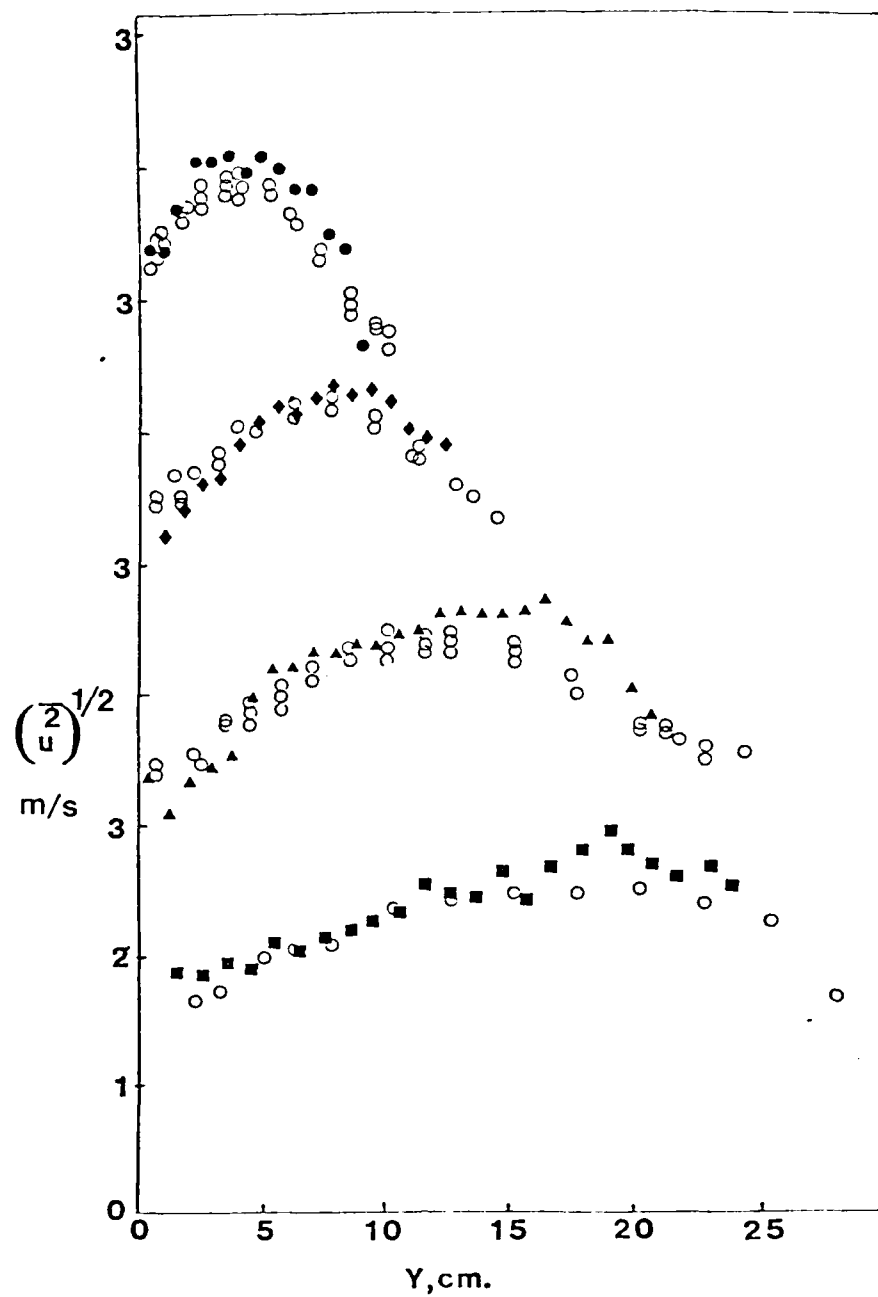


Fig. 5.4 RMS of Velocity Fluctuations at Four Different Streamwise Locations.

For legend see Table 5.1 .

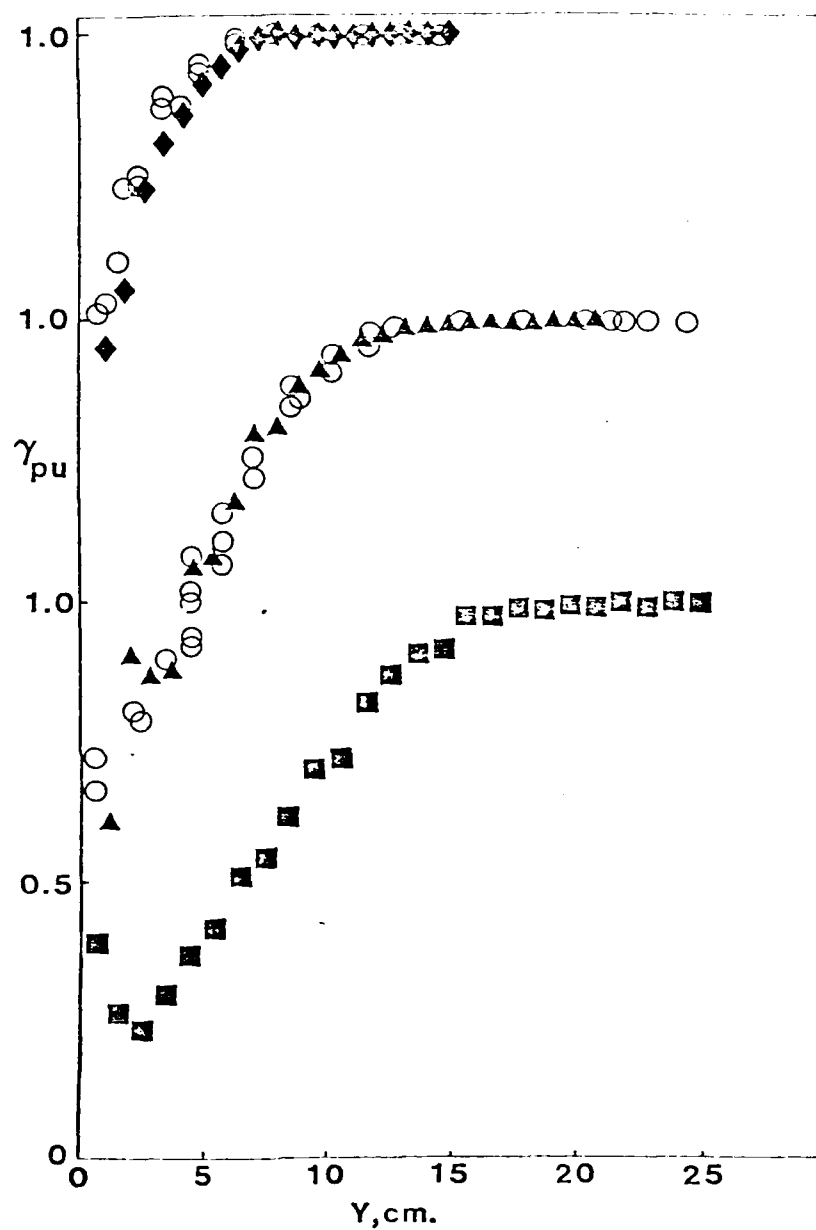


Fig. 5.5 Intermittency Factor vs. Position at Four Different Streamwise Location.

For legend see Table 5.1 .

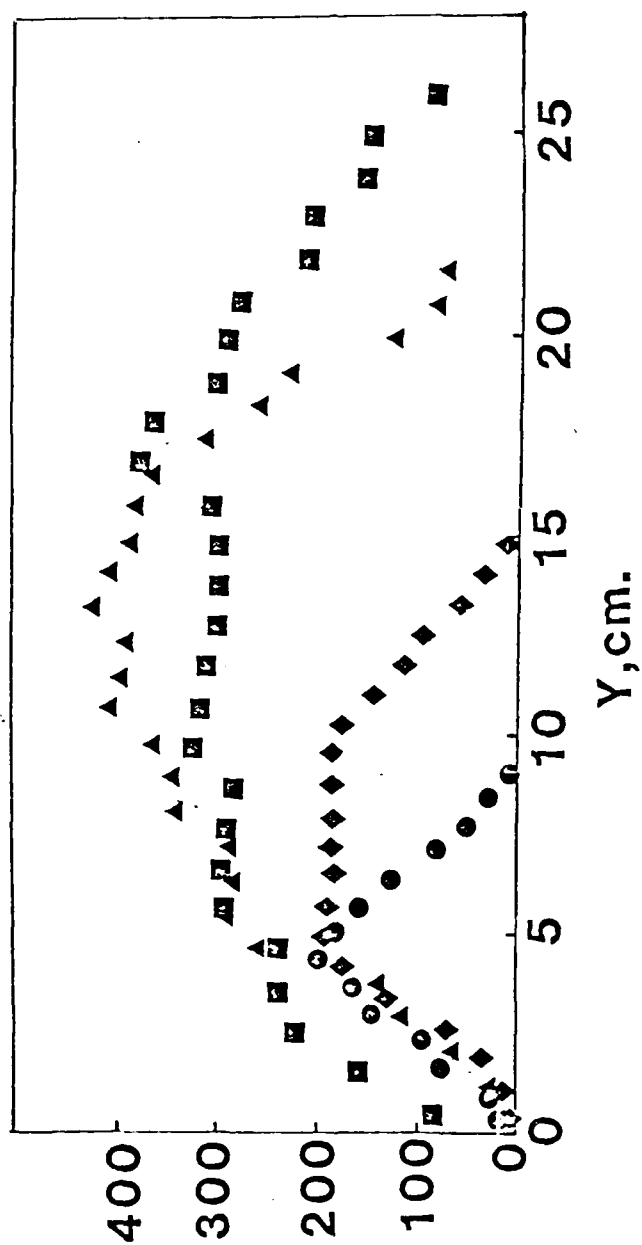


Fig. 5.6 Total Number of Valid Measurements / Total Time Spent
by Measurement Volume in a Bin vs. Position.
For legend see Table 5.1 .

concentration and/or increasing the gain of the counter amplifier. However, there is an optimum state that if one increases the gain it will amplify the noise. This can practically be detected by the departure of the mean velocity profile found by scanning from the 'true' profile. On the other hand, if one increases the baby powder concentration above certain level, it either saturates the PM-tube and/or increases the noise. In all of the experiments reported here in the scanning mode, the following fixed settings are used:

Laser Power	:	600 mw
PM-tube Voltage	:	-1690 volts
Average baby powder concen- tration	:	33 mg/m ³

The scanning system is very sensitive to the gain of the counter processor amplifier, and for each experiment its value in dB is written on the Table 5.1.

As shown in Fig. 3.12 section 3.2.3, the scanner position waveform remains linear up to 156 Hz (there was no attempt to examine its linearity for higher than 156 Hz.), and there is no mechanical problem. However, as one increases the scan frequency, one should ensure that there are enough number of fringes crossed by the particles. If using the processing technique explained here, one needs faster A/D and computer, see section 4.7.

5.2 Some Characteristics of the Flow Field in this Work

Table 5.2 shows the boundary layer integral parameter at the same four streamwise locations using pointwise measurements shown in Figs. 5.3. Flow is completely attached at $x = 317.5$ cm, and intermittency factor, γ_{pu} , is 1 throughout the boundary layer.

To show that the flow is well behaved in this work, results taken at $x = 317.5$ cm are compared with the mean velocity correlation suggested by Perry and Schofield (1973) for strong adverse pressure gradient turbulent boundary layers. Figure 5.7 shows the results of the non-dimensionalized velocity versus normalized position in which solid line is the correlation suggested by Schofield (1980)

$$\frac{U_{\infty} - \bar{U}}{U_s} = 1 - 0.4 (y/\Delta)^{1/2} - 0.6 \sin [(\pi/2) (y/\Delta)] \quad (5.1)$$

where U_s is a scaling velocity and Δ is an integral layer thickness $[\Delta = 2.86 \delta_1 (U_{\infty}/U_s)]$. At this station U_s/U_{∞} was calculated to be .99.

The spectrum function $F(n)$ of \bar{u}^2 is defined as

$$\bar{u}^2 \int_0^{\infty} F(n) d n = \bar{u}^2 \quad (5.2)$$

or in other form:

$$\bar{u}^2 \int_0^{\infty} n F(n) d (\ln n) = \bar{u}^2 \quad (5.3)$$

where n is the frequency in Hz. The spectrum function $F(n)$ was obtained at four streamwise locations for $\gamma_{pu} \approx 1$ using hot wire anemometer. The

Table 5.2 Boundary layer integral parameters

x-cm (in)	$\delta_{.99}$ -cm.	δ_1 -cm.	δ_2 -cm	H
317.5 (125)	10	3.99	1.67	2.39
355.6 (140)	15	8.34	2.30	3.63
396.2 (156)	24.5	14.96	3.11	4.81
436.9 (172)	32.5	19.23	2.99	6.43

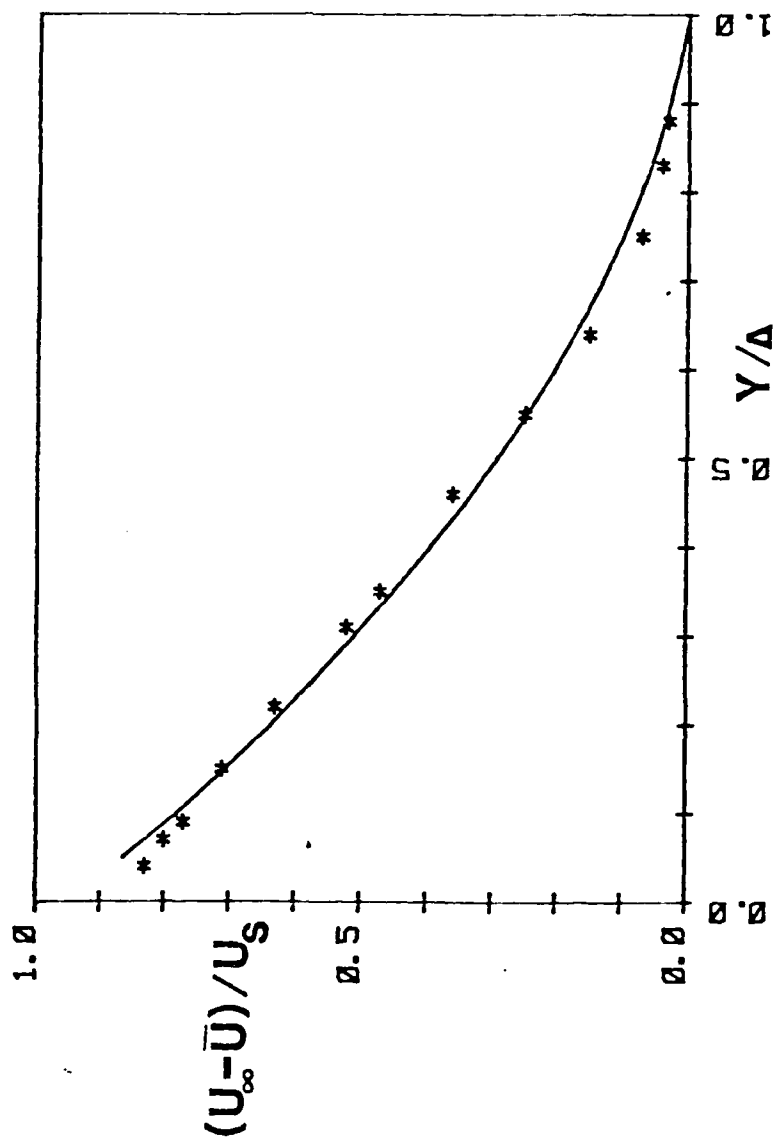


Fig. 5.7 Comparison of the Data at $X=317.5$ cm with the Perry and Schofield (1973) Mean Velocity Correlation (Solid Line).

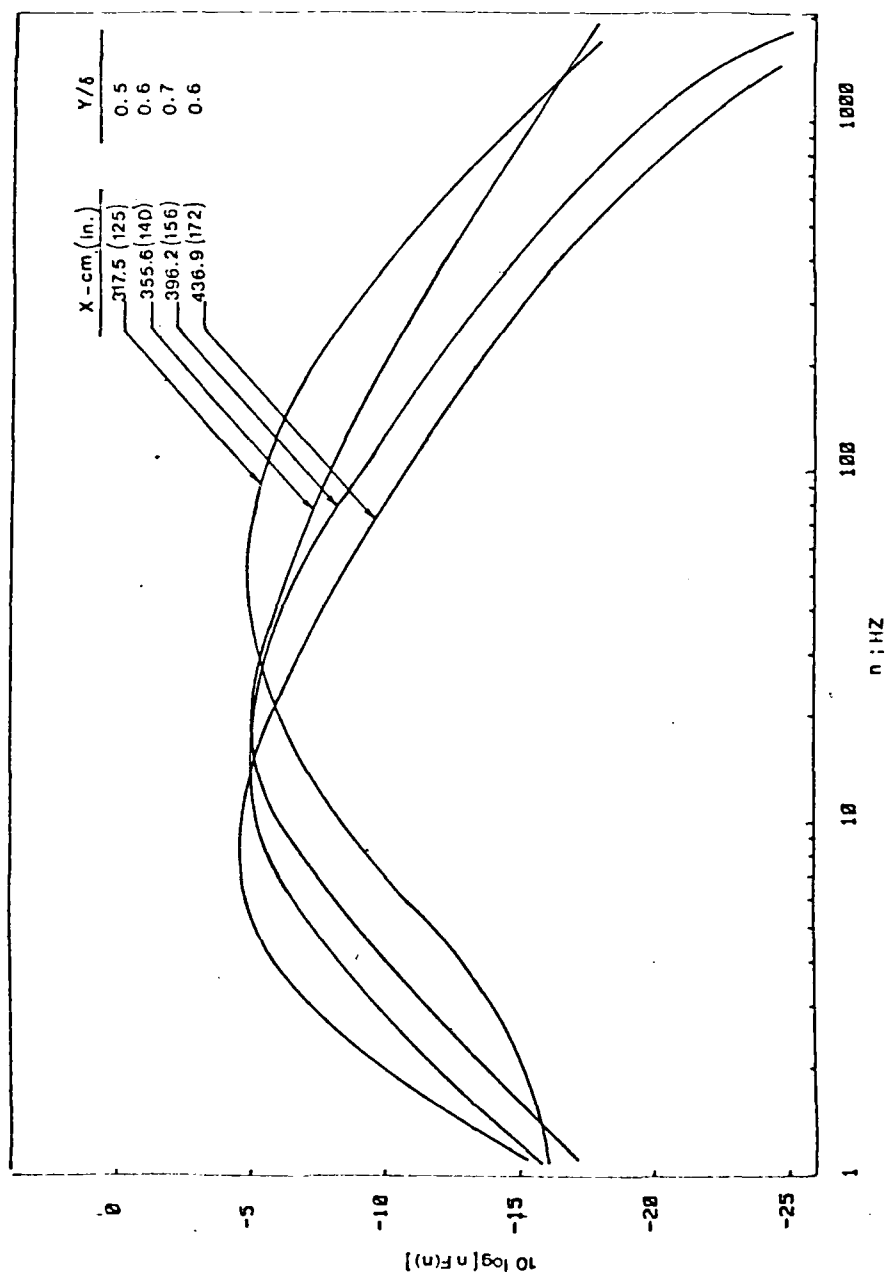


Fig. 5.8 Spectra of $\overline{u^2}$ at Four Streamwise Positions.

spectra shown in Fig. 5.8 are smooth lines drawn through the experimental curves. The frequency corresponding to the maximum of the curves in Fig. 5.8 (n_{max}) shifts towards the lower frequencies as flow enters the separation zone. This means that the large-scale energy-containing eddies grow in size in separated region. In addition, the average frequency characteristics of the large energy-containing eddies in the separated zone is seen to be in the order of 15 Hz. Hence, on the average, with 60 Hz scan frequency, one has four scans through these eddies which may reveal more information about their structure.

5.3 Quadrant Analysis and Space-Time Correlations

The qualitative investigations by Simpson et al. (1981) showed that for the case where the thickness of the backflow region is small compared with the turbulent shear-layer thickness; the backflow region is supplied locally by outer region large-scale structures. The scanning LDA system used here can be useful for this kind of investigation provided "adequate" data rates are achievable. The quadrant analysis and space-time correlation measurements are attempts toward this goal using scanning LDA.

Since the maximum number of validated measurements, for a given scan, in this work was not more than 20, one needs to break the scan range into few intervals, Fig. 5.9, to be able to perform any quadrant and space-time correlation analysis.

A point in a quadrant plane shows the departure of the instantaneous streamwise velocity from the corresponding mean value in a given interval, Fig. 5.9, versus the same departure for another interval in a single scan of the measurement volume ($\bar{U}-U$). Figures 5.10 to 5.16 show the results of quadrant analysis using all scans in a data record for

the streamwise location of 396.2 cm. The number of points in each quadrant is written in the corresponding quadrant, and the normalized space-time correlation is written in the parenthesis in the first quadrant. The logic in the quadrant analysis program examines, first, for any valid velocity measurements in the interval on the abscissa of Figs. 5.10 to 5.15. If there is any, then the program searches for valid measurements on the same scan in the interval on the ordinate, and only if there is at least one, then points are marked on the quadrant plane and are also used for correlation calculations having zero cycle delay. The same logic is used for measured velocities in two intervals having a pre-chosen number of cycle forward delay, see Fig. 5.17, in space-time correlation calculations.

As it is shown in Fig. 5.17, one can find space-time correlation coefficient between measured velocities in intervals 1 and i for the same cycle throughout the entire record (zero cycle delay), or correlation coefficient between velocities in the aforementioned intervals having any desired number of forward-cycle delay. Theoretically, space-time correlation for two positions having τ = time delay is defined as:

$$R_{uu}(y_i - y_1, \tau) = \frac{1}{\left[\overline{u^2(y_1, t)} \cdot \overline{u^2(y_i, t)} \right]^{\frac{1}{2}}} \lim_{T \rightarrow \infty} \frac{1}{T} \int_{t_0}^{t_0 + T} u(y_1, t') \cdot u(y_i, t' + \tau) dt' \quad (5.4)$$

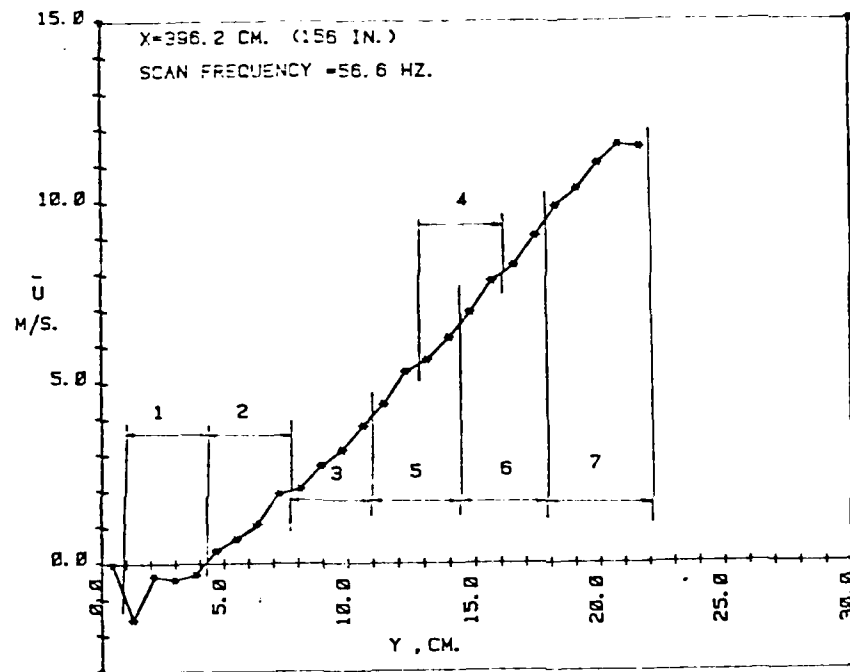


Fig. 5.9 Mean Velocity vs. Position from Scanning LDA Showing the Spatial Intervals Used for Figs. 5.10 to 5.16.

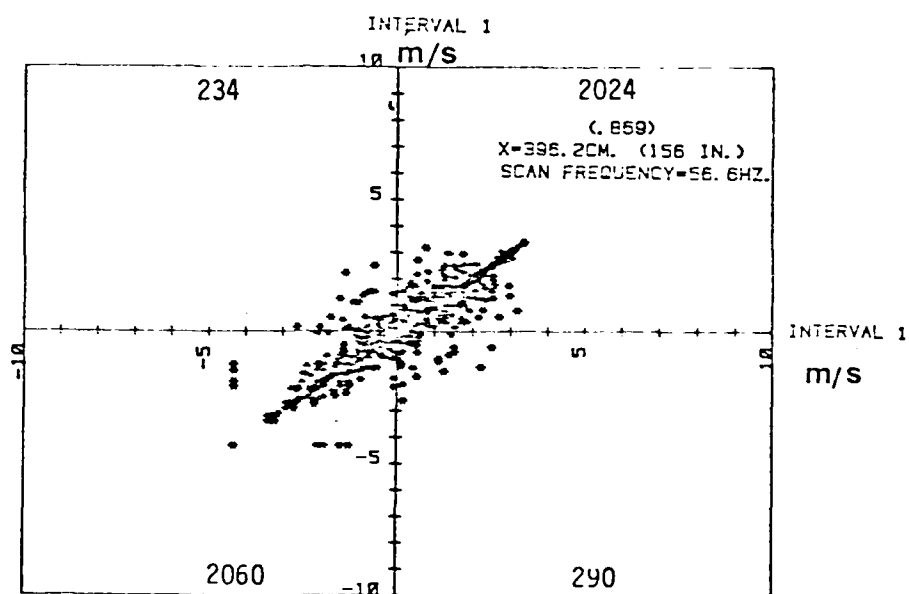


Fig. 5.10 Quadrant Analysis (Section 5.3).
For intervals information see Fig. 5.9 .

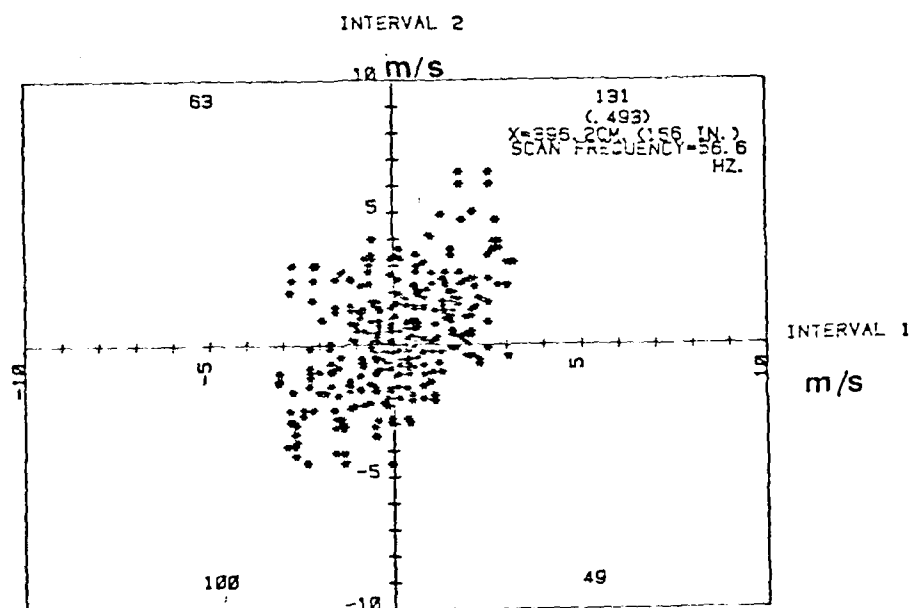


Fig. 5.11 Quadrant Analysis(Section 5.3).
For intervals information see Fig. 5.9

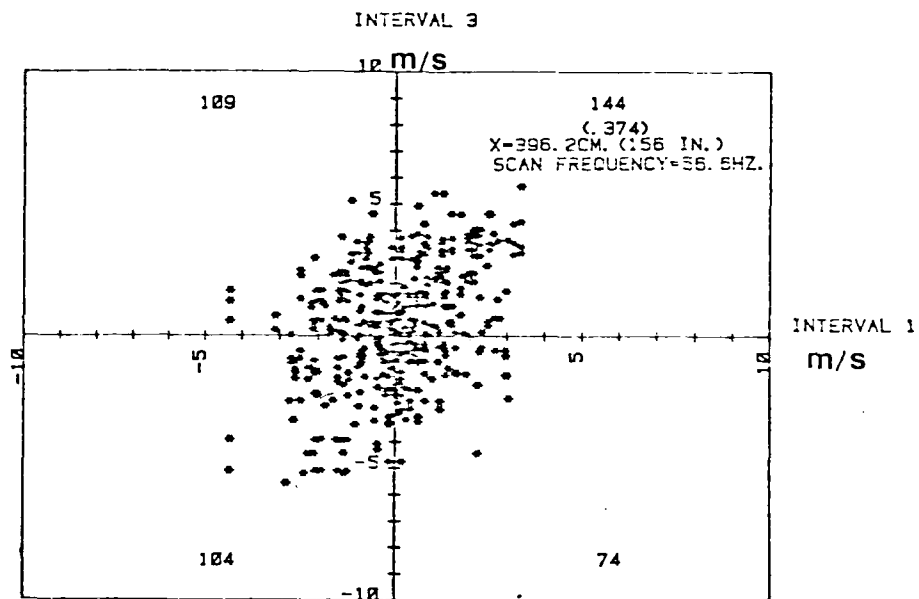


Fig. 5.12 Quadrant Analysis(Section 5.3).
For intervals information see Fig. 5.9 .

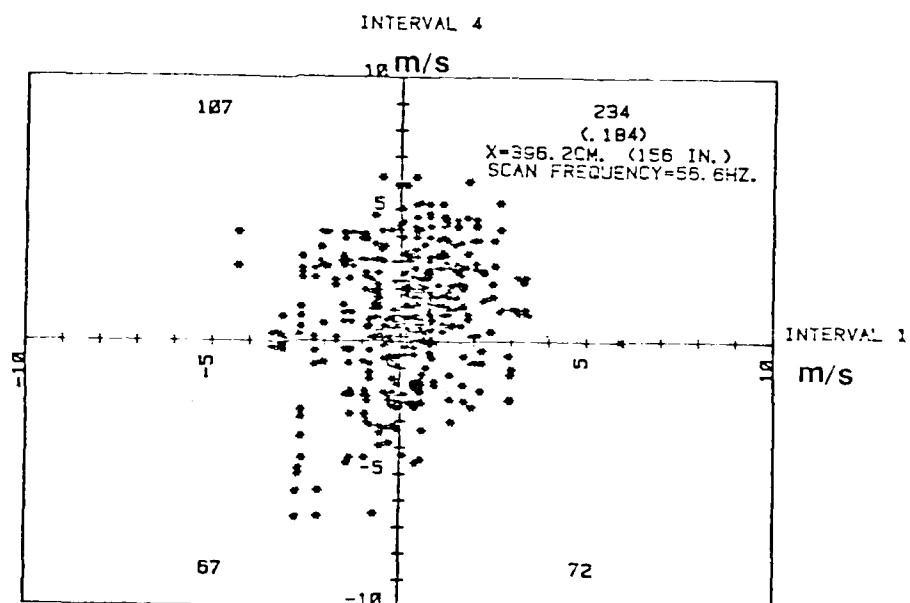


Fig. 5.13 Quadrant Analysis(Section 5.3).
For intervals information see Fig. 5.9 .

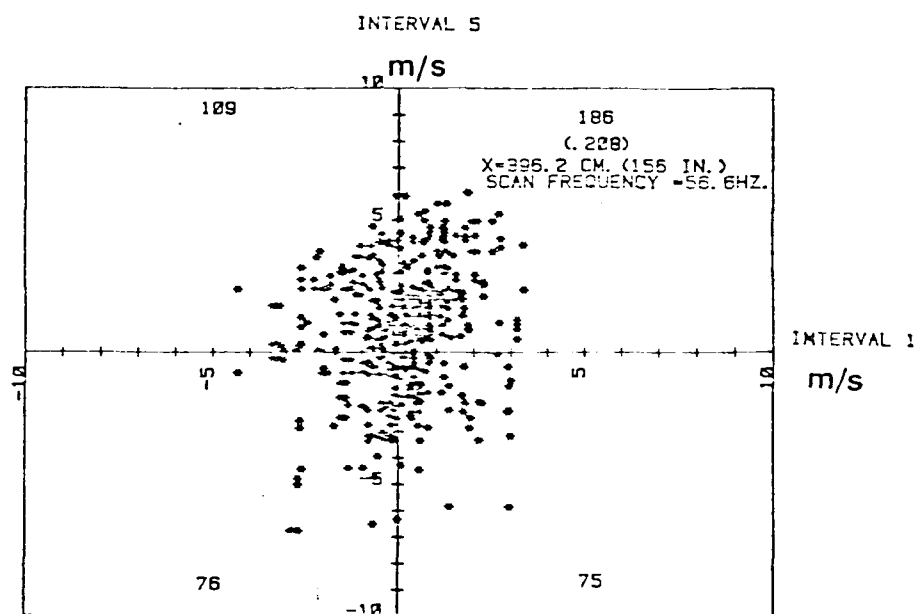


Fig. 5.14 Quadrant Analysis(Section 5.3).
For intervals information see Fig. 5.9 .

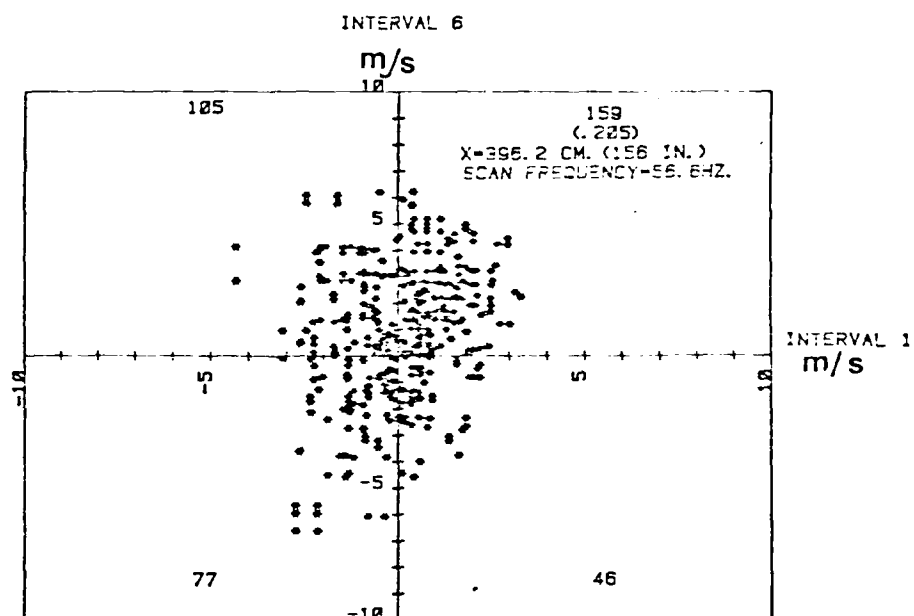


Fig. 5.15 Quadrant Analysis(Section 5.3) .

For intervals information see Fig. 5.9 .

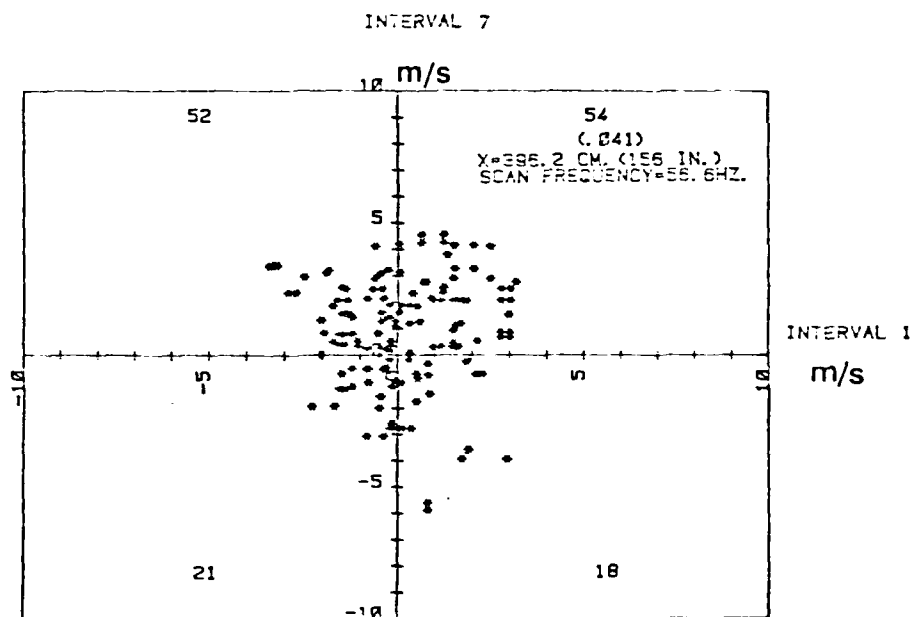


Fig. 5.16 Quadrant Analysis(Section 5.3) .
For intervals information see Fig. 5.9 .

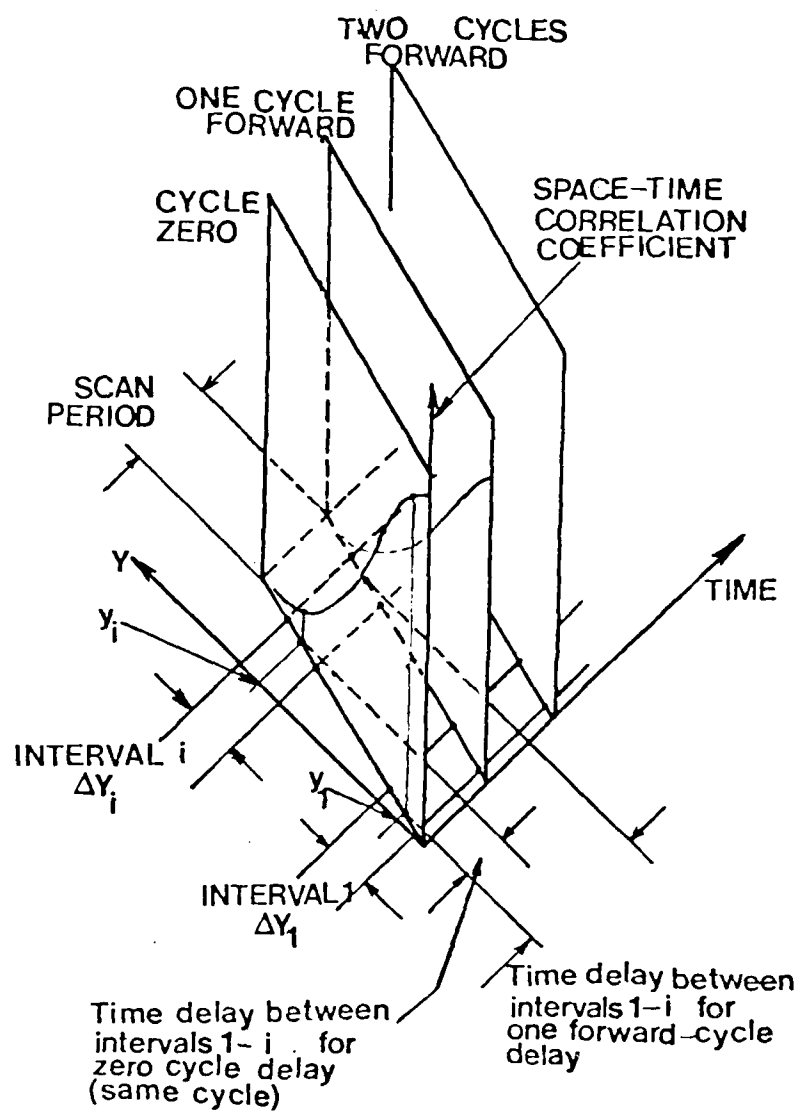


Fig. 5.17 Terminology Used For Space-Time Correlation Coefficients Determined by the Scanning LDA.

In this work, $R_{uu}(y_i - y_1, \tau)$ is estimated (Fig. 5.17) according to the following equation:

$$R_{uu}(y_i - y_1, \tau) \approx \frac{\sum u(y_1 \pm \Delta Y_1/2, t) \cdot u(y_i \pm \Delta Y_i/2, t + \tau)}{\left[\sum u^2(y_1 \pm \Delta Y_1/2, t) \cdot \sum u^2(y_i \pm \Delta Y_i/2, t + \tau) \right]^{1/2}} \quad (5.5)$$

In which $\tau = \frac{m}{f_s} + \frac{V_s}{y_i - y_1}$ for m cycle of forward delay, see Fig. 5.17,

summation is taken over the entire record. In Eq. 5.5, $Y_i \pm \Delta Y_i$ in the argument of (u) means that the value of this argument is between $Y_i - \Delta Y_i/2$ and $y_i + \Delta Y_i/2$.

In all of the space-time correlation reported here, a fixed interval near the wall was chosen against various intervals in outer region of the boundary layer for a pre-chosen number of forward-cycle delays to investigate the influence of these two regions on each other (quadrant analyses are for zero cycle delay only, Fig. 5.17).

The uncertainty of the space-time correlations was estimated by a comparison between the auto-correlations found using the scanning LDA velocity data and a fixed measurement volume experiment at $y/\delta \approx .5$ where maximum data rate was available, see Figs. 5.9 and 5.6. As it is shown in Fig. 5.18, the departure of the scanning results from that of the fixed measurement volume data increases as the number of forward-cycle delay and/or interval thickness is increased. For this reason, only results up to four cycle forward delayed is reported here. The uncertainty on space-time correlations for scanning results was estimated to be ± 0.1 from the values calculated using Eq. (5.5).

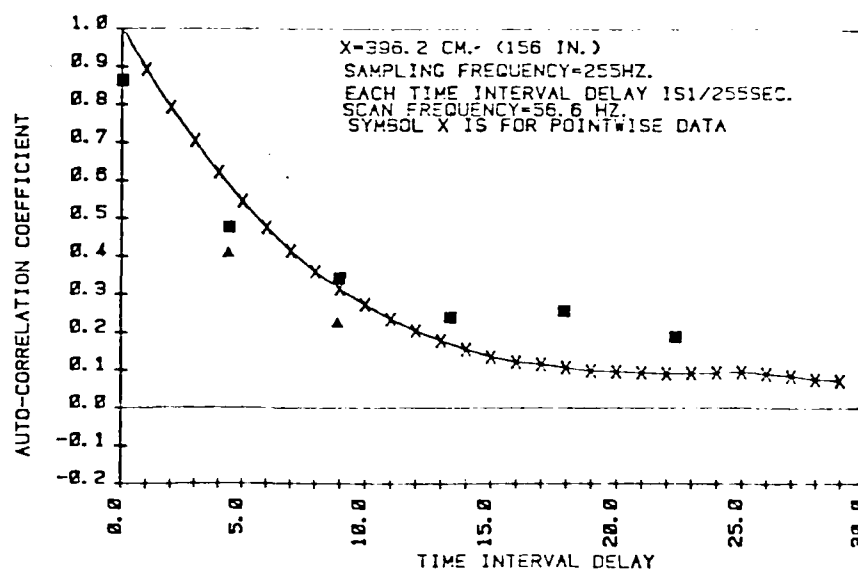


Fig. 5.18 Auto-Correlation Found Using Scanning Setup but for Fixed Measurement Volume at Y=10.2 cm as Compared with the Scanning Results for Various Number of Forward Cycle Delay for an Interval Centered around the same Y-Position.

Symbol	Interval Thickness; cm.
--------	-------------------------

▲	3.4
■	1.7

The interpretation of the quadrant analysis is that when flow is greater than the mean near the wall (interval 1), then approximately $75 \pm 5\%$ of the time flow is greater than the corresponding mean values in the central region of the boundary layer as well (Fig. 5.12, 5.13, 5.14); and when flow near the wall is less than the mean (larger back-flow), then about $60 \pm 5\%$ of the time flow is greater than the mean in the outer region. One can reverse the argument by saying: given that the flow is greater than the mean in the outer region (conditional probability), then $64 \pm 5\%$ of the time flow is larger than the mean near the wall using Figs. 5.12 to 5.14.

Space-time correlation coefficients for up to four forward-cycle delay are reported here. Figure 5.19 shows the correlation coefficient for zero cycle delay at three streamwise locations in the SMU wind tunnel. As the flow goes towards the separation zone the length scale (area under the curves in Fig. 5.19) attains values of $3.55 \pm .88$ cm, 7.9 ± 1.30 cm, 8.18 ± 2.18 cm. This means that the mean size of the eddy grows downstream which is in agreement with the earlier results from spectra in Fig. 5.8 considering that the nondimensional parameter $U_\infty/\delta(n_{\max})$ is approximately constant (≈ 4.71) for these streamwise locations. Note that the ratio of the length scale to corresponding boundary layer thickness is about $.35 \pm .09$.

Since there are no correlation coefficient measurements available in the separated region, it is not possible to critically evaluate the results obtained in this work. Correlation coefficient measurements with zero time delay are available, as reported in a work by Schubauer and Klebanoff (1951), at 9.7 cm upstream of the separation point using hot wire anemometry technique. Figure 5.20 is the results of space-time

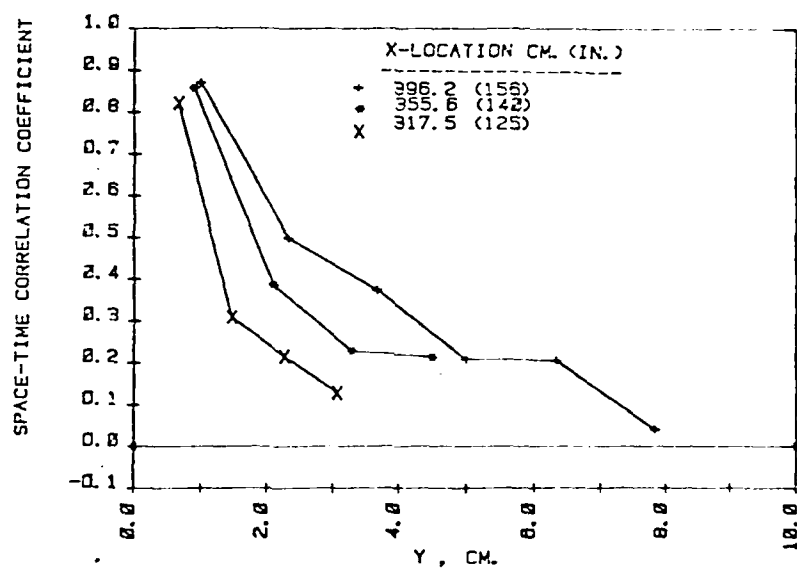


Fig. 5.19 Space-Time Correlation Coefficients for Zero Cycle Delay vs. Position at Three Different Locations.

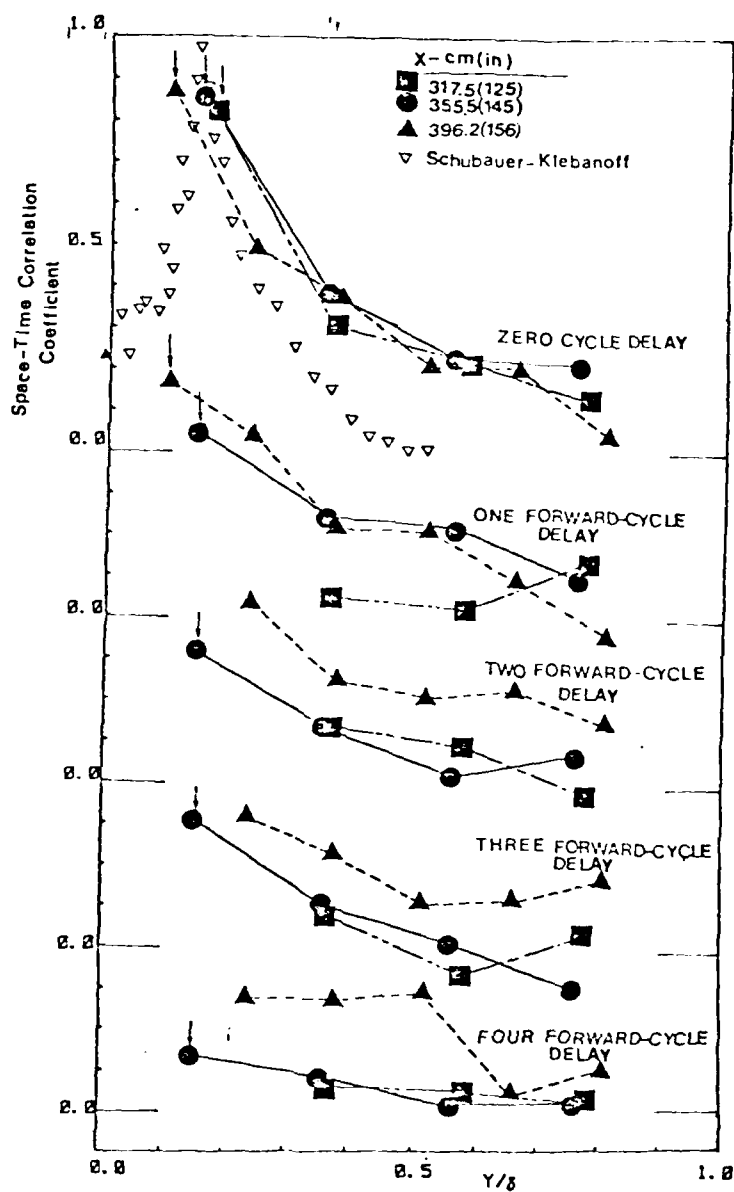


Fig. 5.20 Space-Time Correlation Coefficients between a Given Fixed Interval Near the Wall and Various Intervals vs. Y/δ for Three Streamwise locations. Arrows show the first interval near the wall.

correlation coefficients for three different streamwise locations and up to four forward-cycle delay. The time delay between the two adjacent points for the zero-cycle-delay case is about 3 msec. (use τ given in Eq. 5.5).

The space-time correlations for $y/\delta > .6$ are more uncertain because of the following reasons. Firstly, the data rate is low as it is shown in Fig. 5.6, and consequently there are not sufficient points (see Fig. 5.16) for proper convergence, and the total record-time is short, also. Secondly, due to the variation of the turbulent-nonturbulent interface and the fact that the baby powder particles tend to stay in the boundary layer, the values of correlation coefficients are high there. Finally, one should note that the correlation coefficients are between two intervals of finite length, Fig. 5.18, rather than two points in the boundary layer. Note that this last problem exists for the entire space-time correlation calculations in this work. (see section 5.4).

Despite that, one can see that the correlation between the near wall region and the outer region decreases as the number of forward cycle delay is increased. It seems that this correlation remains longer in time for the streamwise location of 396.2 cm, which is completely buried in the separation zone, which again is consistent with the fact that the energy containing eddies grow in size downstream.

Figures 5.21 to 5.23 show the same information as given in Fig. 5.20 but in different format. The points discussed above is as much physical insight as possible at present with the existing facilities.

Figures 5.24 to 5.28 show the instantaneous velocity profiles as obtained using scanning LDA system. It can be seen that most of the

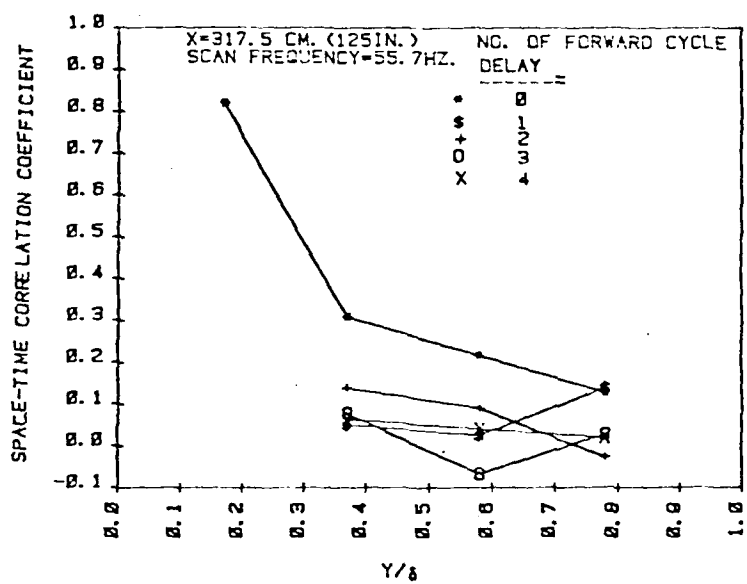


Fig. 5.21 Space- Time Correlation Coefficients vs. Y/δ .

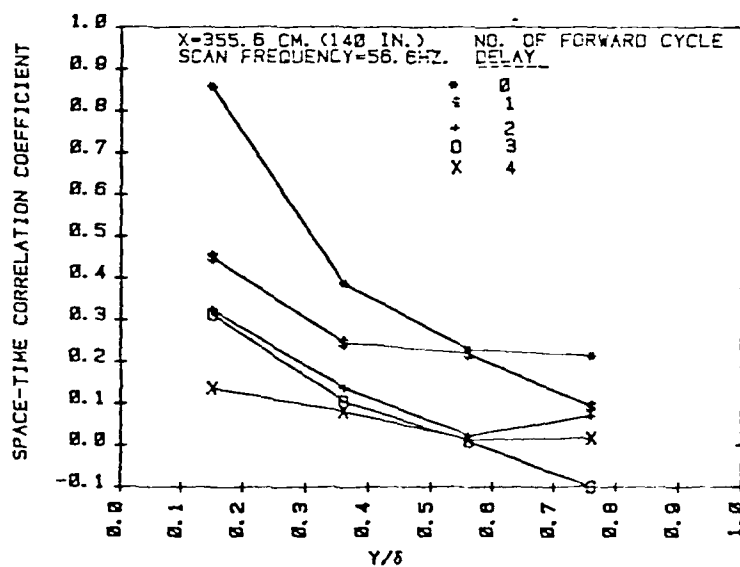


Fig. 5.22 Space-Time Correlation Coefficients vs. Y/δ .

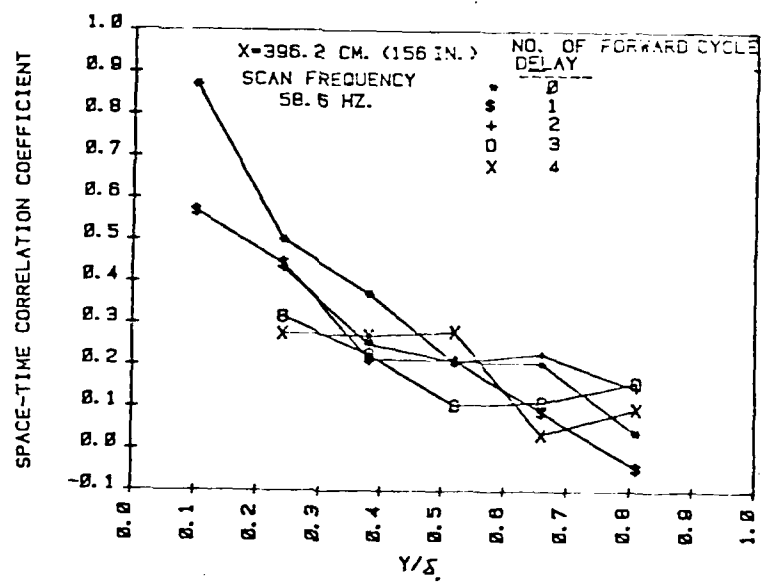


Fig. 5.23 Space-Time Correlation Coefficients vs. Y/δ .

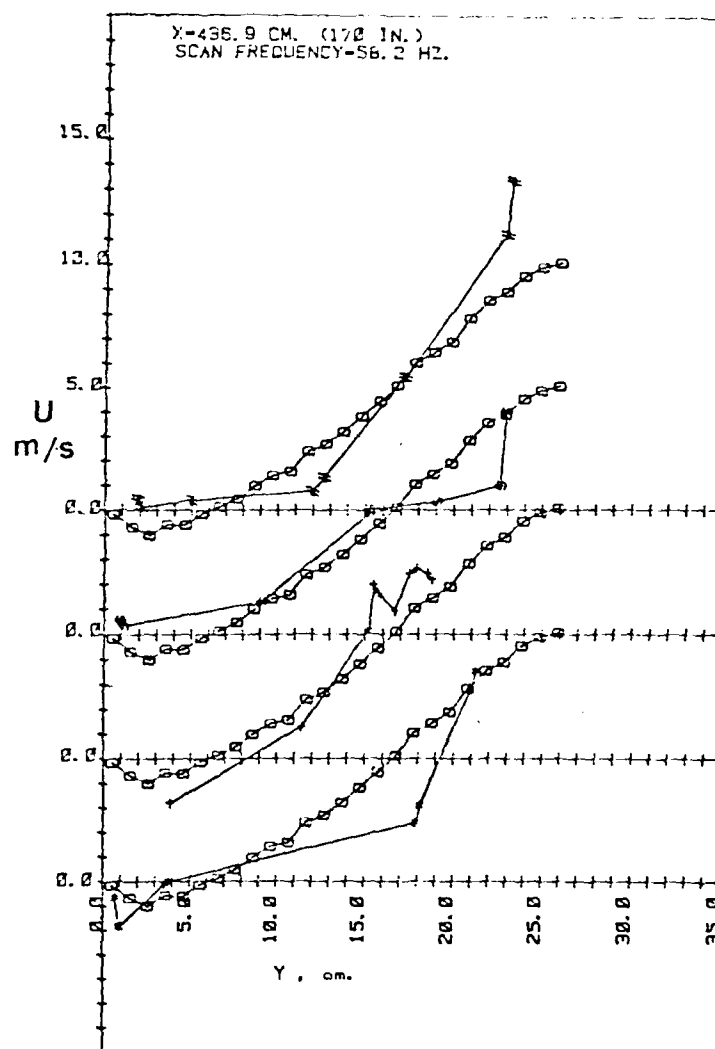


Fig. 5.25 Same as Fig. 5.24 .

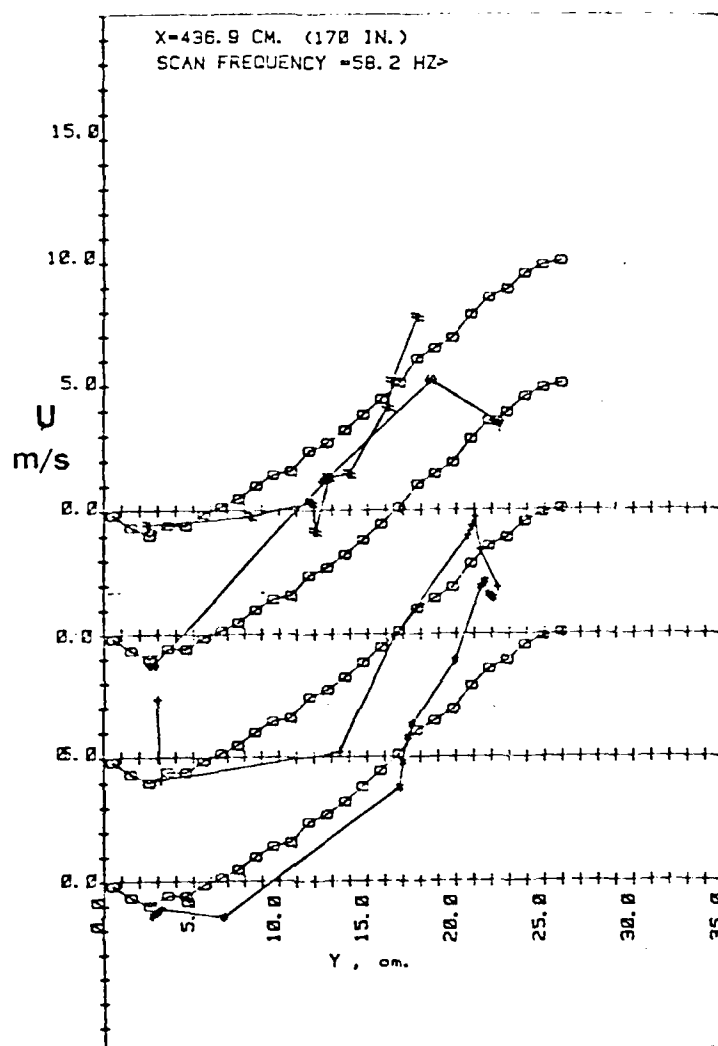


Fig. 5.26 Same as Fig. 5.24 .

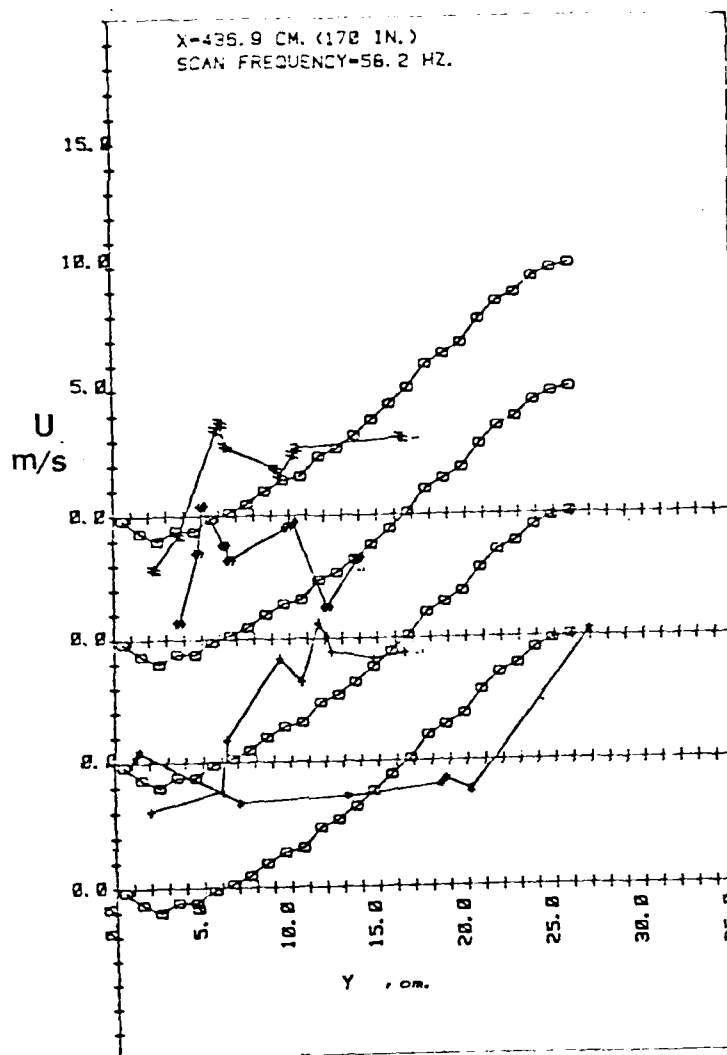


Fig. 5.27 Same as Fig. 5.24 .

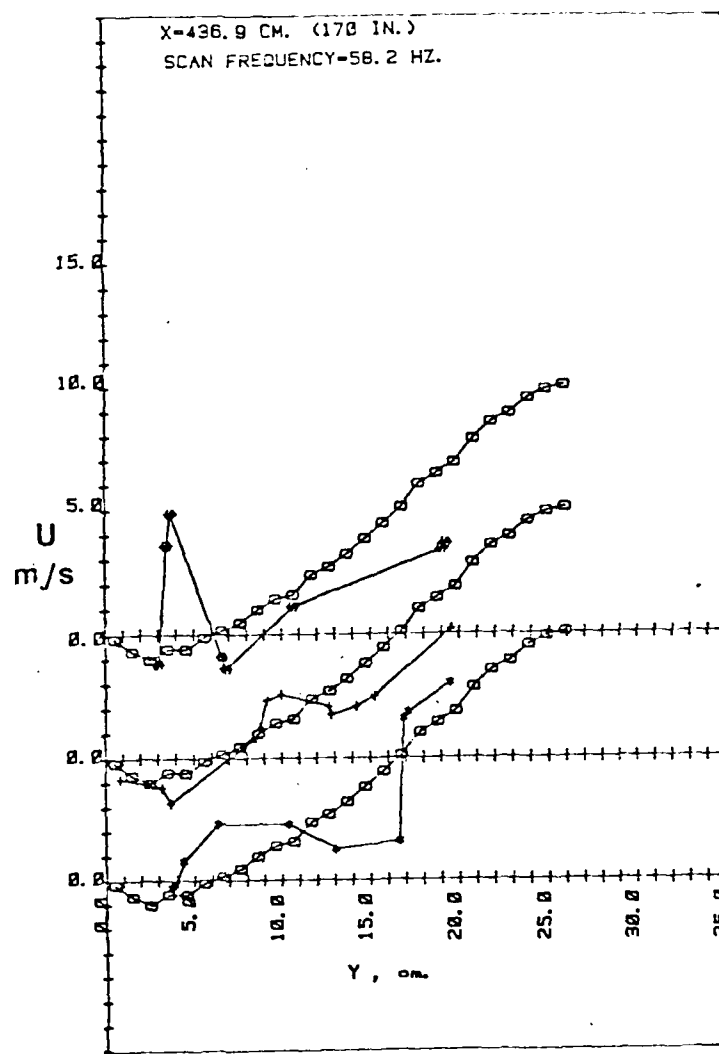


Fig. 5.28 Same as Fig. 5.24 .
Only three scans are shown.

valid measurements are in the central third of the boundary layer. There exist scan cycles in which either there are none or few numbers of valid data. Therefore, one cannot really deduce any pattern using these figures. It does, however, demonstrate the ability of having almost instantaneous velocity profiles if sufficiently high data rates are achievable.

5.4 Suggestions for Future Improvements and Extensions

Improvements on the system are divided into three parts: transmitting optics, seeding and signal processing. As for the transmitting optics, one can obtain better spatial resolution if the vertical dimension of the beams cross-over volume is decreased. One alternative is to decrease the beam diameter, but as was discussed in section 3.2.1 this means that better quality mirrors are needed (flatter surface curvature) so that the two laser beams align perfectly for all the positions of scanning (Fig. 3.5 c).

Another improvement is to drive the scanner mirror with a symmetric waveform, preferably sinusoidal, to be able to acquire validated measurements for both upsweep and downsweep scan as well as having better stability in mirror oscillations. As it was mentioned before and is obvious from Figs. 5.6 and 5.23 to 5.27, one cannot have more than a few consecutive instantaneous velocity profiles; and even then, there are not sufficient measurements in the inner and outer third of the boundary layer. This problem may be overcome by using stair-step type waveform which causes the probe volume to reside at several discrete y-locations and therefore increases the chance of having measurements for all the resident positions in a given scan. Note that one needs to adjust the damping ratio of the scanner control unit to

decrease the overshoot of the step response. A sinusoidal waveform has one more advantage that it spends more time near the wall and the outer region than the central zone of the scan range (from probability amplitude distribution). Therefore, the chance of having more consecutive "instantaneous" profiles would be increased.

The seeding technique used here is quite adequate for mean and rms value measurements and the only improvement is to increase the record time which in turn means larger memory area (section 5.1). The seeder itself, though, needs some improvements to increase its stability and/or controllability. There are two major improvements on the seeder: firstly, feed-back control to maintain a constant piston velocity for stability of the baby powder concentration; and, secondly, variable speed wirebrush motor for controllability. In the absence of any other seeding techniques, the aforementioned improvements on the seeding are necessary. More investigations on the seeding techniques and seeding materials are encouraged for any sophisticated flow analysis.

As far as data processing is concerned the counter type processor was found to be quite adequate for this work despite being very sensitive to the amplifier gain settings and not having better scale sensitivity. An automatic gain control would be of some value in this work as was also mentioned by Orloff et al. (1975). As for the acquisition technique, it is essential to be able to sample both position and velocity information simultaneously when the latter is available (can be found by data ready pulse from the counter). The data acquisition used in this work was the only choice based on the facilities available at the time.

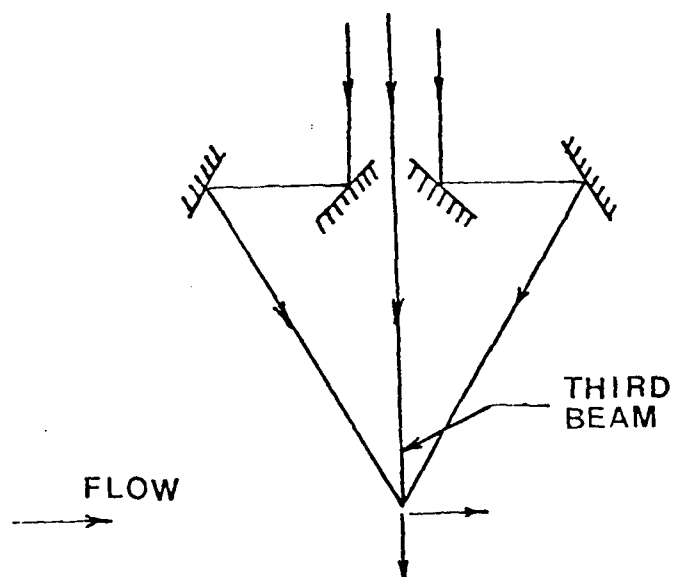


Fig. 5.29 A Suggested Extension of the Existing Scanning LDA to Two Dimensional scanning system.

A transient recorder may be the "ideal" data processing technique, Durst et al. (1981), which digitizes Doppler signal from the PM-tube and the position transducer voltage simultaneously, and is triggered only when a Doppler burst is available (Bates, 1979). Transient recorders with sampling frequency up to 100 MHz, suitable for air studies, are available (see Petersen and Maurer, 1975).

One important advantage of the existing design is the possibility of extension so that it could measure streamwise and cross-flow velocity profiles simultaneously. Figure 5.29 shows the schematic of the design proposal. The principle of operation for this three beam system for point-by-point measurement is discussed in a report by TSI, Inc. (1983). The two side beams need to be down and up-shifted with two different frequencies, and path equalization for three beams should also be considered.

5.5 Conclusions

A rapidly scanning directionally-sensitive fringe-type laser Doppler Anemometer (SLDA) which scans the measurement volume perpendicular to the optical axis of the transmitting optics is described. The fringe spacing can be easily adjusted from 1 μm to 4 μm . Scan frequencies up to 60 Hz over scan distances of 40 cm have been used, although scan frequencies up to 150 Hz are possible. The maximum scanning velocity of the measurement volume that can be used is directly proportional to the shift frequency of the Bragg cell, since each signal producing particle must cross a minimum number of fringes to produce a valid signal. Signal averaging bias is lower with a scanning LDA than with pointwise measurements. Results obtained for a separating turbulent boundary layer show that good mean and rms velocity profiles and

profiles of the fraction of time that the flow moves downstream can be obtained in less than one minute of data acquisition. Improvements in seeding and signal processing are needed to further improve the data rate and permit almost instantaneous velocity profiles to be obtained for each scan.

Space-time correlations, although with uncertainty band, were taken for the first time in separated turbulent boundary layer and showed that the length scale for the large eddies grows in size towards the separation although the ratio of the length scale to the boundary layer thickness remains constant. Quadrant analysis not too far from the separation point says that when flow is greater than the mean in the outer region, then it is most probably greater than the mean near the wall, too, and vice versa, which represents some degree of coherence between these two regions.

The advantages of the SLDA reported here for large wind-tunnel-flow surveying is obvious if one considers that at each location two-dimensional velocity profiles are possible in an order of a few minutes (for better convergence). With improvements mentioned above, one can obtain almost instantaneous velocity profiles which could reveal more details of the flow structure.

REFERENCES

- Adrian, R. J., Humphrey, J. A. C., and Whitelaw, J. H., 1975. Frequency measurement errors due to noise in LDV signals, Proc. LDA-Symposium, Copenhagen, pp. 287-311.
- Bates, C. J. 1979. Software consideration for use with a transient recorder/minicomputer LDA system, Proc. of the Sixth Symposium on Turbulence in Liquids, University of Missouri-Rolla, pp. 104-113.
- Bates, C. J., and Hughes, T. D. 1976. Real-time statistical LDV system for the study of a high Reynolds number, low turbulence intensity flow, J. Phys. E: Sci. Instrum., Vol. 9, pp. 995-958.
- Bendick, P. J. 1971. A Laser Doppler velocimeter to measure instantaneous velocity profiles, Proc. Flow Symposium, May 10-14, Pittsburgh.
- Brosens, P. 1976. Scanning accuracy of the moving-iron galvanometer scanner, Optical Engineering, Vol. 15, No. 2, pp. 95-98.
- Buchhave, P., George, W. K. Jr., and Lumley, J. L. 1979. The measurement of turbulence with the Laser-Doppler anemometer, Ann. Rev. Fluid Mech. Vol. 11, pp. 443-503.
- Durst, F., Lehmann, B., and Tropea, C. 1981. Laser Doppler system for rapid scanning of flow fields, Rev. Sci. Instr., Vol. 52, pp. 1676-1681.
- Durst, F., Melling, A., and Whitelaw, J. H. 1976. Principles and Practice of Laser-Doppler Anemometry, New York; (Academic Press).
- Echols, W. H., and Young, J. A. 1963. Studies of Portable Air-Operated Aerosol Generators, NRL Report 5929.
- Gartrell, L. R. and Jordan, F. J. 1977. Demonstration of a rapid-scan two-dimensional Laser velocimeter in the Langley vortex research facility for research in aerial application, NASA TM-74081.
- Grant, G. R. and Orloff, K. L. 1973. Two-color dual-beam backscatter Laser Doppler velocimeter, J. of Applied Optics, Vol. 12, pp. 2913-2916.
- Hjelmfel, A. T. Jr., Mockros, L. F. 1966. Motion of discrete particles in a turbulent fluid, App. Sci. Res., Vol. 16, pp. 149-161.
- Kline, S. J., and McClintock, F. A. 1953. Describing uncertainties in single sample experiments, Mech. Eng., Vol. 75, p.3.

- McLaughlin, D. K. and Tiederman, W. G. 1973. Biasing correction for individual realization of Laser anemometer measurements in turbulent flows, Physics of Fluids, Vol. 16, Number 12, pp. 2082-2088.
- Meyers, J. F. 1979. Applications of Laser velocimetry to large scale and specialized aerodynamic tests, TSI Quarterly, 5, Issue 4, pp. 5-12.
- Muzumder, M. K., et al. 1979. Spart analyzer, J. Aerosol Science, Vol. 10, pp. 561-569.
- Nakatani, N., Yorisue, R., and Yamada, T. 1978. Simultaneous measurement of flow velocities in multipoint by the Laser Doppler Velocimeter, Proc. of the Dynamics Flow Conference, Marseille, Baltimore, pp. 583-590.
- Orloff, K. L. and Biggers, J. C. 1974. Laser velocimeter of developing and periodic flows, Proc. of the Second International Workshop on LDV, Purdue University, Vol. 2, pp. 143-168.
- Orloff, K. L., Corsiglia, V. R., Biggers, J. D. and Ekstedt., T. W. 1975. The accuracy of the flow measurements by Laser-Doppler methods, Proc. of the LDA - Symposium, Copenhagen, pp. 624-643.
- Perry, A. E. and Schofield, W. H. 1973. Mean velocity and shear stress distributions in turbulent boundary layers, The Physics of Fluids, Vol. 16, No. 12, pp. 2068-2074.
- Petersen, J. D. and Maurer, F. 1975. A method for the analysis of Laser-Doppler signals using a computer in connection with a fast A/D converter, The accuracy of flow measurement, ed. P. Buchaue, Copenhagen: Proc. LDA Symposium, pp. 312-318.
- Rhodes, D. B. 1976. Optical scanning system for Laser velocimeter, SPIE, Vol. 84, pp. 78-84.
- Schofield, W. H. 1980. Turbulent boundary layers in strong adverse pressure gradients, Department of Defense, Defense Science and Technology Organization, Aeronautical Research Laboratories, Melbourne, Victoria, Mechanical Engineering Report 157, Commonwealth of Australia.
- Schubauer, G. B. and Kelebanoff, P. S. 1951. Investigation of separation of the turbulent boundary layer, NACA Report 1030.
- Seegmiller, H., 1982. Private communication with Prof. R. L. Simpson.
- Simpson, R. L. 1978. Measurements in highly turbulent flows: steady and unsteady separated turbulent layers, Third International Workshop on Laser Velocimetry, Purdue University, Eds. H. D. Thompson and W. H. Stevenson, pp. 175-195.

- Simpson, R. L. 1983. A model for the backflow mean velocity profile, AIAA Journal, Vol. 21, pp. 142-143.
- Simpson, R. L., Chew, Y. T., and Shivaprasad, B. G. 1980. Measurements of a separating turbulent boundary layer, Project SQUID Report SMU-4-PU (AD-A095252/3).
- Simpson, R. L., Chew, Y. T., and Shivaprasad, B. G. 1981. The structure of a separating turbulent boundary layer. J. Fluid Mech., Vol. 113, pp. 53-73.
- TSI Incorporated, 1983. 3-Component, On-Axis LDV System, Technical Information.
- Yanta, W. J., and Smith, R. A. 1973. AIAA 11th Aerospace Sciences Meeting, Washington, D. C. Paper 73-169.

DATE
LMED
8